Investigation of the Very Large Eddy Simulation Model in the Context of Fluid-Structure Interaction

Vom Fachbereich Maschinenbau
an der Technischen Universität Darmstadt
zur Erlangung des akademischen Grades eines
Doktor-Ingenieurs (Dr.-Ing.) genehmigte

Dissertation

vorgelegt von

Anastasia Kondratyuk M.Sc.

aus Selenodolsk, Russland

Berichterstatter:	Prof. Dr. rer. nat. Michael Schäfer
Mitberichterstatter:	Apl. Prof. Dr.-Ing. habil. Suad Jakirlic
Tag der Einreichung:	17. Januar 2017
Tag der mündlichen Prüfung:	25. April 2017

Darmstadt 2017
D17

Vorwort

Diese Arbeit ist der Abschluss meines Promotionsstudiums an der Graduate School of Computational Engineering am Fachgebiet Numerische Berechnungsverfahren im Maschinenbau an der TU Darmstadt. Ich möchte mich für die Bewilligung dieses Stipendiums beim Board of Deans der Graduate School of Computational Engineering herzlich bedanken.

Zuerst bedanke ich mich bei meinem Betreuer Herrn Professor Schäfer, dem Leiter des Fachgebiets, für die Möglichkeit am Fachbereich zu promovieren. Die sehr angenehme Atmosphäre, die am Fachbereich herrscht, bietet Raum für freies Denken und ermöglicht es neue Ideen auszuprobieren. Damit wird eine perfekte Arbeitsatmosphäre für eine erfolgreiche Promotion geschaffen. Bei Herrn Professor Jakirlic bedanke ich mich für die Übernahme der Zweitbetreuung, für die fachliche Hilfe in Fragen zu Turbulenz und ehrliches Feedback.

Weiterhin danke ich meinem Masterarbeitsbetreuer und späteren Bürokollegen Dr. Sebastian Türk zuerst für die Unterstützung in der Entscheidungsfindung zu promovieren, für die Hilfe in den ersten Zeiten am Fachgebiet und für die Bereitschaft für fachliche Diskussionen. Besonders bedanke ich mich für das Korrekturlesen und die sehr hilfreichen Anmerkungen.

Allen meinen FNB-Kollegen danke ich für die Zusammenarbeit am Fachbereich. Herrn Ali bin ich sehr dankbar für den Austausch von Fachwissen und Korrektur meiner Arbeit. Besonders gern würde ich Herrn Dr. Dominik Staab, Herrn Dr. Stefan Kneißl und Frau Dr. Stefanie Röder für die wunderschöne Zeit am Fachbereich und außerhalb des Arbeitsalltags Danke sagen. Die zahlreichen Diskussionen werden mir für lange Zeit im Gedächtnis bleiben.

Danke an Michael Fladerer, der erster Ansprechpartner für Probleme mit dem Computersystem und dem Cluster war. Frau Monika Müller bin ich sehr dankbar für die Bereitschaft immer zu helfen und ihre Unterstützung in jeder Situation. Dem ganzen administrativen Team der Graduate School of Computational Engineering sage ich auch Danke.

Danke an meine ehemaligen Master- und Bachelorstudenten Herrn Li und Herrn Henzel für die fruchtbare Zusammenarbeit.

Abschließend möchte ich mich ganz herzlich bei meinen Eltern bedanken, die mir mein Studium und meine Promotion in Deutschland ermöglichten. Ihre Unterstützung und Zuneigung ist sehr wichtig für mich. Von ganzem Herzen will ich meinem Freund Andreas Reinauer danken für die Geduld vielmals meine Präsentationen anzuhören und meine Texte zu korrigieren und für die ständige Unterstützung bei meiner Promotion.

Contents

1 Introduction

1.1 Motivation

Turbulent flows play a dominant role in most technical applications, for instance in the automobile industry or in aviation. Therefore, the correct prediction of these flows is a very important task. The understanding of turbulent flows can help to control and optimize the flow parameters for technical fields, what leading to, among others things, more efficient use of technologies in terms of energy and time, as well as leading to safety improvement. Despite the essential role of turbulence, a concrete definition of this phenomenon is missing. One of the most complete descriptions of turbulence was framed by Bradshaw in 1971 [17]:

> "Turbulence is a three dimensional time dependent motion in which vortex stretching causes velocity fluctuations to spread to all wavelengths between a minimum determined by viscous forces and a maximum determined by the boundary conditions. It is the usual state of fluid motion except at low Reynolds numbers."

This definition recognizes, that turbulence phenomena are very complex, and therefore the numerical simulation of these flows is very challenging, due to the wide range of eddy structures with different length and time scales.

In the last 60 years, with the rapid increase of computational power, the application of numerical simulations for the prediction of turbulent flows has grown continuously. Computational fluid dynamics provides the possibility to predict different kinds of flows and demonstrates advantages over time-consuming and expensive experiments.

The most exact technique for the prediction of turbulent flows is a direct numerical simulation (DNS), which allows resolution of the complete range of turbulent scales. However, the prediction of complex unsteady flows with DNS is very expensive in terms of computational effort, due to the required high-grid refinement for the complete resolution of turbulent structures. Therefore, nowadays the DNS can be applied only to flows with very simple geometries and small Reynolds numbers. By contrast, with the Reynolds-average Navier-Stokes (RANS) approach all of the turbulent vortices, also called eddies, are modeled. The broader scope of this approach leads to a significant reduction in computational time. However, this approach shows weaknesses in the simulation of some types of turbulent flows, especially flows with massive separations, for instance in aerodynamic or rotation flows. An alternative to these two techniques is large eddy simulation (LES). On this approach large, energy-containing turbulent scales are resolved, while the small, universal eddies are modeled. In this case, the results are more accurate than in RANS simulations, and computational effort is less than in DNS; nevertheless computational time grows rapidly with increasing Reynolds numbers and is still too high for the simulation of

industrial flows. Therefore in the last two decades, so-called hybrid turbulence techniques have become especially popular. Such models combine the advantages of the basic modeling methods outlined in the beginning with an aim to produce accurate results with reduced computational time.

The problems of computational cost become especially demanding in the case of coupled problems, such as fluid-structure interaction (FSI) tasks. One of the reasons for the increase of the computational effort in simulations with a coupling between fluid and structure is additional equations of motion for the structural part, which have to be solved per iteration. FSI problems occur in different applications, for instance in the design of wind turbines, and consideration of these problems can help to increase the efficiency of a construction. In biomechanics, FSI simulations can be applied in the modeling of optimized artificial heart valves, whereas in civil engineering they are used in the calculation of the dynamic response of bridges or buildings to excitation by wind or water. The simulation of multiphysics problems is a challenging task. Difficulties occur primarily in the coupling of two different problems with different background foundations. In case of FSI, these nackground foundations are the finite volume method (FVM) regarding the fluid and the finite elements method (FEM) in the description of the structure. Each has different numerical fundamentals: for instance, the additional interpolation between the nodal values in FEM codes and the cell-centered values in FVM programs have to be realized. Therefore, in the investigation of multiphysics problems, the main focus lies on coupling algorithms and moving grids, while the fluid element is often neglected by means of applying laminar flows in such problem configurations. The important aspect of turbulence is often hardly considered, and the turbulent FSI is currently not an established research subject, although most FSI effects occur in turbulent flows. Therefore, the study of turbulent phenomena in context of FSI is of special interest. The potential for hybrid modeling in this context is quite promising. Most FSI flow configurations have massive separation regions. The RANS model is not able to capture the main behavior of such turbulent flows, contrary to the hybrid approaches, which additionally provide a reduction of computational time, as compared to LES. Another important reason for the investigation of turbulence modeling techniques on moving structures is a lack of information about the behavior of turbulent methods in this context, while a variety of studies and best-practice-guidelines are available for the turbulence models on stationary grids.

1.2 Goals of this work

The focus of the present study lies in the investigation of a relatively new hybrid modeling technique, the so-called very large eddy simulation (VLES) strategy, in the context of FSI. This investigation requires an extension of the turbulence modeling part in the in-house code FASTEST, from the Institute of Numerical Methods in Mechanical Engineering at the TU Darmstadt, with the new turbulent technique VLES. The next step is a systematic investigation of the implemented VLES model for the examination of this model's capabilities and a demonstration of the advantages of this approach over other turbulence modeling techniques. Firstly, simulations on stationary grids with different test cases are performed, which cover a variety of flow configurations and demonstrate the capability of the VLES model to predict different kinds of turbulent

flows occurring in technical applications. Afterwards, an investigation of the VLES model in the context of moving grids is undertaken, which is necessary for the subsequent enhancement of this study on FSI problems and for the demonstration of the ability of the VLES model to produce satisfactory results in challenging multiphysics cases.

1.3 Outline of this work

The present work begins by outlining theoretical fundamentals for fluid dynamics, fluid-structure coupling and turbulence phenomena. The second chapter deals with the foundations of turbulence modeling, including the introduction of the VLES model, which is of central interest in this study. Chapter 4 introduces numerical methods essential to this work (e.g. spatial and time discretization). Moreover, the in-house code FASTEST is briefly introduced. The results of the verification procedure for the RANS models, which are the basis of the VLES method, are presented in Chapter 5. Afterwards, Chapter 6 applies the VLES model to the simulation of three different flow configurations on stationary grids and includes an investigation of the influence of different filter widths in the formulation of the VLES approach. In Chapter 7, the simulation results of the VLES model on moving grids for two different cases are presented and discussed. Afterwards, the VLES method is applied in the context of FSI problems and compared to other turbulence modeling techniques.This dissertation concludes with a summary of its results and recommendations for future study of this subject.

1.4 State of the art

This section presents an overview of current techniques, methods and results in FSI, in turbulence modeling, and in the turbulent FSI.

Fluid-structure interaction (FSI)

In FSI problems, the deformation of the computational domain plays a central role, along with the resulting the deformation of the grid, caused by the distortion of structure and fluid. The Eulerian system used for the Navier-Stokes equation and the Lagrangian formulation applied to the structural component of FSI problems are not suited in the case of fluid-structure coupling. One of the methods to manage the dynamics of the fluid and the structure is the *arbitrary Lagrangian-Eulerian (ALE)* formulation, introduced by Hirt et al. [67] and belonging to the group of boundary-fitted methods. The idea behind this technique is a combination of the Eulerian and Lagrangian formulations that incorporate the grid velocity in the Navier-Stokes equation for the description of the fluid component, while the structure part is described in a Lagrangian framework. The ALE method is based on the space conservation law formulated, e.g. by Demirdžić and Perić [33], where mass conservation by grid deformation is required. The application of the ALE formulation in FSI problems was first suggested by Donea et al. [35]. In the ALE formulation, the fluid grid and the structure mesh have the same deformation at the

coupling interface. This sameness is the source of this method's main advantage: the possibility to construct an appropriately fine mesh in the vicinity of the structural surface to resolve the flow phenomena around solid boundaries. As a result, fluid quantities can be calculated with better accuracy. Another benefit of the ALE method is the relative ease of its implementation. However, this technique demonstrates disadvantages for large structural deformations. Furthermore the re-meshing required in each time step leads to an increase of computational effort. Despite these drawbacks, the ALE formulation is widely used in the numerical simulation of FSI systems. For application examples and a more detailed description of the ALE method in fluid-structure coupling the reader is referred to [10], [71] and [46].

Alternatives to the ALE method include *interface-capturing approaches* (i.e. fixed-grid methods), where the fluid grid does not move in every time step together with the structure. The most commonly applied of these techniques is an *immersed boundary method* introduced by Peskin [117], [118] for numerical investigations in hemodynamics. The discretization of the foundation equations is realized by assuming a Eulerian grid for the fluid part and representing the immersed surface as a set of elastic fibers in a Lagrangian coordinate system, which moves with the fluid velocity. Fluid velocities on the fictitious subdomain are interpolated into the structure domain to evaluate the structural deformation and structural forces are interpolated back into the fluid domain. The forces arising from the structural side are incorporated into the Navier-Stokes equations by means of an additional source term. A benefit of this method over the ALE formulation is the elimination of the re-meshing and therefore the reduction of computational time. Variations of this basic approach have been widely investigated [90], [109], [81], [134] and applied to different FSI problems [26], [11], [15], [145]. Another technique belonging to the fixed-grid approaches is the *fiction domain method* (distributed Lagrange multiplier method) developed by Baaijens [5]. Fluid and solid meshes are generated independently from each other and both domains are coupled by means of a Lagrange multiplier along the solid boundary. The solid deformed under the acting fluid forces is described in Lagrangian way, while the Eulerian fluid mesh does not require updating. This method has been applied in the biomechanics field by De Hart et al. [29]. Fixed-grid approaches are often unsuitable for FSI calculations, since FSI problems require an accurate resolution of the flow feature in the vicinity of the solid interface between fluid and structure, which is hardly feasible with such techniques. Therefore fixed-grid techniques are rarely applied for complex FSI problems. As mentioned in [165], the ALE-formulation is preferred over the other approaches if the problem formulation permits. An overview over the current techniques and algorithms can be found in [68].

The second essential aspect of FSI applications is a coupling between fluid and structure. Different coupling techniques can be grouped into two categories: the *monolithic approach* and *partitioned approach*. In the monolithic method, fluid and structure equations are solved in one global system of equations simultaneously with implicitly given interface conditions. This strategy leads to improved solution stability and to better convergence behaviors [32], [69]. However the implementation of this method is costly in terms of software engineering [68]. The monolithic approach is detailed in the works of Michler et al. [107], Blom [14], Heil et al. [66] and Hübner et al. [70].

Due to the benefit in realization (from the software point of view), the partitioned approaches

are widely used in FSI problems. With this method, the fluid and the structure are treated separately on independent meshes and in different codes. Therefore, well-established software, which offers a variety of numerical methods, can be applied for calculations relating to the fluid and structure components. The realization effort is restricted by the development of the coupling and communication algorithms for the interaction procedure. The partitioned approaches are subdivided into implicit and explicit methods. In the last group the fluid-structure coupling is performed only once in each time step. Explicit methods have been successfully applied in simulation of aeroelasticity problems, which occur in compressible flows [43]. The application of such methods frequently leads to unstable behavior, and as a result a strong limitation on the used time step size [100] is imposed. In the implicit approach the coupling between structure and fluid is performed in every time step repeatedly until a convergent solution is found. In contrast to the explicit method, this technique demonstrates more robustness and improved convergence behavior [135], [111]. Different numerical methods have been developed to increase the convergence rate and reduce the computational time, for instance the fixed-point method with dynamic relaxation [167] or vector extrapolation methods [166], [108].

In the present work for the simulation of FSI problems, the ALE technique and the implicit portioned approach are applied.

Turbulence modeling

The foundation for the modeling of turbulent flows was expressed by Richardson in 1922 in lyrical form [129]:

> "Big whorls have little whorls
> Which feed on their velocity,
> And little whorls have lesser whorls
> And so on to viscosity."

This mechanism is denoted as *energy cascade* and has been investigated in detail by Kolmogorov [84]. He formulated three hypotheses for the description of the turbulence phenomenon and moreover introduced the concept of the energy spectrum. The simulation of turbulence is based on this idea until today.

Turbulence models can be subdivided into four groups: DNS, LES, RANS and hybrid models. Since the DNS is not of essential interest for the present work, the review of this model is not presented here. Nevertheless, the idea of this concept is briefly outlined in chapter 3.

The formulation of RANS models is based on the idea of a decomposition of main flow quantities into a mean part and a fluctuating part, as proposed by Reynolds [128] in 1895. RANS models produce a statistical representation of turbulent features that is sufficient for many engineering applications. Due to the relatively low computational effort that they requiere, RANS models are widely used in the industrial field. By inserting the Reynolds decomposition in the Navier-Stokes equation and subsequent averaging, new unknown term arise, the so-called Reynolds stress tensor. As a result, the closure problem emerges. Depending on the how these unknown terms are

modeled, RANS models can be categorized into two groups: the Reynolds stress models (RSMs) and eddy-viscosity models (EVMs).

In RMS an individual differential equation is formulated for each Reynolds stress component. This idea was first mentioned in the works of Hanjalic and Launder [62] and Launder et al. [89]. Subsequent investigations of this class of turbulence models have been published in Speziale et al. [153], Durbin [37] and Jakirlic and Hanjalic [74]. One of the advantages such models is their ability to capture the influence of the Reynolds stress anisotropy in the velocity field. Nevertheless the solution of additional equations is required, and as a consequence the computational time increases.

In the eddy-viscosity concept, the Reynolds stress tensor is presented as a product of the turbulent viscosity and the mean rate of strain in accordance with the hypothesis of Boussinesq [16]. This approach is based on the idea of the similarity of the average turbulent flow field and the corresponding laminar flow. A wide range of turbulence models based on this concept has been developed. Depending on the number of additional transport equations that have to be solved to compute the eddy viscosity, the zero-, one-, two- or four-equations models are distinguished.

The zero-equation turbulence model was introduced by Prandtl in 1925. In the Prandtl mixing-length model, the effective viscosity is expressed as the product of a turbulent velocity scale and a characteristic length (mixing length) scale. Other formulations of zero-equation models can be found in Baldwin and Lomax [6] and Johnson and King [78]. Such models are often too simple for usage in general situations. The commonly used one-equation model with the objective of numerical efficiency and robustness is the Spalart-Allmaras approach [148]. This model includes the transport equation for turbulent eddy viscosity. Although this model demonstrates the ability to predict attached wall-bounded flows and flows with mild separation or recirculation, it is weak in the simulation of the free shear or massively separated flows. The Spalart-Allmaras method is generally applied in aerodynamic problems and in turbo-machinery applications

Two-equation models have become the preferred model type in different industrial application fields. The most frequently applied method is the $k - \varepsilon$ approach. Although the earliest ideas of this model have been mentioned in [64] and [61], the complete formulation of this model is presented in Jones and Launder [79]. The main idea of the $k - \varepsilon$ RANS method is to solve additional transport equations for turbulent kinetic energy and for dissipation, for closure of the problem. However, this model demonstrates weaknesses in the near-wall region; therefore several modifications of this model have been developed, the most popular being introduced in Launder and Sharma [88] and Chien [25]. Another commonly applied two-equation model, the $k - \omega$ approach, has been developed by Wilcox [169]. In this method, for the calculation of the turbulent viscosity, one must solve transport equations for the turbulent kinetic energy and for the specific dissipation rate. The introduction of the specific dissipation rate provides advantages in wall treatment. as compared to the $k - \varepsilon$ model. However, this approach suffers from problems with respect to the separation region. Menter [106] suggested the shear stress transport (SST) $k - \omega$ model, which combines these two approaches. Menter's model switches to the $k - \omega$ method in the inner parts of the boundary layer and to a $k - \varepsilon$ formulation in the free-stream.

In the immediate vicinity of the wall, the modeling of turbulence is a difficult task due to its physical complexity. To improve the prediction in the near-wall region, Durbin [39] suggested to

use the transport equation for the normal-to-the-wall stress component $\overline{v^2}$ in addition to the equations for k and ε. This strategy allows one to improve the reproduction of wall-near anisotropy and non-local pressure-strain effects. To improve the stability of this model Hanjalić et al. [63] formulated the $\zeta - f$ RANS model with the new variable $\zeta = \overline{v^2}/k$ instead of $\overline{v^2}$. This improvement leads to a weaker dependency of the model equations on wall distance. These nonlinear eddy viscosity models demonstrate significant improvements in capturing the influence of the near-wall anisotropy into the turbulent viscosity. However, the influence of the Reynolds stress anisotropy on the velocity field remains a weakness of these models. Although EVMs are commonly used in practical applications, they exhibit limitation in the prediction of some types of flows, for instance the flows with the dominance of large-scale anisotropic structures or rotational flows (for more information about the application of RANS models for different uses, see Frost [50] or Dervieux et al. [34]).

According to Leonard [91], most information on turbulent flows can be obtained from simulating the motion of large scales. For this reason, the scales can be separated by means of the filter operation, which is the main idea of the LES technique. Here, the instantaneous flow quantities are decomposed into resolved and unresolved (sub-grid) scales by introducing a spatial filtering. This general concept is based on the idea of self similarity suggested by Kolmogorov. This concept maintains that the large, energy-containing eddies are mostly determined by the geometric boundary conditions, while the smaller scales are more universal and can therefore be more easily modeled. A detailed overview of LES modeling is presented in Sagaut [136] and in Fröhlich [48]. Smagorinsky model, from 1963 [144], is among the most commonly applied and simplest of LES approaches. Following to Prandtl's idea, the sub-grid turbulent length scale in Smagorinsky model is set proportional to the grid spacing, and the relevant velocity scale is set proportional to the resolved velocity gradient. From this assumption follows the calculation without additional transport equations, and follows a simple implementation procedure. This model demonstrates quite good results for rather simple flow configurations, whereas for more complex scenarios, the modeling constant becomes flow dependent. Therefore Germano et al. [52] have suggested the so-called dynamic sub-grid scale, which is a modification of the simplest LES method with a variation of the Smagorinsky constant in space and time based on the filtering of flow quantities. This method has been widely investigated and extended in [96], [102]. The problem of applying the LES technique in the simulation of turbulent flows is a requirement of the very fine grid resolution in the wall vicinity, since the size of turbulent eddies is correspondingly reduced by approaching the solid surface. To reduce this impact, Nicoud and Ducros [115] proposed a wall-adapting local eddy-viscosity model (WALE). This model is capable of capturing the effects of the smallest resolved turbulent fluctuations in the near-wall region by means of the square of the velocity gradient tensor. In 1985, Yoshizawa and Horiuti [175] suggested a one-equation LES model. In this approach the transport equation for sub-grid turbulent kinetic energy is used to estimate the properties of the corresponding turbulent velocity scale. Although different LES models demonstrate the ability to predict correctly the different types of flows, the computational effort is by a factor from ten to 100 times larger than in RANS simulations, depending on the problem configuration. This high computational effort generally limits the application of LES techniques to an academic field. For instance, the simulation of complex flows,

like a flow around a full aircraft model, will remain out of reach for the next 30 years according to [147].

The limits of application for the LES techniques due to the required fine spatial and temporal resolution and the weaknesses of RANS methods in capturing the behavior of some kind of turbulent flows have led to the development of a new group of turbulence models, hybrid LES-RANS methods. These RANS-based models imitate the behavior of sub-grid-scale models generally by means of the introduction of the grid-spacing as a model parameter. Thereby, these approaches, denoted as eddy-resolving (ER) models, combine the advantages of the LES and RANS models and reduce the drawbacks of each. As a result, ER methods are able to capture the main turbulent flow behavior on a rather coarse mesh. The hybrid models suggested about 20 years ago are one of the central points in turbulence modeling research today.

The detached eddy simulation (DES) model, first proposed by Spalart et al. [149] for the simulation of massively separated flows, is the most popular hybrid turbulence model. The DES method has been successfully used for many complex turbulent flow tasks. In this approach, a RANS mode is applied near the solid boundaries, whereas in separated flow regions and regions far from the wall, the method switches to LES mode. In the beginning, this model was based on the Spalart-Allmaras approach [148], where the wall distance is replaced by a newly introduced length scale depending on the grid spacing and on the shear stress tensor. Since the switching has been realized depending on the grid and not on the flow, some modifications have been introduced in this hybrid model. These modifications led to the formation of delayed detached eddy simulation (DDES) [150] and improved delayed detached eddy simulation (IDDES) models [143]. The crucial issue in the application of DES-based methods is the so-called "gray area", in which an undefined modeling zone exists. In this region the solution is neither pure RANS nor pure LES [60].

One of the new hybrid models, the VLES, has been provided by Speziale [151]. This hybrid turbulence approach switches seamlessly between fully modeled RANS and fully resolved DNS modes depending on the numerical grid resolution. This method is also called flow simulation methodology [44], [73]. Johansen et al. [77] have proposed the application of a built-in function for the modification of the sub-grid scale turbulent viscosity. Since the original VLES model damped the Reynolds stress too much and required a rather fine mesh resolution, Han and Krajnović [60] suggested a new VLES approach by means of the modification of the built-in function (i.e. the resolution control function). This new hybrid model shows high efficiency and robustness in many applications already on relatively coarse grids [60], [59]. In these works, the $k-\varepsilon$ and $k-\omega$ based VLES methods have been investigated. In 2014, Chang et al. [24] suggested the modification of a built-in function by means of the introduction of the cut-off length scale, and they formulated the $\zeta - f$ based VLES method. This modification led to further improvement of the results obtained by the VLES model.

Other popular hybrid models include the scale adaptive simulation (SAS) model introduced by Menter and Egorov [104] and the partially averaging Navier-Stokes (PANS) method proposed by Girimaji [53]. The concept of the SAS method, which is an improved unsteady Reynolds-average Navier-Stokes (URANS) formulation presents the introduction of the von-Karman length scale into the turbulence scale equation (i.e. the ratio of the first to the second derivative of the velocity

field). This length scale allows the SAS approach to adapt dynamically to resolved structures in an URANS simulation, and as a result the LES-like behavior in unsteady regions. The idea behind the PANS method is to seamlessly switch between RANS and DNS, by means of the introduced ratio modeled to total turbulent properties.

Turbulence in fluid-structure interaction (FSI) problems

As mentioned at the beginning of this chapter, investigation of the turbulence phenomena in the context of FSI, especially with hybrid modeling techniques, is quite limited in comparison to research focusing on coupling algorithms and moving grid techniques.

A variety of publications from the work groups of Bazilevs et al. [8], Takizawa et al. [157] and Tezduyar and Sathe [160] are available. In these studies, different FSI applications are investigated in the field of aerodynamics. These groups most commonly apply special space-time computational techniques for simulations of wind turbines, flapping wings or parachutes. However the focus of these investigations lies on the numerical methods, and the aspect of turbulence is not a major issue.

The working group of Breuer et al. [20] has applied the LES model with an efficiently partitioned coupling scheme based on a predictor–corrector method to simulate different FSI problems [19], [21]. The application of DES hybrid modeling techniques has been discussed by this group in Münsch and Breuer [113]. They also performed different experiments suited for the validation of FSI codes and simulated them with the LES approach [80], [31], [30]. The LES method has demonstrated quite good agreement with the experimental data in these flow configurations.

Golshan et al. [54] have applied LES and RANS approaches for the simulation of wind- and wave-forced oceanic turbulence in unstratified shallow water. In this work, the influence of wall-modeling on the results is investigated in detail. In Das [27], FSI-URANS simulation results in marine applications being presented. Due to the small deformation of the investigated metallic propeller, the RANS method has demonstrated very good coincidence with measurement data.

From 2013-2016, the number of investigations of DES-based models in the context of FSI increased, although it remains small. The DES and LES based on the experiments from Breuer's group have been performed in [2], [124], [125]. Both models reproduce an acceptable agreement with the experimental data. Türk [163] has been studying a flow over the Lambie airfoil characterized by a mechanical coupling between the leading and trailing edge, with X-LES and URANS models. The hybrid X-LES model demonstrates the ability to capture the different turbulent structures. The investigation results for unsteady loads in a tube bundle by means of DES and URANS modeling techniques are reported in [142]. In [141] the $k-\omega$ SST and Spalart–Allmaras RANS models, as well as the modified DES approach, have been applied for the prediction of an aeroelastic phenomenon (namely turbulent flow over an Onera M6 wing at different angles of attack). The hybrid turbulence model has shown quite good results for all flow configurations, whereas the presented RANS models mainly failed to capture the separation at higher angles of attack.

Chang et al. [24] investigated the VLES model on a moving structure for the study of an internal combustion engine system. In this work, the capability of the VLES approach to capture the

swirling properties and the anisotropy of turbulent characteristics has been determined. To the best of the author's knowledge, the investigation of the VLES model in the context of fluid-structure interaction has not yet been presented in any publication.

2 Theoretical Foundations

In the following chapter, the essential theoretical foundations for this work are introduced. The first part outlines the foundation equations of fluid mechanics, which describe the behavior of the fluids. They are based on the mass, momentum and energy conservation laws. Together with the material law, the initial and the boundary conditions build the required basis for the computational fluid simulation. Subsequently, the arbitrary Lagrangian-Eulerian approach, together with the idea of the fluid-structure coupling, is sketched. Finally, at the end of this chapter, the properties of turbulent flows are summarized. General and deeper theories of fluid dynamics can be found in the textbook of Spurk [154] and Schäfer [138]. For a detailed review of the turbulent flows, please refer to the textbook of Pope [121] and Piquet [119].

2.1 Governing equations of fluid dynamics

2.1.1 Conservation of mass

According to the law of conservation of mass, the mass m of the material volumes V in the absence of sources and sinks stays constant:

$$\frac{D}{Dt}\int_V \rho \, dV = 0 \; . \tag{2.1}$$

The reformulation of the law in the differential form leads to *continuity equation*:

$$\frac{\partial \rho}{\partial t} + \frac{\partial \left(\rho u_i\right)}{\partial x_i} = 0 \; , \tag{2.2}$$

with ρ being the density and u_i the velocity components in the i-direction.

The fluid considered in the present work can be assumed as incompressible. This means $D\rho/Dt = 0$. To ensure the legitimacy of this assumption, the Mach number Ma is required to be smaller than 0.3:

$$Ma = \frac{U}{a} < 0.3 \; , \tag{2.3}$$

where U is the characteristic flow velocity and a is the speed of sound.

Under this condition the continuity equation (2.2) takes the following simplified form:

$$\frac{\partial u_i}{\partial x_i} = 0 \; . \tag{2.4}$$

In contrast to the calculation of compressible fluids, no energy equations have to be solved for the simulation of incompressible flows. The reason for that lies in the idealized assumption that the viscosity of incompressible fluids is independent from temperature. Therefore, the flow field and the temperature field are decoupled.

2.1.2 Conservation of linear momentum

The law of momentum conservation states that in an inertial frame, the temporal change of the momentum of a body is equal to the sum of all forces (surface and volume) applied to the body:

$$\underbrace{\frac{D}{Dt}\int\limits_{V}\rho u_i\,dV}_{momentum\,change} = \underbrace{\int\limits_{S}T_{ij}n_j\,dS}_{surface\,forces} + \underbrace{\int\limits_{V}\rho f_i\,dV}_{volume\,forces}\ , \tag{2.5}$$

with f_i being the volume forces, n_j the normal vector and T_{ij} the components of the Cauchy stress tensor T. After applying the Gauss integral theorem, equation (2.5) is converted to the following differential form:

$$\frac{\partial\left(\rho u_i\right)}{\partial t} + \frac{\partial(\rho u_i u_j)}{\partial x_j} = \frac{\partial T_{ij}}{\partial x_j} + \rho f_i\ . \tag{2.6}$$

2.1.3 Navier-Stokes equation

The Cauchy stress tensor T_{ij} included in equation (2.6) depends on the material quantities of the medium. As a linear viscous isotropic medium (Newtonian fluid) is used in the present work, the stress tensor T_{ij} in consideration of the incompressibility takes the following form:

$$T_{ij} = 2\mu S_{ij} - p\delta_{ij}\ , \tag{2.7}$$

where μ is the dynamic viscosity, δ_{ij} denotes the Kronecker delta, p is the pressure that arose as a new unknown quantity in the equation (2.6) and $\overline{S_{ij}}$ is the shear stress, which is defined as the following:

$$S_{ij} = \frac{1}{2}\left(\frac{\partial u_i}{\partial x_j} + \frac{\partial u_j}{\partial x_x}\right)\ . \tag{2.8}$$

After substituting the Cauchy stress tensor T in the conservation equation of linear momentum (2.6) through the material law (2.7) the equation (2.6) becomes

$$\rho\frac{\partial u_i}{\partial t} + \rho\frac{\partial(u_i u_j)}{\partial x_j} = \frac{\partial}{\partial x_j}\left[\mu\left(\frac{\partial u_i}{\partial x_j} + \frac{\partial u_j}{\partial x_i}\right)\right] - \frac{\partial p}{\partial x_j} + \rho f_i\ . \tag{2.9}$$

Equation (2.9) together with (2.4) builds *the incompressible Navier-Stokes equation* for the Newtonian fluids. This system serves as the foundation for the calculation of the fluid quantities, for example, pressure and velocity.

2.2 Arbitrary Lagrangian-Eulerian approach

The equations in the prior sections are formulated in the Eulerian system, which is commonly applied in the description of fluids, while the Lagrangian formulation is normally used for the description of motion in structural mechanics.

Both of the descriptions are not suitable in the case of the fluid-structure coupling. In the Lagrangian approach nodes of a computational grid move together with the appropriate material particles (Figure 2.1, top). Because of the large deformations of the fluid, this formulation is not optimal for FSI problems, as the large grid distortions lead to the destruction of the mesh in the Lagrangian algorithm. In the Eulerian description the grid is linked to the spatial coordinates (Figure 2.1, center), allowing for the handling of large distortions with the cost of the exact interface definition and the resolution of the flow details. However, for the FSI problem, the Eulerian formulations lose accuracy when applied to solids.

To solve this problem the arbitrary Lagrangian-Eulerian (ALE) approach is used, which is a combination of the prior described formulations. The idea of the ALE method is that the mesh is fixed on neither a spatial coordinate nor a material particle. Therefore, by the deformation, the computational grid has qualities of both formulations and moves in an arbitrarily specified manner (Figure 2.1, bottom). This formulation allows handling cases with great distortions of the continuum [35].

The ALE formulation enables the representation of the Navier-Stokes equations by the optional motion of the computational domain. For this, the fluid velocities u_i in the convective term of equation (2.9) are replaced with the velocities in the moving reference system $u_i - u_i^g$:

$$\rho\frac{\partial u_i}{\partial t} + \rho\frac{\partial}{\partial x_j}\left(u_i(u_j - u_j^g)\right) = \frac{\partial}{\partial x_j}\left[\mu\left(\frac{\partial u_i}{\partial x_j} + \frac{\partial u_j}{\partial x_i}\right)\right] - \frac{\partial p}{\partial x_j} + \rho f_i \ . \tag{2.10}$$

with u_i^g denoting the velocity of the moving grid.

Together with continuity equation (2.4), expression 2.10 builds the Navier-Stokes equations in the ALE formulation, which returns to the Eulerian formulation, if the system is not moved ($u_i^g = 0$) and to the Lagrangian approach, if u_i becomes the material velocity.

According to [161], the space conservation law is applied in order to ensure that equation (2.10) is fulfilled:

$$\frac{\partial}{\partial t}\int_V \rho dV = \int_S \rho u_i^g n_i dS \ . \tag{2.11}$$

To guarantee that equation (2.10) holds for a non-moving fluid in every time step, this condition 2.11 must be fulfilled by the numerical scheme [33]. For detailed information concerning the formulation of the foundation equations in the arbitrary system, refer to Warsi [168].

2.3 Fluid-structure coupling

Let Ω be a computational FSI domain described in the ALE framework, which consists of the structure domain Ω_s and the fluid domain Ω_f. These two domains have a common boundary $\Gamma_{FSI} = \Omega_s \cap \Omega_f$ (Figure 2.2). Subscript f refers to the fluid and subscript s to the structure.

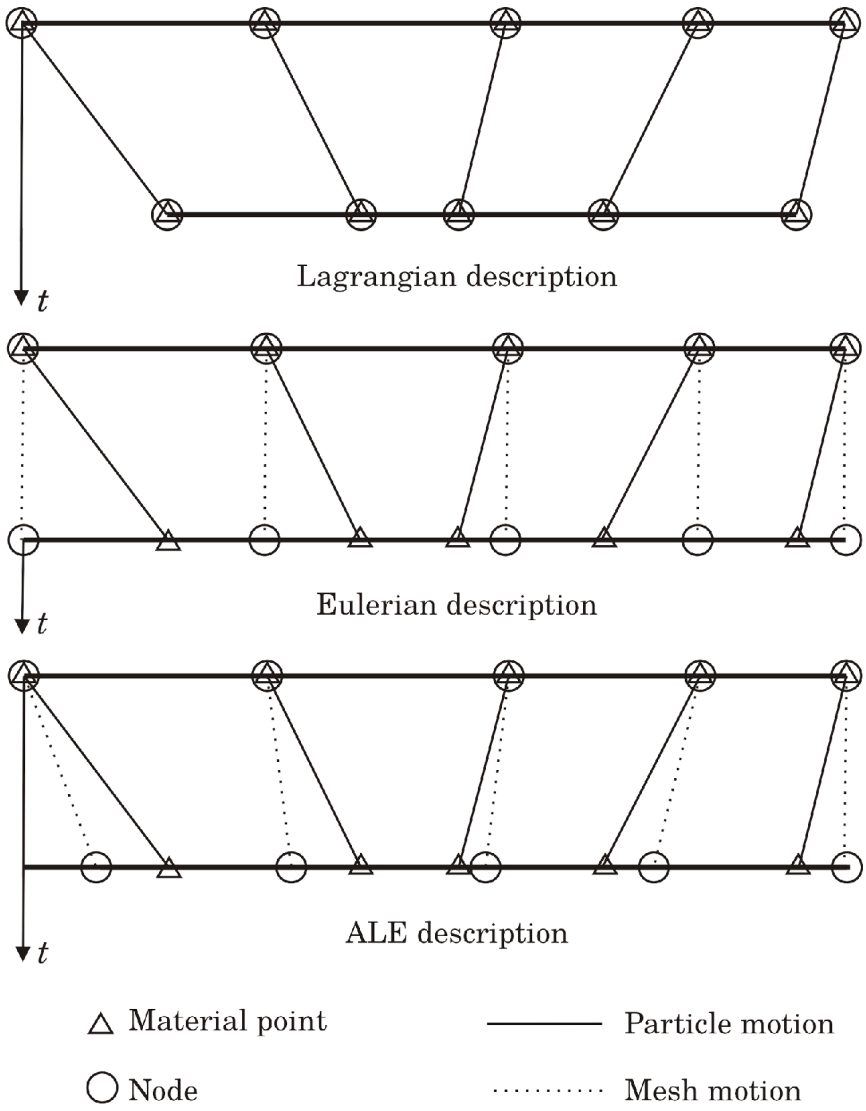

Figure 2.1: Lagrangian, Eulerian and ALE formulation [35].

On the coupling boundary Γ_{FSI} additional boundary conditions for velocities and stresses are imposed:

$$u_i^f = u_i^s \, , \tau_{ij}^s \, n_i = \tau_{ij}^f \, n_i. \tag{2.12}$$

For a mathematical description of the FSI phenomena, the fluid and the structure continuum mechanical problems have to be combined. The basic fluid dynamics equations (Section 2.1) and the basic structure equations (see [172]) are extended with additional terms, which contain the values arising from the interactions with the respective fields. This can be expressed in the following non-linear coupled equations system:

$$\begin{bmatrix} A^f & A^{fs} \\ A^{sf} & A^s \end{bmatrix} \begin{bmatrix} \phi^f \\ \phi^s \end{bmatrix} = \begin{bmatrix} b^f \\ b^s \end{bmatrix} \, . \tag{2.13}$$

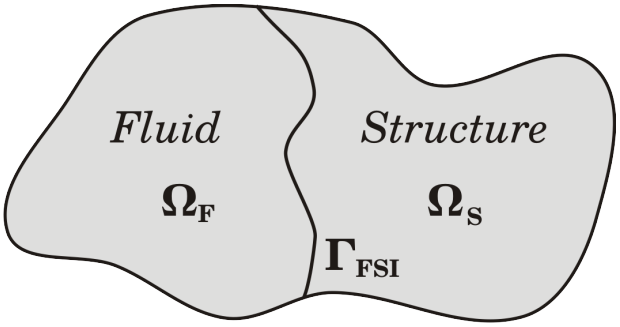

Figure 2.2: Schematic presentation of FSI domain.

In this system, the flow unknowns are denoted with ϕ^f and the structure unknowns with ϕ^s. The A^{fs} and A^{sf} are the new terms arising from the effect of the fluid on the structure and the structure on the fluid, respectively. Different coupling techniques for solving the system of equations (2.3) are described in Chapter 1. Detailed information to this topic can be found in [7] and [146].

2.4 Foundation of turbulent flows

This section describes the phenomenon of turbulence in flows. All well-known flows can be subdivided into two groups. The first group contains the laminar flows, where the fluid flows regularly in parallel layers. The second group contains the turbulent flows, which are characterized by instationarity, three-dimensionality and rapid movement of fluid particles. This behavior is caused by irregular field gradients in the fluid field, for example, velocity gradient. These two flows can be distinguished by means of the Reynolds number Re [126], which is defined as the ratio of inertial forces to viscous forces:

$$Re = \frac{UL\rho}{\mu}, \tag{2.14}$$

with the characteristic velocity U, the characteristic linear dimension L, the density ρ and the dynamic viscosity of the fluid μ. The laminar regime occurs below a certain problem-dependent critical Reynolds number Re_{cr}, where the viscous forces are dominant and damp the small disturbances. Above the critical Reynolds number, the inertial forces are dominant and the turbulent regime occurs. For a pipe flow, as investigated by Reynolds [127], the value of the critical Reynolds number is $Re_{cr} \approx 2300$. In experiments, laminar flows can be achieved up to $Re_{cr} \approx 40,000$ by means of a carefully calmed inflow [154]. Biswas and Eswaran [13], Davidson [28] or Pope [121] provides detailed information about turbulent flows.

2.4.1 Turbulence energy cascade

The basic concept for the understanding of the phenomenon of turbulence is the energy cascade, which was first expressed by Lewis F. Richardson in the 1920s [129]. According to this concept,

turbulent flow consists of three-dimensional vortices, also called eddies, of various sizes. The large vortices, which contain the main part of the kinetic energy, decay into smaller eddies by the process of vortex stretching. As a result, the energy is continuously transferred from the large vortices to the smallest turbulent scales, where the kinetic energy of turbulent motion dissipates.

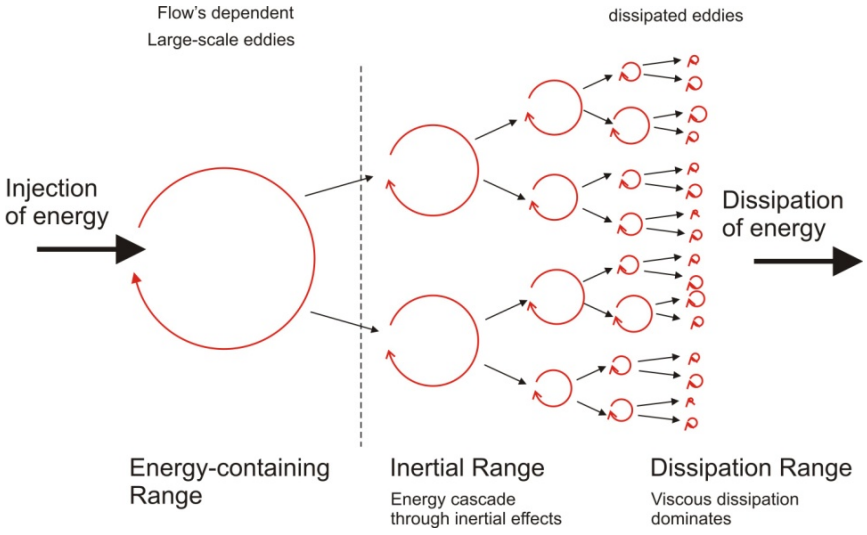

Figure 2.3: Schematic diagram of the energy transfer and regions of the turbulent energy cascade.

This continuous decay of the eddies towards smaller eddies was investigated in detail by Kolmogorov and was formulated into three hypotheses ([84]). The schematic diagram of the energy cascade is given in Figure 2.3. All of the turbulent structures can be subdivided into three groups. The first one consists of vortices which are influenced by the order of the characteristic length of the problem domain. The eddies in this range are determined only through the boundary condition and are thereby anisotropic and inhomogeneous. As the large structures hold a substantial part of the energy, they have an enormous influence on the flow. The second part, denoted as inertial range, includes the turbulent structures, which are no longer dependent on the boundary conditions at a sufficiently large Reynolds number. The smallest eddies are located in the dissipation range. Turbulent structures in this part are determined by the dissipation of the flow and the viscosity; they can be treated as locally isotropic and homogeneous. In contrast to the large anisotropic eddies, the small structure can be modeled due to this local universality. These three ranges can be distinguished through the typical scales, which are described in more detail in the next section.

2.4.2 Turbulent scales

The length and time scales play an important role in the description of different ranges of the energy cascade. The length scale l_0, time scale τ_0 and velocity scale u_0 of large energy-containing eddies can be estimated by means of k and ε:

$$l_0 = k^{3/2}/\varepsilon \,, \quad u_0 = k^{1/2} \,, \quad \tau_0 = k/\varepsilon \,. \tag{2.15}$$

In considering Kolmogorov's theory, the movement of the small scales is locally isotropic and homogeneous at high Reynolds numbers. The statistic of this movement has a universal character and can be described only through the kinematic viscosity ν and the dissipation ε. From a dimension analysis, it can be observed that the smallest eddies are characterized by following scales, which are denoted *Kolmogorov scale* [84]:

$$\eta = \left(\frac{\nu^3}{\epsilon}\right)^{1/4} \,, \quad u_\eta = (\nu\varepsilon)^{1/4} \,, \quad \tau_\eta = \left(\frac{\nu}{\varepsilon}\right)^{1/2} \,, \tag{2.16}$$

where η is a length scale, u_η is a velocity scale and τ_η is a time scale. The Reynolds number formed from these scales is equal to one: $(\eta u_\eta)/\nu = 1$. This illustrates that, on the smallest scale, the Reynolds number is small enough for dissipation to be effective.

From the ratio of the smallest (η, u_η, τ_η) to the largest scales (l_0, u_0, τ_0), it can be observed that the smallest scales reduce in size compared to the largest ones if the Reynolds number of the flow increases:

$$\eta/l_0 \propto Re^{-3/4} \,, \quad u_\eta/u_0 \propto Re^{-1/4} \,, \quad \tau_\eta/\tau_0 \propto Re^{-1/2} \,, \tag{2.17}$$

The Taylor microscale falls in between the large scale and small scale eddies. Its characteristic length, velocity and time scale can be calculated by

$$\lambda = \sqrt{10\,\nu\frac{k}{\varepsilon}} \,, \quad u_\lambda = k^{1/2} \,, \quad \tau_\lambda = \left(\frac{\nu}{\varepsilon}\right)^{1/2} \,. \tag{2.18}$$

Taylor scales are related to the dissipation energy, but do not have an exact relation to the size of the small eddies. The ratio of the Taylor scale to the Kolmogorov's dissipation scale can be estimated as follows:

$$\lambda/\eta \approx Re^{1/4} \,. \tag{2.19}$$

2.4.3 Energy spectrum

Based on the idea of the energy cascade, Kolmogorov ([84]) theoretically derived the energy spectrum, which allows one to investigate of the distribution of energy over the different scales. Therefore, the energy spectrum $E(\kappa)$ is considered as a function of a so-called wavenumber, where the wavenumber of a particular length scale κ is defined as $\kappa = 2\pi/l$. Figure 2.4 schematically demonstrates the energy spectrum. In accordance with the concept described in Section 2.4.1 the energy spectrum can be subdivided into three ranges. Each of them is characterized by corresponding scales, which are listed in the previous section. For a detailed description of the turbulent spectrum, see [121].

Kolmogorov also derived the shape of the spectrum in the inertial range using the dimensional analysis and formulated the Kolmogorov's $\kappa^{-5/3}$ law for this range:

$$E(\kappa) \propto \kappa^{-5/3}.$$

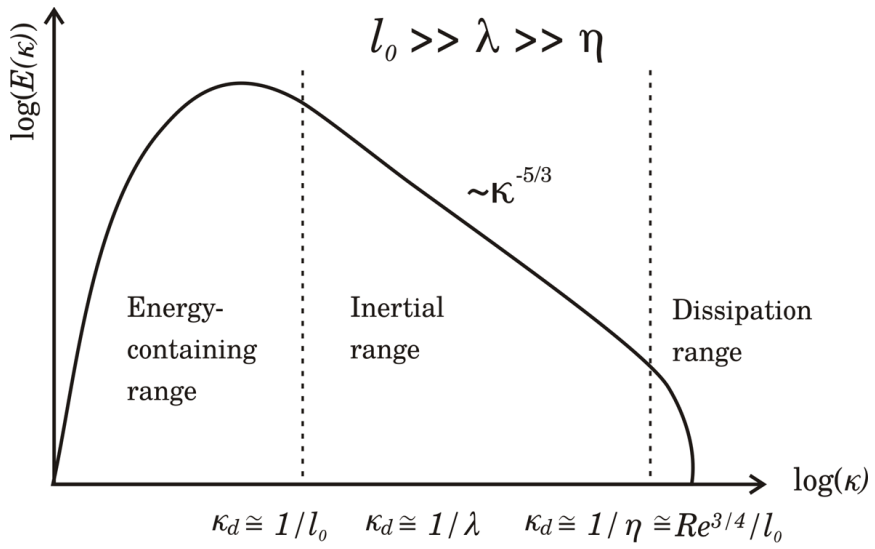

Figure 2.4: Schematic diagram of the energy spectrum.

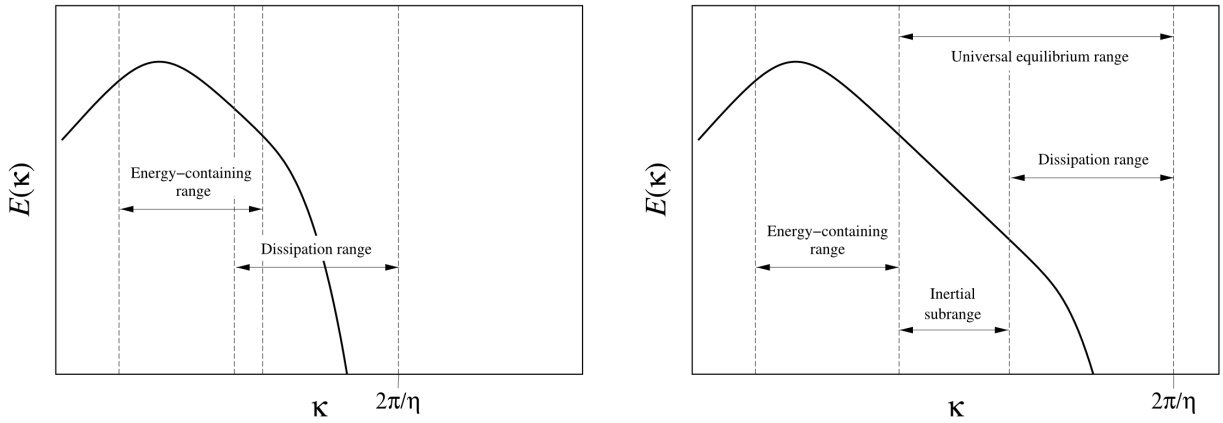

Figure 2.5: Energy spectra for varying turbulence Reynolds number [110].

For higher Reynolds numbers, the span of the wavenumbers over which the $\kappa^{-5/3}$ law holds is broader. As result of an overlap of the energy-containing range and dissipation range at lower Reynolds numbers, this $\kappa^{-5/3}$ law region being eliminated. Figure 2.5 demonstrates this influence of different Reynolds numbers on the energy spectra.

The concept of the energy cascade and the energy spectrum are a basis for the turbulence modeling (see Chapter 3).

2.4.4 Wall treatment

Many typical flow problems in engineering are bounded by solid interfaces, for example, the flow through pipes or the flow around airfoils. Consequently, the wall treatment is a very important aspect in turbulence modeling.

The effect, which occurs in a turbulent flow in the near of boundaries, is a damping of the fluctuations in the wall-normal direction and an amplification of these in the tangential direction. As the viscous effects are dominant in the vicinity of solid surface, the wall shear stress τ_w together with the molecular viscosity ν plays an important role in the wall-bounded flows. The description of the turbulence near the wall can be determined using these two quantities. The mean wall friction velocity and the viscose lengthscale are defined as

$$u_\tau = \sqrt{\frac{\tau_w}{\rho}} , \quad \text{with} \quad \tau_w = \mu \frac{\partial u}{\partial y}|_w . \tag{2.20}$$

The non-dimensional values for the wall distance y^+ and the mean velocity u^+ are formulated using the equation for u_τ:

$$y^+ = \frac{y u_\tau}{\mu} \quad \text{and} \quad u^+ = \frac{\overline{u}}{u_\tau} . \tag{2.21}$$

From this formulation, a similarity of $y+$ to the definition of the Reynolds number is well recognized. With $y^+ \approx 1$, the local Reynolds number corresponds to the Kolmogorov scales (see Equation 2.4.2).

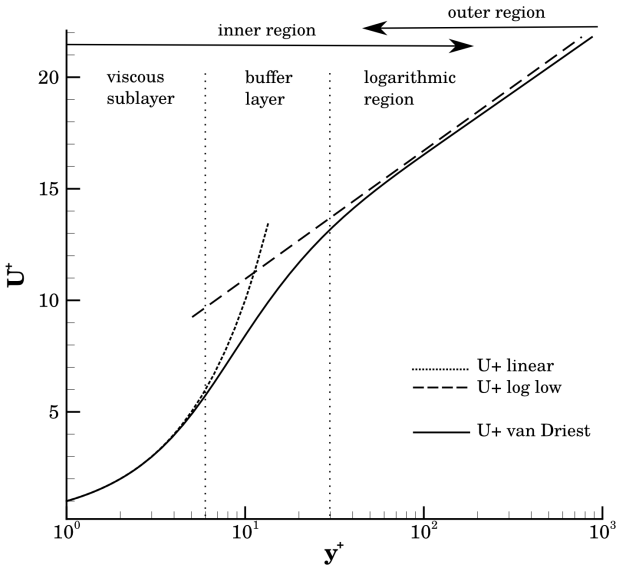

Figure 2.6: Velocity profiles in the near-wall region. Linear region, log-law region and the profiles from van Driest [164].

By means of the non-dimensional wall distance y^+, the near-wall region can be subdivided into three different layers, which are characterized by different physical phenomena:

- Viscous sublayer: $0 < y^+ < 5$. In comparison to the viscous stress the Reynolds stresses are negligible. The non-dimensional mean velocity profile is determined as $u^+ = y^+$.
- Buffer layer: $5 < y^+ < 30$. The transition region. The viscous and turbulent effects are of the same order.
- Log-law layer: $30 < y^+$. The log-law of von Karman [139] is applied:

$$u^+ = \frac{1}{\kappa} \ln y^+ + B, \tag{2.22}$$

  whereκ is the von Karman constant and $B = 5.2$.

The form of the mean velocity profiles in the different boundary regions is illustrated in Figure 2.6.

3 Modeling of Turbulent Flows

Turbulence is a continuum mechanical phenomenon and therefore can be described and resolved with the Navier-Stokes equations without further modeling. This method is denoted as a direct numerical simulation (DNS) (Figure 3.1 [a]). The DNS requires a resolution of the computational domain, which lies below the smallest eddy size. To estimate the order of computational cost, the number of required grid cells should be determined. This is done by calculating the scales ratio of the smallest turbulence structures to the elements of the integration region (Section 2.4.2). From this estimation, it can be determined that the required number of grid points N is proportional to $Re^{3/4}$ and that the computational cost is proportional to $Re^{11/4}$. Consequently, the current use of DNS is limited to problems with low Reynolds numbers and simple geometry.

To reduce the computational cost, different modeling techniques have been developed.For example, the large eddy simulation (LES) model was initially proposed in 1963 by Joseph Smagorinsky [144]. In this approach, only the large, energy containing anisotropic scales are simulated, while the small universal eddies are modeled (figure 3.1 [b]). For the subdivision of the scales into large and small, spatial filtering is applied [48]. This concept allows for a reduction of the computational cost in comparison to the DNS (Section 3.2).

For industrial applications, it is often sufficient to utilize a statistical description of turbulent flows, which takes the average impact of the turbulence into consideration. To calculate the mean values of unknowns, it is sufficient to model all turbulent structures (Figure 3.1 [d]). The corresponding models are denoted as the Reynolds-average Navier-Stokes (RANS) model [121]. This approach allows for a significant reduction of the computational time. However, the resulting accuracy is inadequate for describing some types of turbulent flows. The RANS models are explained in detail in Section 3.1.

In the last fifteen years, hybrid models have become extremely popular. They combine the advantages of the basic models described above in order to obtain sufficient results with limited computational cost [49] (Figure 3.1 [c]). The most popular hybrid turbulence model, which has also been successfully used for many complex turbulent flow tasks, is the detached eddy simulation (DES). First proposed by Spalart et al. [149], this model combines a RANS mode in the attached boundary layers with LES in separated regions and in regions far from the wall. The complication of applying the DES is that it creates a "gray area", in which an undefined modeling zone exists, where the solution is neither pure RANS nor pure LES [60].

Another kind of hybrid methodology, the so-called very large eddy simulation (VLES), was proposed by Speziale [151]. This model provides a seamless change from RANS to DNS depending on the numerical resolution. However, the original VLES model damped the Reynolds stress excessively and required a fine mesh resolution. Therefore, modifications were proposed in [60] or [24]; after these changes the VLES model demonstrated high efficiency and a robustness in

many applications [59], [58], [24].

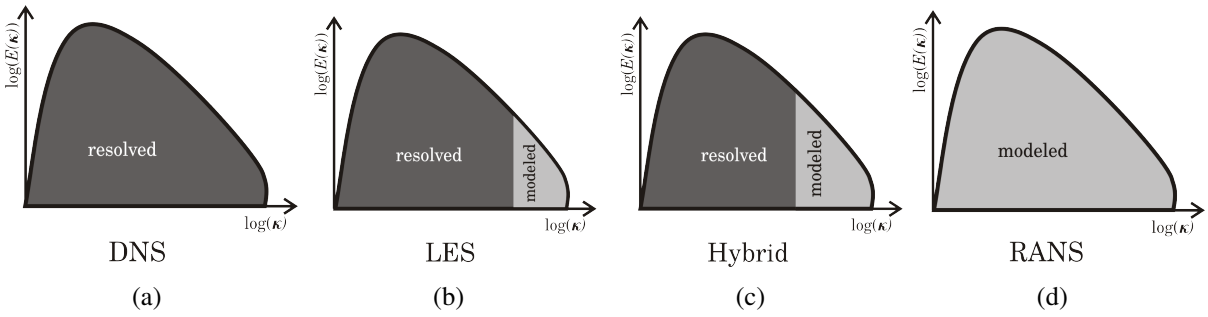

Figure 3.1: Schematic presentation of turbulent models by means of energy cascade.

In the beginning of this chapter, the description of the RANS concept is sketched and three types of RANS models are presented in detail. A brief overview of the LES can be found in Section 3.2 in order to understand the idea of the VLES approach. As the VLES model is of central interest for this work, it is presented in detail at the end of this chapter.

3.1 Reynolds-averaged Navier-Stokes equation models

As mentioned in the introduction to this chapter, instead of the complete unsteady information, the behavior of the statistical means of the flow is sufficient for many technical applications. To model the flow in such a way, statistical turbulence models, referred to as Reynolds-average Navier-Stokes (RANS), are utilized. In the statistical modeling, all turbulent structures, along with large anisotropic vortices, are treated as isotropic, which is in contrast to the physics described in Section 2.4.1. This can lead to unsatisfactory results in some kinds of flows, especially in flows with separations [173].

3.1.1 Averaging of the foundation equations

For averaging the foundation equations described in Chapter 2, a stochastic approach is used, which means that, apart from the averaged part $\overline{\phi}(x,t)$, a fluctuating part $\phi'(x,t)$ of a quantity exists. This separation was suggested by Reynolds [128] and is valid for the velocities as well as for the pressure and other field quantities in the following form:

$$\phi(x,t) = \overline{\phi}(x,t) + \phi'(x,t) \ , \tag{3.1}$$

where the average value $\overline{\phi}(x,t)$ is determined by means of the ensemble averaging

$$\overline{\phi}(x,t) = \lim_{n\to\infty} \frac{1}{n} \sum_{k=1}^{n} \phi_k(x,t) \ . \tag{3.2}$$

For this, the experiment is conducted n-times and the values are measured n-times in the same place over a sufficiently long time period (Figure 3.2).

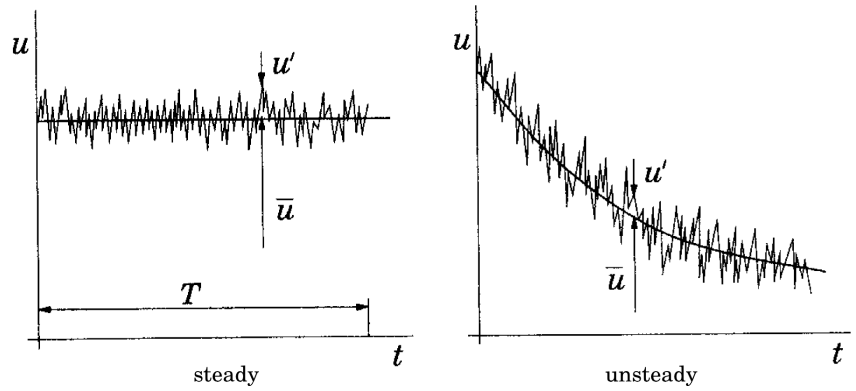

Figure 3.2: Stochastic steady and unsteady averaging of the flow [45].

In the stochastic steady case (Figure 3.2 left), the time averaging is used instead of the ensemble averaging

$$\overline{\phi}(x) = \lim_{T\to\infty} \frac{1}{T} \int_0^T \phi(x,t)dt \ . \tag{3.3}$$

The insertion of the Reynolds decomposition (3.1) in the Navier-Stokes equations (2.2), (2.9) and following time averaging of these equations leads to the *Reynolds - averaged Navier - Stokes equations* (RANS-equations):

$$\frac{\partial \overline{u_i}}{\partial x_i} = 0 \ , \tag{3.4}$$

$$\rho \frac{\partial \left(\overline{u_i}\right)}{\partial t} + \rho \frac{\partial \overline{u_i u_j}}{\partial x_j} = \frac{\partial}{\partial x_j} \left(\mu \frac{\partial \overline{u_i}}{\partial x_j} - \rho \overline{u_i' u_j'} \right) - \frac{\partial \overline{p}}{\partial x_j} + \rho \overline{f_i} \ . \tag{3.5}$$

By averaging, a new unknown term $\rho\overline{u_i'u_j'}$, which is denoted as *the Reynolds stress*, arises from the non-linear convective term in the equation (2.9). Due to the additional term the system of equations (3.4) and (3.5) contains more unknowns than equations, whereby the system is no longer closed. The goal of turbulence modeling is an approximation of the unknown terms and thereby the closure of the problem.

There are two classes of models, which are approximations of the Reynolds stresses: the *Reynolds stress equation* (RSM) and the *eddy viscosity* models. In the first group of models, the further transport equations for the unknown terms $\rho\overline{u_i'u_j'}$ are solved and the Reynolds stresses are directly computed. Eddy viscosity models, on the other hand, are based on the modeling of the $\rho\overline{u_i'u_j'}$ term by means of the Boussinesq approximation [16]:

$$\tau_{ij}^{turb} = -\rho\overline{u_i'u_j'} = 2\mu_t\overline{S_{ij}} - \frac{2}{3}\rho k\delta_{ij} \quad \text{with} \quad \overline{S_{ij}} = \frac{\partial \overline{u_j}}{\partial x_i} + \frac{\partial \overline{u_i}}{\partial x_j} \ , \tag{3.6}$$

where $k = 1/2\ \overline{u_i' u_i'}$ is *the turbulent kinetic energy*, which characterizes the intensity of turbulent flows.

The consequence of the Boussinesq hypothesis is a changed viscosity, which consists of a molecular and a turbulent part (eddy viscosity). While the molecular viscosity is a thermodynamic property of a fluid, the eddy viscosity is dependent on the local flow characteristic. The modeling of the turbulent viscosity is a central task of the corresponding turbulence model. Depending on the number of equations solved for the computation of the eddy viscosity, the models are zero, one or two equation models. Within this study, only different kinds of two equation models are applied, which are described in detail in the following subsections.

3.1.2 The Chien low Reynolds number $k - \varepsilon$ model

Two equation models are commonly used in different application fields. The most popular two equation model is the $k - \varepsilon$ model. It was developed by Jones and Launder [79] and uses additional transport equations for the turbulent kinetic energy k and the dissipation of the turbulent kinetic energy ε to represent the turbulent properties of the flow. In many cases, the $k - \varepsilon$ model shows numerical instability and inaccuracy, since the numerical control of the stability in the near wall region for this approach is difficult. To provide the prediction of the flow down to the solid wall, Chien [25] modified the standard $k - \varepsilon$ model of Jones and Launder [79], resulting in the following transport equations for k and ε:

$$\rho \frac{\partial k}{\partial t} + \rho u_j \frac{\partial k}{\partial x_j} = \frac{\partial}{\partial x_j}\left[\left(\mu + \frac{\mu_t}{\sigma_k}\right)\frac{\partial k}{\partial x_j}\right] + P_k - \rho\varepsilon - 2\nu\frac{k}{y^2}\,, \tag{3.7}$$

$$\rho \frac{\partial \varepsilon}{\partial t} + \rho u_j \frac{\partial \varepsilon}{\partial x_j} = \frac{\partial}{\partial x_j}\left[\left(\mu + \frac{\mu_t}{\sigma_\varepsilon}\right)\frac{\partial \varepsilon}{\partial x_j}\right] + C_{\varepsilon_1} P_k \frac{\varepsilon}{k} - \varepsilon\rho\left(\frac{C_{\varepsilon_2} f_\varepsilon}{k} - \frac{2\nu}{y^2} e^{-0.5\ y^+}\right)\,, \tag{3.8}$$

with the production term

$$P_k = 2\mu_t S_{ij} S_{ji} \tag{3.9}$$

and the damping function

$$f_\varepsilon = 1 - 0.22 e^{-Re_T/6},\ \text{with}\ Re_T = \frac{\rho k^2}{\mu\varepsilon}\,. \tag{3.10}$$

The turbulent eddy viscosity in the Chien $k - \varepsilon$ model is defined as

$$\mu_t = C_\mu f_\mu \frac{\rho k^2}{\varepsilon}, \quad f_\mu = 1 - e^{-0.0115 y^+}\,. \tag{3.11}$$

The function f_μ helps to improve the results in the near wall region.
The values of constants can be found in Table 3.1.
This modification of the standard model leads to a reduction of the computational time, by means of the better convergence behavior in the wall near region. However in the case of complex geometries, the application of this model can lead to inaccuracies, as the correct detection of the wall distance y is problematic to determine [83].

σ_k	σ_ε	C_μ	C_{ε_1}	C_{ε_2}
1.0	1.3	0.09	1.36	1.80

Table 3.1: Model constants for the Chien $k-\varepsilon$ model [25]

.

3.1.3 The Wilcox $k-\omega$ model

Apart from many variations of the $k-\varepsilon$ model a wide range of other methods has been developed to improve the modeling in a physical and numerical sense [103]. A successful alternative to the $k-\varepsilon$ model is the $k-\omega$ approach, which was mentioned by Kolmogorov [85] and was modified by Wilcox [169], [170]. In contrast to the $k-\varepsilon$ approach, this model does not require the damping function near the wall and can therefore be integrated down to the viscous layer. However the $k-\omega$ approach demonstrates the weakness in the simulation of the flows with pressure induced separations [105].
In the Wilcox $k-\omega$ model, transport equations are solved for two turbulent quantities: the turbulent kinetic energy k and the specific dissipation ω

$$\rho\frac{\partial k}{\partial t}+\rho u_j\frac{\partial k}{\partial x_j}=P_k-\beta^*\rho k\omega+\frac{\partial}{\partial x_j}\left[(\mu+\sigma_k\mu_t)\frac{\partial k}{\partial x_j}\right], \tag{3.12}$$

$$\rho\frac{\partial \omega}{\partial t}+\rho u_j\frac{\partial \omega}{\partial x_j}=\gamma\frac{\omega}{k}P_k-\beta\rho\omega^2+\frac{\partial}{\partial x_j}\left[(\mu+\sigma_\omega\mu_t)\frac{\partial \omega}{\partial x_j}\right]. \tag{3.13}$$

The turbulent viscosity in this model is determined through k and ω

$$\mu_t=\frac{\rho k}{\omega}. \tag{3.14}$$

The relation between the dissipation ε and the specific dissipation ω or rather the time scale τ_0^{-1} is determined by the following equation:

$$\omega=\frac{\varepsilon}{k}=\tau_0^{-1}. \tag{3.15}$$

The values of the model constants for the Wilcox model from the year 1988 are presented in Table 3.2.

σ_k	σ_ω	β^*	β	γ
$0,5$	$0,5$	$0,09$	$3/40$	$5/9$

Table 3.2: Model constants for the Wilcox $k-\omega$ model [169]

3.1.4 The $k-\varepsilon-\zeta-f$ model

The $k-\varepsilon-\zeta-f$ RANS model (further $\zeta-f$ model) was developed by Hanjalic et al. [63]. The concept of this four equation model is based on the $\overline{v^2}-f$ model of Durbin [39]. Besides the transport equations for k and ε, a transport equation for the velocity scale ratio $\zeta=\overline{v^2}/k$ and an equation for the elliptic relaxation function f needs to be solved:

$$\rho\frac{\partial k}{\partial t}+\rho u_j\frac{\partial k}{\partial x_j}=P_k-\rho\varepsilon+\frac{\partial}{\partial x_j}\left[\left(\mu+\frac{\mu_t}{\sigma_k}\frac{\partial k}{\partial x_j}\right)\right], \tag{3.16}$$

$$\rho\frac{\partial \varepsilon}{\partial t}+\rho u_j\frac{\partial \varepsilon}{\partial x_j}=\frac{C_{\varepsilon_1}P_k-C_{\varepsilon_2}\varepsilon\rho}{\tau_\zeta}+\frac{\partial}{\partial x_j}\left[\left(\mu+\frac{\mu_t}{\sigma_\varepsilon}\frac{\partial \varepsilon}{\partial x_j}\right)\right], \tag{3.17}$$

$$\rho\frac{\partial \zeta}{\partial t}+\rho u_j\frac{\partial \zeta}{\partial x_j}=f\rho-P_k\frac{\zeta}{k}+\frac{\partial}{\partial x_j}\left[\left(\mu+\frac{\mu_t}{\sigma_\zeta}\frac{\partial \zeta}{\partial x_j}\right)\right], \tag{3.18}$$

$$L_\zeta^2\Delta f-f=\frac{1}{\tau_\zeta}\left(C_1+C_2\frac{P}{\varepsilon}\left(\zeta-\frac{2}{3}\right)\right). \tag{3.19}$$

Equation (3.18) for function f is formulated by means of the pressure-strain model of Speziale et al. [153] and is used to adjust the wall reflection term of the pressure-strain correlation.

The corresponding turbulent viscosity in this eddy-viscosity-based model is modified through the introduction of the quantity ζ, which can be interpreted as the ratio of the wall-normal turbulent time scale $\tau_v=\overline{v^2}/\varepsilon$ to the general turbulent time scales $\tau=k/\varepsilon$:

$$\nu_t=C_\mu^\zeta\zeta k\tau_\zeta\ . \tag{3.20}$$

Since the velocity scale ratio contains the Reynolds stress component perpendicular to the wall, the near wall anisotropy is partially incorporated. This modification improves the determination of the viscosity [122]. And, as a result, the $\zeta-f$ model yields better results for wall-bounded flows in comparison to the models with damping functions, for example, the Chien $k-\varepsilon$ model [59].

The model is completed by limiting the time and length scales with the Kolmogorov scales as a lower bound and the Durbin's realisability constants [38] as an upper bound:

$$\tau_\zeta=\max\left[\min\left(\frac{k}{\varepsilon},\frac{a}{\sqrt{6}C_\mu\mid S\mid\zeta}\right),C_\tau\left(\frac{\nu}{\varepsilon}\right)^{1/2}\right] \tag{3.21}$$

$$L_\zeta=C_L\max\left[\min\left(\frac{k^{3/2}}{\varepsilon},\frac{k^{1/2}}{\sqrt{6}C_\mu\mid S\mid\zeta}\right),C_\eta\left(\frac{\nu^3}{\varepsilon}\right)^{1/4}\right] \tag{3.22}$$

The model coefficients are listed in Table 3.3.

3.2 Large eddy simulation

The idea of the large eddy simulation (LES) model arises from the Kolmogorov hypotheses (see Section 2.4.3). In this approach, the large three-dimensional anisotropic structures (grid scale)

C_μ	C_{ε_1}	C_{ε_2}	c_1	C_2'	σ_k	σ_ε	σ_ζ	C_τ	C_L	C_η
0.22	$1.4\,(1+0.012/\zeta)$	1.9	0.4	0.65	1	1.3	1.2	6.0	0.36	85

Table 3.3: Model constants for the $\zeta - f$ model.

are resolved, while the small isotropic eddies (sub-grid scale) are modeled. The distinction between the large and small eddies is accomplished by the spatial filtering procedure. The filtering operator is defined by means of the filter function $G(r, x_i, \Delta)$ [91]:

$$\tilde{\phi}_i(x_i, t) = \int_V G(r, x_i, \Delta) f(x_i - r, t) dr \ , \tag{3.23}$$

where Δ is a spatial dependent filter width, which in order is set equivalent to the numerical grid size. The filter width indicates the size of smallest resolved eddies and has explicit dependency on the filter function. The most commonly used explicit filter functions are the Gaussian and top-hat filters. It is important to mention, that the filtering operator has a different properties than the averaging operator in the RANS formulation. Detailed information about the filtering is found in [121].

To derive the transport equations for the LES approach, the flow quantities are decomposed into the resolved (filtered) part $\tilde{f}_i$ and the modeled (sub-grid scale) part f' :

$$\phi_i = \tilde{\phi}_i + \phi_i' \ , \tag{3.24}$$

After inserting this decomposition into the Navier-Stokes equations (2.9) and (2.2), and filtering these equations, the *filtered Navier-Stokes equations* are obtained:

$$\frac{\partial \tilde{u}_i}{\partial x_i} = 0 \ , \tag{3.25}$$

$$\frac{\partial \tilde{u}_i}{\partial t} + \frac{\partial (\tilde{u}_i \tilde{u}_j)}{\partial x_j} = \frac{\partial}{\partial x_j} \left(\nu \frac{\partial \tilde{u}_i}{\partial x_j} \right) - \frac{1}{\rho} \frac{\partial \tilde{p}}{\partial x_j} + \frac{1}{\rho} \frac{\partial \tau_{ij}^{LES}}{\partial x_j} \ . \tag{3.26}$$

It is recognized that the LES equations (3.25) and (3.26) have a similar form to the RANS equations (3.4) and (3.5). The term $\widetilde{\tau_{ij}}$ is an analog to the Reynolds stress tensor (3.6) and in LES case is denoted as a *sub-grid-stress* tensor:

$$\widetilde{\tau_{ij}} = \widetilde{u_i} \widetilde{u_j} - \widetilde{u_i u_j} \ . \tag{3.27}$$

As in the case of the RANS equations (see Section 3.1), a closure problem arises for the LES equations (3.25) and (3.26). The task of the LES method is the modeling of the sub-grid stress term (3.27) in order to solve this problem. A detailed description of the theory concerning the LES and the filter operator can be found in Fröhlich [48].

It is important to notice, that the filtering procedure in the large eddy simulation can be implicit or explicit. Implicit filtering is carried out by the grid itself and the grid is assumed as a LES filter. In explicit filtering, one of mentioned spatial filtering operators is used. In some LES models it is required to compute the sub-grid stress tensor [52].

The most common and easiest fine structure model was formulated by Smagorinsky [144] and is the basis for many other LES approaches [121]. The first SGS model assumes, that the energy production and dissipation of the small scales are in equilibrium. Based on this idea, the eddy viscosity approach is defined as following:

$$\widetilde{\tau_{ij}} = -2\nu_t \tilde{S_{ij}} \ , \tag{3.28}$$

with the turbulent viscosity directly proportional to the filter width (corresponding conventionally to the grid spacing):

$$\nu_t = (l_{LES})^2 \sqrt{2\tilde{S_{ij}}\tilde{S_{ij}}} = (C_S \Delta)^2 \sqrt{2\tilde{S_{ij}}\tilde{S_{ij}}} \ , \tag{3.29}$$

where C_s is a case-depending constant, $\tilde{S_{ij}}$ describes the large scale strain-rate tensor and l_{LES} is the Smagorinsky length scale. The equations of this SGS model can be solved without the explicit specification of the filtering operator.

For the filter width Δ, one of the following definitions can be used:

$$\Delta = (\Delta_x \Delta_y \Delta_z)^{1/3} \quad \text{or} \tag{3.30}$$

$$\Delta = \max(\Delta_x; \Delta_y; \Delta_z), \tag{3.31}$$

where Δ_x, Δ_y and Δ_z denote the grid width in the corresponding spatial direction.

3.3 Very large eddy simulation

In this study the very large eddy simulation (VLES) approach is investigated. The general name flow simulation methodology is used in some papers for this model. This model belongs to hybrid eddy-resolving or RANS-based sub-scale methods and are based on a very similar equation as in the RANS approach. Although a coincidence they realize the main concept of the LES approach, where the scale and consequently physical properties are filtered by an appropriate filter function. This idea is feasible due to the similarity of the LES and the RANS equations (see Sections 3.1 and 3.2). The VLES model was first mentioned by Speziale [152] and he outlined three basic properties which a hybrid turbulence method should posses [151]:

- the turbulence model transforms into the RANS model on the coarse grid region
- DNS should be recovered on the fine mesh region
- the application of explicit filtering (see Section 3.2) or averaging is not desirable.

The approach of Speziale is neither classical RANS nor LES. However, the idea of this method is very similar to the LES concept: the large scales in the VLES model are simulated, while the small ones are modeled. The VLES approach provides a transition from the fully modeled RANS to the fully resolved DNS modes depending on the numerical grid resolution. The main difference to the traditional LES is the replacement of the sub-grid scale stress $\widetilde{\tau_{ij}}$ through the Reynolds stress of a generalized RANS model τ_{ij}^{turb} rescaled with a resolution control function F_r:

$$\widetilde{\tau_{ij}} = F_r \tau_{ij}^{turb}. \tag{3.32}$$

In the original VLES model the F_r function depends on two length scales: the turbulent length scale l_c related to the spectral cut-off and the Kolmogorov length scale η. The first formulation of the VLES model has a weakness in the near wall region, since the resolution control function damps the Reynolds stress too strongly. Therefore, some modifications of the resolution control function are proposed. For example, Zhang et al. [176], Han and Krajnović [60] improve the definition of F_r with the introduction of a third length scale: the integral length scale l_0 ($\propto k_{us}^{3/2}/\varepsilon_{us}$). The modified method recovers the RANS in the near wall region and the LES approach can be reached between the RANS and the DNS limits. The new very large eddy simulation method is validated with different turbulent flow configurations and show the efficiency in the resolving of the large flow structures together with the high efficiency and robustness in many applications already on relatively coarse grids [58], [59].

In 2014, Chang et al. [24] suggested the modification of the VLES model and defined the F_r function based on the following concept:

$$F_r \propto \int_{\kappa_C(LES)}^{\kappa_K} E(\kappa)d\kappa \Big/ \int_{\kappa_C(VLES)}^{\kappa_K} E(\kappa)d\kappa. \tag{3.33}$$

where C denotes the "cut-off "and K - the Kolmogorov scales; the area between κ_C and κ_K is related to the unresolved scale (see Figure 3.3).

Corresponding to this concept the resolution control function has the following form:

$$F_r = \min\left[1, \left(\frac{l_c}{l_0}\right)^{\frac{3}{4}}\right] . \tag{3.34}$$

The modified F_r function depends only on the integral length scale $l_0 = k^{3/2}/\varepsilon$ and the turbulent length scale related to the spectral cut-off $l_c = C_x\Delta$. In Chang et al. [24], a detailed derivation of the resolution control function F_r can be found.

According to this definition, F_r takes a value between one and zero. When the resolution control function approaches zero, all of the scales are (theoretically) resolved and the VLES model behaves similar to a DNS. In regions, where $F_r \to 1$, as in the case of a coarser mesh, the higher fraction of the modeled turbulence is expected and the method works as a RANS model, similar to the DES concept. Between these two modes, the VLES behaves like a LES. The filter width applied in this hybrid eddy-resolving model is in order larger compared to the LES filters, which is defined by the grid size (see Figure 3.3). Consequently, the dependency of numerical results

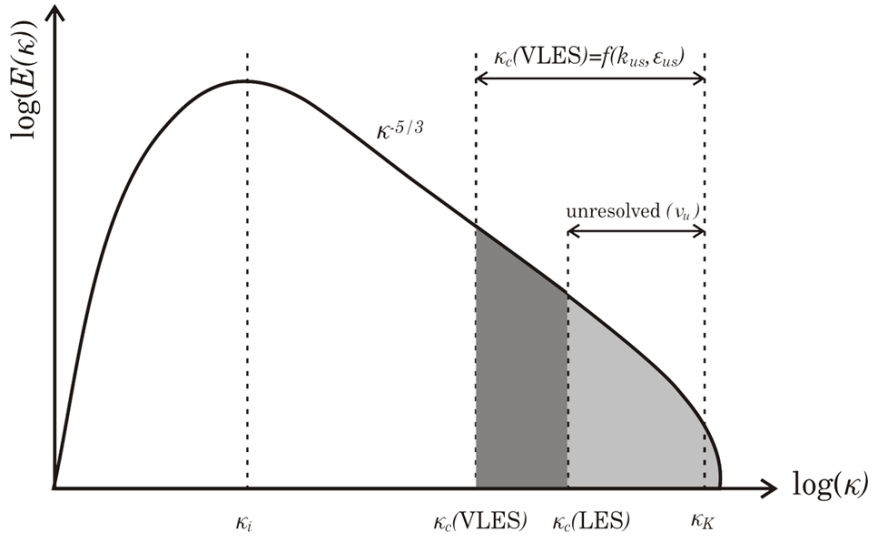

Figure 3.3: Schematic view of energy spectrum with characteristic cut-offs corresponding to unresolved $\kappa_C(\mathrm{LES})$ and unsteady $\kappa_C(\mathrm{VLES})$ scales [24].

on the grid resolution is not explicit. Therefore, the new VLES model fulfills the requirements of Speziale.

The VLES method is well compatible with different RANS turbulence models. In this study, a VLES approach based on three different RANS models is used: the VLES model based on the Chien $k-\varepsilon$ model (Section 3.1.2), on the Wilcox $k-\omega$ model (Section 3.1.3) and on the elliptic-relaxation eddy-viscosity $\zeta-f$ VLES model (Section 3.1.4).
The transport equations for the Chien $k-\varepsilon$ VLES model are defined as follows:

$$\rho\frac{\partial k_{us}}{\partial t}+\rho\widetilde{u_j}\frac{\partial}{\partial x_j}k_{us}=\frac{\partial}{\partial x_j}\left[\left(\mu+\frac{\mu_t}{\sigma_k}\right)\frac{\partial k_{us}}{\partial x_j}\right]+P_{k_{us}}-\rho\varepsilon_{us}-2\nu\frac{k_{us}}{y^2}\,, \tag{3.35}$$

$$\rho\frac{\partial \varepsilon_{us}}{\partial t}+\rho\widetilde{u_j}\frac{\partial}{\partial x_j}\varepsilon_{us}=\frac{\partial}{\partial x_j}\left[\left(\mu+\frac{\mu_t}{\sigma_{\varepsilon_{us}}}\right)\frac{\partial \varepsilon_{us}}{\partial x_j}\right]+C_{\varepsilon 1}P_{k_{us}}\frac{\varepsilon_{us}}{k_{us}}-\rho\varepsilon_{us}\left(\frac{C_{\varepsilon 2}f_\varepsilon}{k_{us}}-\frac{2\nu}{y^2}e^{-0.5\,y^+}\right) \tag{3.36}$$

with the index us characterizing the "unsteady" RANS regime and the production term $P_{k_{us}}$

$$P_{k_{us}}=2\nu_u\left|\widetilde{S_{ij}}\right|\left|\widetilde{S_{ij}}\right|.$$

Due to the similarity of the equations for the $k-\epsilon$ and $k-\omega$ RANS models, the equations for the last one are not presented here for the VLES formulation.

Since the predictive accuracy of VLES depends on the specific RANS turbulence model [58], the application of the $\zeta-f$ model as a background RANS model for VLES appears to be promising. The reason is, that this model demonstrates advantages in a prediction of anisotropy effects in the wall near region in comparison to two other investigated models.

For the $\zeta - f$ VLES model the transport equations have the following form:

$$\frac{\partial k_{us}}{\partial t} + \widetilde{u_j}\frac{\partial k_{us}}{\partial x_j} = P_{k_{us}} - \varepsilon_{us} + \frac{\partial}{\partial x_j}\left[\left(\nu + \frac{\nu_u}{\sigma_k}\right)\frac{\partial k_{us}}{\partial x_j}\right], \tag{3.37}$$

$$\frac{\partial \varepsilon_{us}}{\partial t} + \widetilde{u_j}\frac{\partial \varepsilon_{us}}{\partial x_j} = \frac{C_{\varepsilon_1}P_{k_{us}} - C_{\varepsilon_2}\varepsilon_{us}}{\tau_\zeta} + \frac{\partial}{\partial x_j}\left[\left(\nu + \frac{\nu_u}{\sigma_\varepsilon}\right)\frac{\partial \varepsilon_{us}}{\partial x_j}\right], \tag{3.38}$$

$$\frac{\partial \zeta_{us}}{\partial t} + \widetilde{u_j}\frac{\partial \zeta_{us}}{\partial x_j} = f - \frac{P_{k_{us}}}{k}\zeta_{us} + \frac{\partial}{\partial x_j}\left[\left(\nu + \frac{\nu_u}{\sigma_\zeta}\right)\frac{\partial \zeta_{us}}{\partial x_j}\right], \tag{3.39}$$

$$L_\zeta^2 \Delta f_{us} - f_{us} = \frac{1}{\tau_\zeta}\left(C_1 + C_2\frac{P_{k_{us}}}{\varepsilon_{us}}\left(\zeta_{us} - \frac{2}{3}\right)\right), \tag{3.40}$$

with the turbulent length and time scales

$$\tau_{\zeta,\,us} = \max\left[\frac{k_{us}}{\varepsilon_{us}}, C_\tau\left(\frac{\nu}{\varepsilon_{us}}\right)^{1/2}\right], \tag{3.41}$$

$$L_{\zeta,\,us} = \max\left[\frac{k_{us}^{3/2}}{\varepsilon_{us}}, C_\eta\left(\frac{\nu^3}{\varepsilon_{us}}\right)^{1/4}\right]. \tag{3.42}$$

Compared to basic RANS models, in the VLES approach, the formulation of the turbulent viscosity is modified. For the $\zeta - f$ model, the sub-grid scale (unresolved) turbulent viscosity takes the form:

$$\nu_u = F_r C_\mu^\zeta \zeta_{us} k_{us} \tau_{\zeta,\,us}, \tag{3.43}$$

and for the $k - \varepsilon$ VLES model, the turbulent viscosity is defined as the following:

$$\nu_u = F_r C^\mu f_\mu \frac{k_{us}^2}{\varepsilon_{us}}, \tag{3.44}$$

The validation of the VLES model on the static and moving grid can be found in the following chapters.

4 Numerical Methods

In order to simulate turbulent flows, the Navier-Stokes equations described in Chapter 3 are solved using numerical techniques. There are various kinds of approximation methods to solve this system of partial differential equations by means of numerical methods, such as the finite difference (FD), the finite element (FE) and the finite volume (FV) methods. For fluid dynamic problems, it is advantageous to use the finite volume method (FVM), because with this numerical technique, discretized equations fulfill the conservation principles also in their discrete forms. The fundamental principle of the method is the subdivision of the problem area in a finite number of control volumes. Subsequently, the conservation equations are evaluated in the center of the control volumes and an approximation system of the algebraic differential equations is created. After solving this system of equations, a solution of the flow problem is available. A detailed description of the FVM can be found in the textbook of Schäfer [138].

This chapter gives a short overview of the numerical methods applied in this work. Firstly, the general idea of FVM is presented. In Sections 4.2 and 4.3, employed spatial and time discretization methods are introduced. Following that the concept of the pressure correction method is outlined. Finally, a short description of the in-house code FASTEST, together with the multigrid method and a technique for the grid deformation which is realized in FASTEST, are briefly presented.

4.1 General strategy of finite volume method

In the following section, the concept of the FVM is presented on the basis of a general transport equation for an optional unknown ϕ:

$$\underbrace{\rho \frac{\partial \phi}{\partial t}}_{time\ term} + \underbrace{\rho \frac{\partial \left(u_i \phi\right)}{\partial x_i}}_{convective\ term} - \underbrace{\frac{\partial}{\partial x_i}\left(\Gamma_\phi \frac{\partial \phi}{\partial x_i}\right)}_{diffusive\ term} = \underbrace{q_\phi}_{source\ term} , \tag{4.1}$$

with Γ_ϕ being a diffusion coefficient for the quantity ϕ.

The starting point of the FVM is the subdivision of the problem area by means of a numerical grid in a finite number of control volumes (CVs). Subsequently, for each CV, the transport equation in integral form is formulated. After applying the Gauss' integral theorem, the equation (4.1) takes the following form:

$$\int_V \underbrace{\rho \frac{\partial \phi}{\partial t}}_{time\ term} dV + \sum_c \int_{S_c} \underbrace{\rho \left(u_i \phi\right)}_{convective\ flux} dS - \sum_c \int_{S_c} \underbrace{\left(\Gamma_\phi \frac{\partial \phi}{\partial x_i}\right) n_i}_{diffusive\ flux} dS = \int_V \underbrace{q_\phi}_{source\,term} dV \ . \tag{4.2}$$

with the faces of the control volumes S_c.

For the numerical solution of equation (4.2), an approximation of the volume and surface integrals is required. For this, the second order midpoint rule is used. For example, for the east side S_e, it leads to the following approximation of the convective and diffusive fluxes:

$$\rho \int_{S_e} (u_i \phi)\, dS \approx \rho\, (u_i \phi)_e\, n_e \partial S_e = \dot{m}_e\, \phi_e\ , \tag{4.3}$$

$$\int_{S_c} \left(\Gamma_\phi \frac{\partial \phi}{\partial x_i} \right) n_i\, dS \approx \left(\Gamma_\phi \frac{\partial \phi}{\partial x_i} n_i \right)_e \partial S_e\ . \tag{4.4}$$

where $\dot{m}_e$ is a mass flux through the east face S_e and the ∂S_e is the surface area. After applying the three-dimensional midpoint rule on the volume integral, the source term takes the following form:

$$\int_V q_\phi dV \approx (q_\phi)_P\, \partial V\ , \tag{4.5}$$

with index p denoting the value in the center of the CV and ∂V being the volume of the current CV.

The approximation of the diffusive and convective terms with the midpoint rule requires the values on the control volume sites. As these values are not known, further linear interpolation from the values on the center of the CV must be used.

4.2 Spatial discretization

Each of the terms in equation (4.2) requires specific discretization methods. For the diffusive and convective terms, the spatial discretization techniques described in this section are applied. Generally, for an approximation of the diffusive flux, a second order *central differencing scheme (CDS)* is used, while for the convective flux, the first order *upwind differencing scheme (UDS)* as well as CDS can be applied. These two commonly used techniques as well as the *flux-blending* approximation and the *high-resolution* (HR) methods are outlined in this section.

To simplify the description of the discretization methods, the problem is reduced to two dimensions. Furthermore, for demonstration of the spatial discretization principles, a control volume (index P) with four neighboring CVs (W-west, E-east, N-north, S-south) for a Cartesian grid is defined (see Figure 4.1).

4.2.1 Upwind differencing scheme

The concept of the upwind differencing scheme (UDS) is based on the idea, that in convection-dominated flows, the flow quantities on control volume sites are more influenced by the upstream

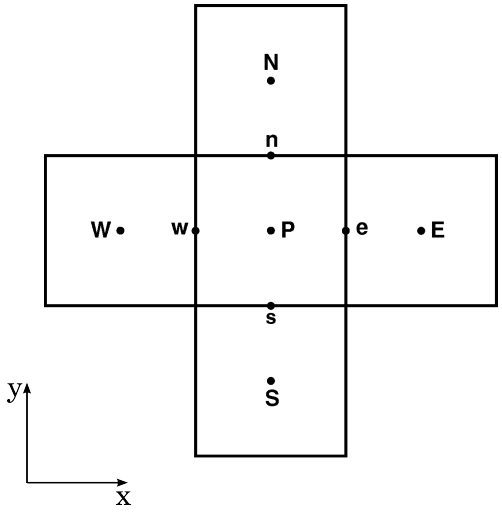

Figure 4.1: Control volume with its neighbor nodes for two-dimensional case.

than by the downstream cell center. Therefore, the first order UDS is formulated as:

$$\phi_e = \phi_P, \quad \text{for } \dot{m}_e \geq 0 \ , \tag{4.6}$$

$$\phi_e = \phi_E, \quad \text{for } \dot{m}_e \leq 0 \ . \tag{4.7}$$

This scheme is unconditionally bounded and robust; however, due to the low order, this discretization method has a high level of numerical diffusion. Therefore, the scheme requires a very fine grid to yield satisfactory results.

4.2.2 Central differencing scheme

Another possibility to approximate $\phi(x,t)$ in the neighboring control volumes is the central differencing scheme (CDS). In this method the flow quantities on control volume sites are defined over the interpolation between the centers of the neighboring cells:

$$\phi_e \approx \phi_E \gamma_e + \phi_P (1 - \gamma_e) \ , \tag{4.8}$$

where γ_e is the linear interpolation factor:

$$\gamma_e = (x_e - x_P)/(x_E - x_P). \tag{4.9}$$

The CDS method has a second order accuracy on Cartesian grids. However, in contrast to the UDS, in this method non-physical oscillations can appear in the solution in regions of strong convection. This happens if the boundedness of the method is no longer ensured. In this case, the Péclet number, characterizing the local relation of convective to diffusive transport, is larger than two:

$$Pe = \frac{\rho \, u \Delta x}{\Gamma} > 2. \tag{4.10}$$

For the LES simulation, the central differencing scheme (CDS) is commonly used due to the required negligible numerical dissipation and very fine grid resolution. However, in the RANS models, difficulties arise by using the CDS method at high Reynolds numbers due to the coarse mesh resolution, which leads to the high Pe.

4.2.3 Flux-blending

The flux-blending approximation combines the advantages of methods with low order (UDS), such as robustness and boundedness, with the exacter approximation of methods with higher order accuracy (CDS). Both schemes are weighted by the factor β, which takes a value between 0 and 1:

$$\phi_e = \beta\phi_{e,CDS} + (1-\beta)\phi_{e,UDS} \ , \tag{4.11}$$

This approximation yields very good results for moderate Péclet numbers.

4.2.4 High-resolution schemes

The schemes described in the sections above have severe weaknesses, such as the poor accuracy due to the numerical diffusion and instability. This shortcoming can be solved by using higher order schemes, including a quadratic upstream interpolation for convective kinematics (QUICK) by Leonard [92] or the upwind-scheme third order. However, despite the significant improvement, the problems with the boundedness and accuracy are not solved completely. High-resolution (HR) schemes provide reliable techniques to suppress the formation of the undesirable oscillations.

There are two numerical tools that transform the linear unbounded high-order scheme into a bounded non-linear high-resolution scheme. The first technique for developing HR-schemes is *total variation diminishing* (TVD) approach, introduced by Harten [65]. As the name indicates, this method uses the idea of a total variation (TV). In systems described by partial differential equations, TV is defined on the node i as:

$$TV = \sum_i \mid \phi_{i+1} - \phi_i \mid \ . \tag{4.12}$$

The following condition ensures that the solution does not increase with time:

$$TV\left(\phi^{n+1}\right) \leq TV\left(\phi^n\right) \ . \tag{4.13}$$

To construct a HR scheme in the TVD approach a so-called flux limiter function should be proposed. For example, according to Sweby [156], the TVD can be transferred on the higher order schemes by means of the introduction of the following limiting function $\Phi(r)$:

$$\phi_f = \phi_C + \frac{1}{2}\Phi(r)\ (\phi_D - \phi_C) \ , \quad r = \frac{\phi_C - \phi_U}{\phi_C - \phi_D} \ . \tag{4.14}$$

with indexes C - center, D - downwind, U - upwind and F - face.

The condition (4.13) is fulfilled, if the following criterion for the limiting function is valid:

$$\Phi(r) = \begin{cases} min(2r\,, 2) & r > 0 \\ 0 & r \leq 0 \end{cases} \tag{4.15}$$

The full mathematical derivation of this methodology can be found in [156].

An additional framework for the description and analyses of HR schemes is the *normalized variable formulation (NVF)* introduced by Leonard [93]. This approach ensures the boundedness if the *convection boundedness criterion (CBC)* [51] is fulfilled. According to the NVF, the normalized variable is defined as:

$$\tilde{\phi} = \frac{\phi - \phi_U}{\phi_D - \phi_U}\,. \tag{4.16}$$

Based on this equation, the value of $\phi_f = f(\phi_U, \phi_C, \phi_D)$ is transformed to $\tilde{\phi_f} = f\left(\tilde{\phi_C}\right)$, because the normalized values are $\tilde{\phi_U} = 0$ and $\tilde{\phi_D} = 1$. The CBC is then formulated as:

$$\tilde{\phi_C} < \tilde{\phi_f} < 1, \text{if } 0 < \tilde{\phi_C} < 1\,, \tag{4.17}$$

$$\tilde{\phi_f} = \tilde{\phi_C}, \qquad \text{otherwise}\,. \tag{4.18}$$

Various high resolution schemes have been developed based on this concept, such as Gamma [75], AVLSMART [123] or the convergent and universally bounded interpolation scheme for the treatment of advection (CUBISTA) [4]. All of these schemes were implemented in the in-house code FASTEST by Reimann [124] in the formulation of Ng et al. [114]. For the numerical and implementation details, these two sources are included for reference.

An additional HR-scheme implemented in FASTEST is the technique of Xue [174], which belongs to TVD schemes and is based on the MUSCL-scheme [95]. The starting point of this scheme is the definition of ϕ_f by means of the TVD approach:

$$\phi_f = \phi_U + \frac{1}{2}\phi(r)^{HO}\,(\phi_D - \phi_C)\,, \quad \phi(r)^{HO} = \frac{1+\kappa}{2} + \frac{1-\kappa}{2}r\,, \tag{4.19}$$

where $-1 \leq \kappa \leq 1$. The function $\phi(r)^{HO}$ is completed by the following boundaries:

$$\phi(r)^{HO}(r) = max\left[0, min\left(2r, \frac{1+\kappa}{2} + \frac{1-\kappa}{2}r, 2\right)\right]\,. \tag{4.20}$$

Following the normalization the Xue-MUSCL scheme is presented in the following form:

$$\tilde{\phi}_f^X = \begin{cases} 2\tilde{\phi}_C & , \quad 0 < \tilde{\phi}_C < \frac{1+\kappa}{4+2\kappa}\,, \\ \left(1 - \frac{\kappa}{2}\tilde{\phi}_C + \frac{1+\kappa}{4}\right) & , \quad \frac{1+\kappa}{4+2\kappa} < \tilde{\phi}_C < \frac{3-\kappa}{4-2\kappa}\,, \\ 1 & , \quad \frac{3-\kappa}{4-2\kappa} < \tilde{\phi}_C < 1\,, \\ \tilde{\phi}_C & , \quad \text{otherwise}\,. \end{cases} \tag{4.21}$$

4.3 Time discretization

As the turbulent flows investigated in the present work are unsteady, a temporal discretization is required in addition to a spatial discretization. After applying the spatial discretization techniques described in the prior section, the problem (4.1) results in a system of ordinary differential equations. These approximated equations can be transformed in the form, where all terms of the spatial discretization remain on the right side and are summarized with the operator $\mathfrak{L}(\phi)$:

$$\frac{\partial \phi}{\partial t} = \mathfrak{L}(\phi) \ . \tag{4.22}$$

The discretization is performed by subdividing the entire time interval $[t_0, t']$ into separate intervals Δt_n:

$$t_{n+1} = t_n + \Delta t \ . \tag{4.23}$$

Two different types of time discretization are distinguished: implicit and explicit.

4.3.1 Explicit methods

In the explicit methods, the solution in the time step $n+1$ is calculated with already known quantities from the previous time step:

$$\phi^{n+1} = \mathfrak{F}(\phi^n, \phi^{n-1}, \ldots) \ . \tag{4.24}$$

Here and in the following, the simplified term $\phi(t_n) = \phi^n$ is used.

This method is easy to apply and implement, but due to stability reasons, the maximal time step length is strongly limited by the Courant–Friedrichs–Lewy (CFL) condition: $CFL = u\Delta t/\Delta x \leq CFL_{max}$, where C_{max} is a constant dependent on the discretization method.

4.3.2 Implicit methods

Contrary to the explicit techniques, the implicit methods include values calculated in the current time step in their formulation [138]:

$$\phi^{n+1} = \mathfrak{F}(\phi^{n+1}, \phi^n, \phi^{n-1}, \ldots) \ . \tag{4.25}$$

By using implicit methods, additional memory space and longer computational times are required, since an additional system of equation must be solved in each time step. Nevertheless, because of their flexible time step choice, which is determined by physics and not by numerics, the implicit methods are commonly used.

Within this work the *second order fully implicit method* (SOFI), which is also known as the three-point-backward-method or backward differentiation formula (BDF), is applied:

$$\left.\frac{\partial \phi_p}{\partial t}\right|_{n+1} \approx \frac{3\phi_P^{n+1} - 4\phi_P^n + \phi_P^{n-1}}{2\Delta t_n} = \mathfrak{L}\left(\phi_P^{n+1}\right) \ . \tag{4.26}$$

4.4 Solving resulting system

After accomplishing the spatial and time discretization presented above, the discretized transport equation can be written in the coefficient form:

$$a_p \phi_p - \sum_c a_c \phi_c = b_P \ . \tag{4.27}$$

with the index of adjacent cell centers c. This equation is valid for every control volume. Subsequent to the assembling, a system of linear equations for all of the control volumes appears. This system can be written in the matrix form:

$$A_{ij} \phi_i = b_j \ . \tag{4.28}$$

In order to solve this linear system, one of the direct or iterative methods can be applied [138]. In the present work, the *strongly implicit procedure (SIP)* [155] belonging to iterative methods is used to solve the sparse linear system of equations. This is an iterative method based on an incomplete LU decomposition and has been specially developed for the system of algebraic equation, which arises from the discretization of partial differential equations. The main idea of the SIP method is the modification of the system matrix $\boldsymbol{A}$ to improve the resulting upper and lower matrices and, therefore, the efficiency of the solution method. The SIP method, as other iterative methods, performs well for the high frequency errors. Therefore, this technique is often applied as a smoother in a multigrid method, which is briefly presented in the following section.

4.5 Pressure correction method

As mentioned in Chapter 2, the Navier-Stokes equations (2.4) and (2.9) represent a coupled equations system. Due to the incompressibility assumption, the calculation of the pressure is a major difficulty in the numerical solution of these equations; because the pressure is linked to the velocities only in the momentum equations (2.9). There are different methods for the coupling of the pressure and the velocities. The technique used in this work is the *semi-implicit method for pressure linked equations (SIMPLE)* algorithm.

Initially, within the pressure correction method, the velocity components are calculated with an estimated (or well-known) pressure field on the basis of the momentum equations (2.9). Then, the calculated velocity field is inserted into the continuity equation (2.4). However, these velocities do not fulfill the equation of mass conservation. Therefore, a mass source arises through the incorrect pressure field. A suitable pressure can be calculated by means of the transformation of the equations. For the balance of this mass difference, a velocity correction is calculated and performed in the subsequent correction step. In the case of convergence, the next time step is calculated. Otherwise the next iteration within the pressure correction is performed. Detailed information can be found in Schäfer [138].

4.6 FASTEST

In the present work the in-house code of the Department of Numerical Methods in Mechanical Engineering at the TU Darmstadt **FASTEST** (flow analysis by solving of transport equations simulating turbulence) is used. FASTEST is a boundary-fitter, block-structured incompressible flow solver based on a finite volume discretization with the pressure velocity coupling.

To solve the system of linear equations arising from the discretization of differential equations, the SIP algorithm together with the pressure-correction method SIMPLE is realized in FASTEST. The iterative solvers, such as SIP, produce smooth errors, which are reduced very slowly. This problem can be solved by applying the *multigrid method*, which is available in FASTEST. The purpose of this method is to define a coarser grid on which a low frequency error will be seen as a high frequency and thus will be reduced more quickly. More details on the multigrid method can be found in the textbook of McCormick [101]. The multigrid technique provides an effective method for various kinds of flows; however, Alkishriwi et al. [3] demonstrated that the benefit of a multigrid method is reduced for highly convective, time dependent problems, such as turbulent flows.

In the block-structured code FASTEST, a grid deformation technique is realized within three steps for the calculation of FSI problems or cases with moving structures. First, the edges of each block are calculated using a linear interpolation or cubic spline approximation. In the second step, the faces of the blocks are moved accordingly by linear interpolation, a transfinite interpolation (TFI) [56] or an elliptic method. Finally, the inner grid points of the blocks are modified using one of the prior methods. This process is repeated for every block until the entire grid is updated. The linear interpolation is the simplest technique, which is applied for the deformation of edges or faces. As the name indicates, the grid points are modified by means of the linear interpolation. In the TFI technique, which belongs to the algebraic approaches, the distribution of the inside grid points is calculated by means of the bi-linear interpolation of the grid points on the boundary. In the elliptic grid movement the grid points are distributed by solving the elliptic equation (Poisson equation). For details on the implementation of different techniques please refer to [120].

For the simulation of fluid-structure coupling problems, the total FSI problem is divided into a fluid and a structural part, which are solved separately in the fluid solver FASTEST, and into a structure solver (partitioned approach). The coupling between the two sets of equations is realized by the exchange of the values at the common boundary interface.

5 Verification of RANS Models

For this research the very large eddy simulation (more details in Section 3.3) is implemented in the in-house code FASTEST (Section 4.6). As the RANS equations are applied in the formulation of the VLES approach, the verification of the basic statistical turbulence models is required to ensure the correct performance of the VLES model. The goal of a verification procedure is the examination of the correct implementation of equations and boundary conditions within software. As the verification is a pure mathematical procedure, it is unnecessary for the results of the verification to be physically correct.

This chapter begins with the description of the *method of the manufactured solution* (MMS), which is applied in this research for the verification of the implemented RANS models. Following that, the concept of verification of turbulence models is introduced. Then, the configuration of the verification test case and the manufactured solution for the turbulent quantities are presented. Finally, the results of the verification are summarized at the end of this chapter.

5.1 Method of manufactured solution

The method of the manufactured solution is a commonly used technique for the verification of source codes and simulation software. The starting point of this method is a design of a solution ϕ_{ms}, which does not have to possess a physical background. However, the solution should fulfill some conditions, for example, the solution should have a sufficient number of non-trivial derivatives. Subsequently, this constructed solution is inserted into the governing equations, which in this work are the Navier-Stokes equations and transport equations for the turbulent quantities. Due to the free choice of the manufactured solution ϕ_{ms}, the system of differential equations is no longer in balance and therefore the source term Q should be analytically calculated:

$$D\ \phi_{ms} = Q\ , \tag{5.1}$$

where D is a differential operator. In the next step, the system of equations (5.1) is solved on computational grids with different grid resolutions. The boundary conditions are defined by means of the constructed solution. Afterwards, the discrete solution of the source code ϕ_h is compared with the designed solution ϕ_{ms} and the approximation error e_h is calculated:

$$e_h = \phi_h - \phi_{ms}\ . \tag{5.2}$$

The error of the numerical solution is estimated by means of the *root mean square*:

$$\text{RMS}\,(e_h) = \sqrt{\sum_{i=2}^{NX-1}\sum_{j=2}^{NY-1}\frac{\left(\phi(i,j)-\phi_{MS}(i,j)\right)^2}{(NX-2)(NY-2)}}\ , \tag{5.3}$$

with i and j being the indices in the x- and y-direction, accordingly, and NX and NY being the number of the grid points in x-and y-directions.

The last step of the verification is the calculation of the order of accuracy of a certain algorithm p_c

$$p_c = \frac{\log\left(\frac{e_{2h}}{e_h}\right)}{\log\left(\frac{2h}{h}\right)} \,. \tag{5.4}$$

and a comparison of p_c with the formal order of accuracy p_0. If the observed and formal order of accuracy do not coincide, then an implementation error may exist in the program code; otherwise the implementation is correct. A detailed description of MMS technique can be found in [137] and [133].

5.2 Verification of RANS models

The verification of RANS models is based on the technique proposed by Eça et al. [42], [40], [41]. It has been developed especially for two-dimensional, steady, wall-bounded, incompressible turbulence flows. As mentioned above, the manufactured solution does not need to have a physical meaning. However, the construction of a physically realistic solution has several advantages, such as smaller source terms as well as similar difficulties to a real problem in the solution and error estimate process [41]. Based on this idea, the manufactured solutions are constructed, which prescribe velocities components, pressure and, for the two-equation RANS model, the eddy viscosity ν_t and the turbulent kinetic energy k. Other turbulent quantities, for example, dissipation ε and ω, can be derived from designed ν_t and k.

The computational domain taken from [42] is a two-dimensional square with a side length $0.5\,L$, where the bottom left corner is $(0.5, 0)$. The Reynolds number Re is based on the reference length L and the reference velocity U_1: $Re = U_1\,L/\nu = 10^6$. The calculations are performed on three grids of different refinement: 101×101, 201×201 and 401×401. All meshes have a refinement on the bottom wall (see Figure 5.1).

The manufactured solutions for the main flow variables (u-, v-velocities as well as pressure p) are identical for both turbulence models verified in this work. The velocity components in the x- and y-direction are defined as follows:

$$u = \text{erf}\left(\frac{4y}{x}\right), \qquad v = \frac{1}{4\sqrt{\pi}}\left(1 - \text{e}^{-\frac{16y^2}{x^2}}\right) \,. \tag{5.5}$$

The mass conservation equation is satisfied identically with the velocity components designed in this way.

The pressure coefficient is given by:

$$C_p = \frac{p}{\rho U_1^2} = 0.5 \ln\left(-x^2 + 2x + 0.25\right)\, \ln\left(4y^3 - 3y + 1.25\right) \,. \tag{5.6}$$

Boundary conditions for all quantities are calculated by inserting the according coordinates in

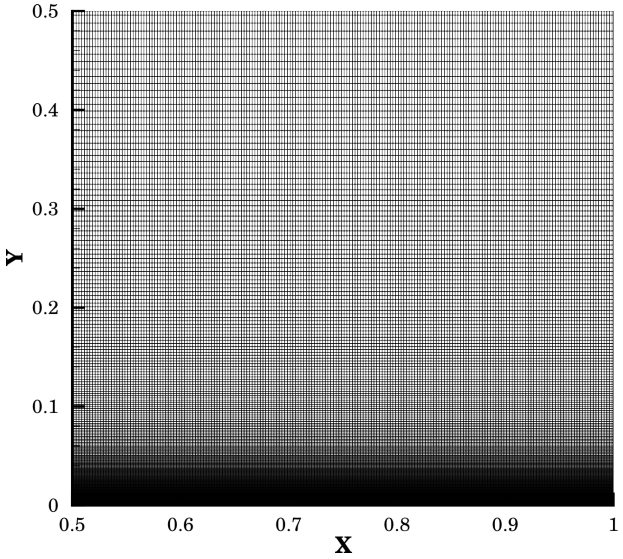

Figure 5.1: Computational domain with mesh 101×101 for verification of RANS models.

the manufactured solutions:

$$u|_{bound} = (u)|_{ms},\ v|_{bound} = (v)|_{ms}\ . \tag{5.7}$$

Source terms can be detected by inserting of the designed solutions (5.5), (5.6) in the Navier-Stokes equations (3.4) and (3.5):

$$\begin{aligned} Q_x &= u\frac{\partial u}{\partial x} + v\frac{\partial u}{\partial y} - (\mu_t + \mu)\left(\frac{\partial^2 u}{\partial x^2} + \frac{\partial^2 u}{\partial y^2}\right) - 2\frac{\partial \mu_t}{\partial x}\frac{\partial u}{\partial x} - \frac{\partial \mu_t}{\partial y}\left(\frac{\partial u}{\partial y} + \frac{\partial v}{\partial x}\right) + \frac{\partial C_p}{\partial x}\ , \\ Q_y &= u\frac{\partial v}{\partial x} + v\frac{\partial v}{\partial y} - (\mu_t + \mu)\left(\frac{\partial^2 v}{\partial x^2} + \frac{\partial^2 v}{\partial y^2}\right) - 2\frac{\partial \mu_t}{\partial y}\frac{\partial v}{\partial y} - \frac{\partial \mu_t}{\partial x}\left(\frac{\partial u}{\partial y} + \frac{\partial v}{\partial x}\right) + \frac{\partial C_p}{\partial y}\ . \end{aligned} \tag{5.8}$$

As the $k - \omega$ RANS model was verified in the work of Türk [163], only the verification of the $k - \varepsilon$ and $\zeta - f$ models is done in this study.

5.2.1 Verification of the Chien $k - \varepsilon$ RANS model

The first model, which is validated in this study, is the Chien $k - \varepsilon$ model. In this low Reynolds model, two additional equations occur in the calculation of the eddy viscosity: the transport equation for the turbulent kinetic energy k and the transport equation for the dissipation ε. The idea of Eça et al. [40] is to construct manufactured solutions only for the turbulent kinetic energy and the turbulent viscosity and to deduce the solution for the other turbulent quantities from these two designed solutions.

Constructed solutions for the turbulent kinetic energy and the turbulent viscosity for the Chien $k - \varepsilon$ model with $\nu_{max} = 10^3\nu$ and $k_{max} = 0.01$ have the following form:

$$k = k_{max}\,\eta_\nu^2\,\mathrm{e}^{1-\eta_\nu^2}\ , \quad \nu_t = 0.25\,\nu_{max}\,\eta_\nu^4\,\mathrm{e}^{2-\eta_\nu^2}\ , \tag{5.9}$$

where the *non-dimensional similar variable* η_ν is defined as:

$$\eta_\nu = \frac{10\,y}{x}\ . \tag{5.10}$$

Both designed solutions fulfill the expectation of the behavior of the turbulent flow in the near wall region. The turbulent viscosity ν_t varies with y^4 close to the bottom wall and k proportional to y^2. Moreover, the maximum turbulent kinetic energy k_{max} occurs closer to the bottom wall than the maximum ν_t.

The dissipation rate follows from the manufactured ν_t and k:

$$\tilde{\varepsilon} = \varepsilon f_\mu = 0.36\,\frac{k_{max}^2}{\nu_{max}}\,f_\mu\,\mathrm{e}^{-\eta_\nu^2}\ . \tag{5.11}$$

The damping functions f_μ and f_ε required for the Chien $k-\varepsilon$ model are constructed with consideration of their properties:

$$f_\mu = 1 - e^{-0.0115\,y^+}\ , \quad f_\varepsilon = 1 - \frac{0.4}{1.8}e^{-\left(\frac{k^2}{6\nu\varepsilon}\right)^2}\ , \tag{5.12}$$

with the non-dimensional wall distance

$$y^+ = y\sqrt{\frac{8}{x\nu\sqrt{\pi}}}\ . \tag{5.13}$$

The solutions (5.9) and (5.11), which are designed for the low Reynolds $k-\varepsilon$ model, are inserted into the transport equations for the turbulent kinetic energy and the dissipation of the turbulent kinetic energy (3.7). The following source terms are obtained with the coefficients summarized in table 3.1:

$$\begin{aligned}
Q_k &= u\frac{\partial k}{\partial x} + v\frac{\partial k}{\partial y} - \left(\frac{\mu_t}{\sigma_k}+\mu\right)\left(\frac{\partial^2 k}{\partial x^2}+\frac{\partial^2 k}{\partial y^2}\right) - \frac{1}{\sigma_k}\left(\frac{\partial \mu_t}{\partial x}\frac{\partial k}{\partial x}+\frac{\partial \mu_t}{\partial y}\frac{\partial k}{\partial y}\right)\\
&\quad - P_k + \rho\varepsilon + 2\nu\frac{k}{y^2}\ ,\\
Q_{\tilde{\varepsilon}} &= u\frac{\partial \tilde{\varepsilon}}{\partial x} + v\frac{\partial \tilde{\varepsilon}}{\partial y} - \left(\frac{\mu_t}{\sigma_\varepsilon}+\mu\right)\left(\frac{\partial^2 \tilde{\varepsilon}}{\partial x^2}+\frac{\partial^2 \tilde{\varepsilon}}{\partial y^2}\right) - \frac{1}{\sigma_\varepsilon}\left(\frac{\partial \mu_t}{\partial x}\frac{\partial \tilde{\varepsilon}}{\partial x}+\frac{\partial \mu_t}{\partial y}\frac{\partial \tilde{\varepsilon}}{\partial y}\right)\\
&\quad - C_{\varepsilon_1}P_k\frac{\tilde{\varepsilon}}{k} + \tilde{\varepsilon}\rho\left(\frac{C_{\varepsilon_2}f_{\tilde{\varepsilon}}}{k}+\frac{2\nu}{y^2}e^{-0.5\,y^+}\right)\ .
\end{aligned} \tag{5.14}$$

Source terms (5.14) are added to the transport equations for k and ε in the source code accordingly. Then, the test described in the beginning of the present section is calculated on three grids of systematical refinement. Subsequently, the error between the manufactured solution and the solution obtained from the calculation is estimated with equation (5.3). The order of accuracy together with the RMS error on the two finer meshes is presented in Table 5.1.

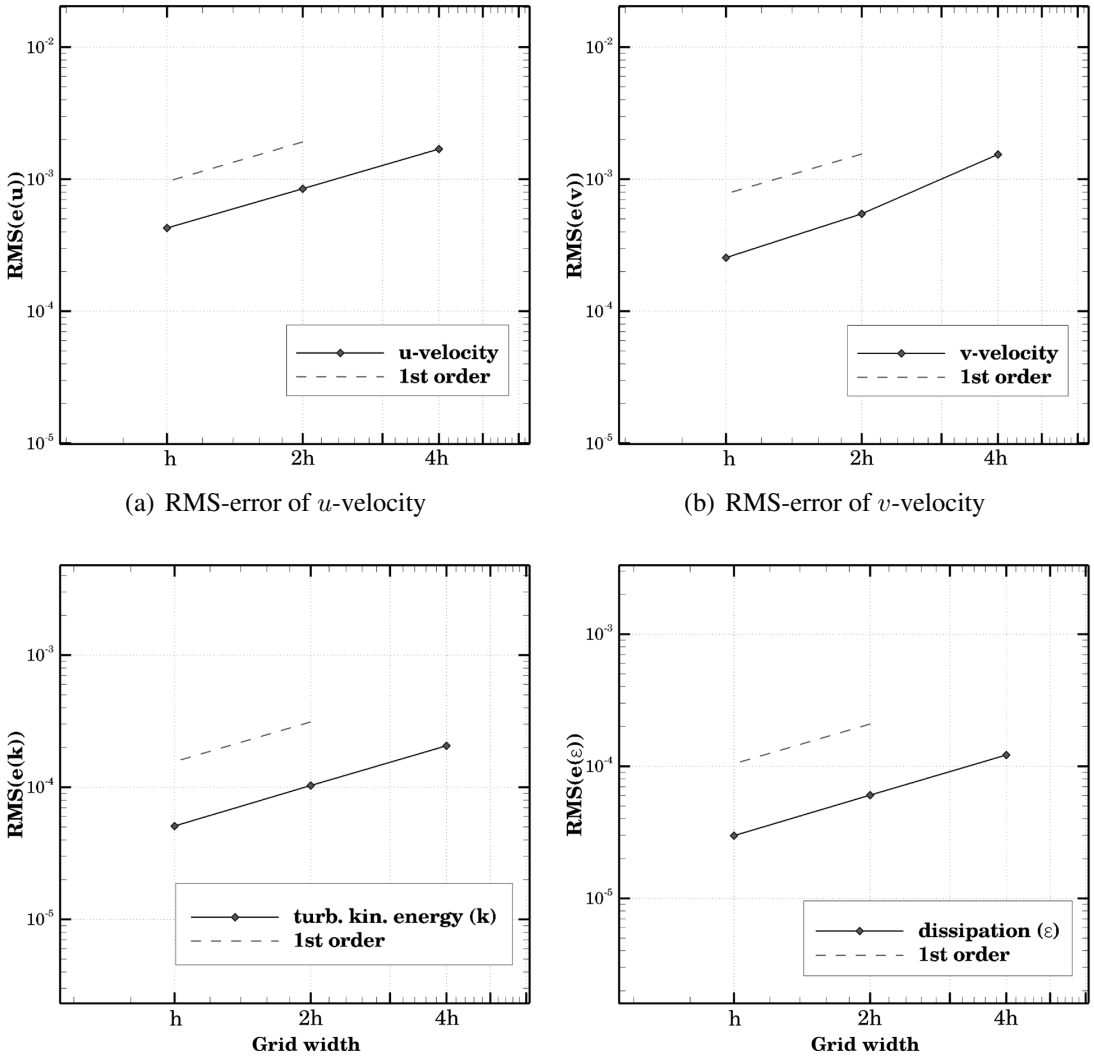

(a) RMS-error of u-velocity

(b) RMS-error of v-velocity

(c) RMS-error of turbulent kinetic energy k

(d) RMS-error of dissipation ε

Figure 5.2: Evolution of RMS-error for velocities and turbulent quantities obtained by Chien $k-\varepsilon$ model on different grids.

In the present simulation, the first order UDS scheme (details can be found in Section 4.2.1) is applied to convective terms in the momentum and transport equations. The observed order $p_c = 1$ corresponds to the formal order of accuracy p_0. Therefore, the Chien $k-\varepsilon$ model is implemented correctly. The deviation occurs only in the order of pressure, due to the pressure-velocity coupling algorithm (the values for the pressure cannot be set on the boundary; it is calculated from velocities), which is used in FASTEST code. From the evolution of the RMS-errors for u, v, k and ε on the different grids (in Figure 5.2, the stroke line presents the reference first order line), it can be recognized that the error tends to zero with the refinement of the mesh,

confirming the correct implementation of the Chien $k-\varepsilon$ RANS model.

Variable	RMS-error (201×201)	RMS-error (401×401)	Order
Velocity (u)	8.45×10^{-4}	4.26×10^{-4}	1.00
Velocity (v)	5.48×10^{-4}	2.54×10^{-4}	1.11
Pressure (p)	2.79×10^{-4}	1.51×10^{-4}	0.90
Turb. kinetic energy (k)	1.03×10^{-4}	5.09×10^{-5}	1.02
Dissipation (ε)	6.04×10^{-5}	2.97×10^{-5}	1.02

Table 5.1: RMS-error and order of accuracy obtained by verification of Chien $k-\varepsilon$ RANS model.

5.2.2 Verification of the $\zeta - f$ RANS model

In the following, the four equation $\zeta - f$ RANS model is verified with the manufactured solution. In addition to the solutions for k and ε, the solutions for the velocity scale ratio $\zeta = \overline{v^2}/k$ and for the elliptic relaxation function f must be designed.

The turbulent viscosity is defined as:

$$\nu_t = 2.5 \times 10^{-4}\, \eta_\nu^4\, \mathrm{e}^{(2-\eta_\nu^2)}, \tag{5.15}$$

with the non-dimensional similar variable η_ν (Equation 5.10).

For the manufactured solution of the turbulent kinetic energy, the following equation is used:

$$k = 0.01\, \eta_\nu^2\, \mathrm{e}^{1-\eta_\nu^2} + 0.01\ . \tag{5.16}$$

In the previous section, the dissipation rate follows from the manufactured quantities ν_t and k:

$$\varepsilon = 0.036\, \mathrm{e}^{\eta_\nu^2} + 0.01\ . \tag{5.17}$$

The manufactured solution for the velocity scales ratio is defined as following:

$$\zeta = 3.59\, \nu^2\, \mathrm{e}^{1-0.5\eta_\nu^2} + 0.01\ . \tag{5.18}$$

The constructed solution for the function f has the following form:

$$f = 7.18 \times 10^4 \frac{\eta_\nu^2}{y^2}\, \mathrm{e}^{1-\eta_\nu^2}\ . \tag{5.19}$$

In this form, the designed solution fulfills the condition for the elliptic relaxation function on the wall:

$$f_w = \lim_{y \to 0} \frac{-2\nu\zeta}{y^2}\ . \tag{5.20}$$

The $\zeta - f$ model is completed by limiting the time and length scales τ_ζ, L_ζ, (see Equation [3.21]). As the manufactured solution must be a monotone function, only part of the limits of the scales is investigated:

$$\tau_\zeta = C_\tau \left(\frac{\nu}{\varepsilon}\right)^{1/2} , \tag{5.21}$$

$$L_\zeta = C_\eta \left(\frac{\nu^3}{\varepsilon}\right)^{1/4} . \tag{5.22}$$

After the insertion of the manufactured solutions (5.16), (5.17), (5.18) and (5.19) in the transport equations for k, ε, ζ, f (3.16), the following source terms are obtained:

$$\begin{aligned} Q_k &= u\frac{\partial k}{\partial x} + v\frac{\partial k}{\partial y} - \left[\left(\nu + \frac{\nu}{\sigma_k}\right)\left(\frac{\partial^2 k}{\partial x^2} + \frac{\partial^2 k}{\partial y^2}\right) + \frac{1}{\sigma_k}\left(\frac{\partial \nu_t}{\partial x}\frac{\partial k}{\partial x} + \frac{\partial \nu_t}{\partial y}\frac{\partial k}{\partial y}\right)\right] \\ &\quad - \nu_t S + \varepsilon , \\ Q_\varepsilon &= u\frac{\partial \varepsilon}{\partial x} + v\frac{\partial \varepsilon}{\partial y} - \left[\left(\nu + \frac{\nu}{\sigma_\varepsilon}\right)\left(\frac{\partial^2 \varepsilon}{\partial x^2} + \frac{\partial^2 \varepsilon}{\partial y^2}\right) + \frac{1}{\sigma_\varepsilon}\left(\frac{\partial \nu_t}{\partial x}\frac{\partial \varepsilon}{\partial x} + \frac{\partial \nu_t}{\partial y}\frac{\partial \varepsilon}{\partial y}\right)\right] \\ &\quad - C_{\varepsilon_1}\frac{S}{\tau} + C_{\varepsilon_2}\frac{\varepsilon^2}{\tau} , \end{aligned} \tag{5.23}$$

$$\begin{aligned} Q_\zeta &= u\frac{\partial \zeta}{\partial x} + v\frac{\partial \zeta}{\partial y} - \left[\left(\nu + \frac{\nu}{\sigma_\zeta}\right)\left(\frac{\partial^2 \zeta}{\partial x^2} + \frac{\partial^2 \zeta}{\partial y^2}\right) + \frac{1}{\sigma_\zeta}\left(\frac{\partial \nu_t}{\partial x}\frac{\partial \zeta}{\partial x} + \frac{\partial \nu_t}{\partial y}\frac{\partial \zeta}{\partial y}\right)\right] \\ &\quad - \frac{\zeta}{k}S - f , \\ Q_f &= L^2\nabla^2 f - f - \frac{1}{\tau}\left(c_1 + C_2'\frac{S}{\varepsilon}\right)\left(\zeta - \frac{2}{3}\right) . \end{aligned} \tag{5.24}$$

The source terms (5.23) and (5.24) are summed up in the source code to transport equations for k, ε, ζ and f, accordingly. Then, the calculation for the computational case described in the beginning of this section is carried out on three grids of different refinements. Subsequently, the RMS-errors between the manufactured and the code solution are calculated for major quantities. The orders of accuracy and RMS errors on the two finer meshes are presented in Table 5.2.

As for the simulation with the Chien $k - \varepsilon$ model, convective terms in the momentum and transport equations are discretized with the first order UDS scheme. Therefore, the observed order $p_c = 1$ is in accordance with the formal order of accuracy $p_0 = 1$, which confirms the correct implementation of the $\zeta - f$ RANS model. The deviation occurs only in the order of pressure, due to the pressure-velocity coupling algorithm (see description in the previous section), and in the elliptic relaxation function. The last deviation is explained by the manner of

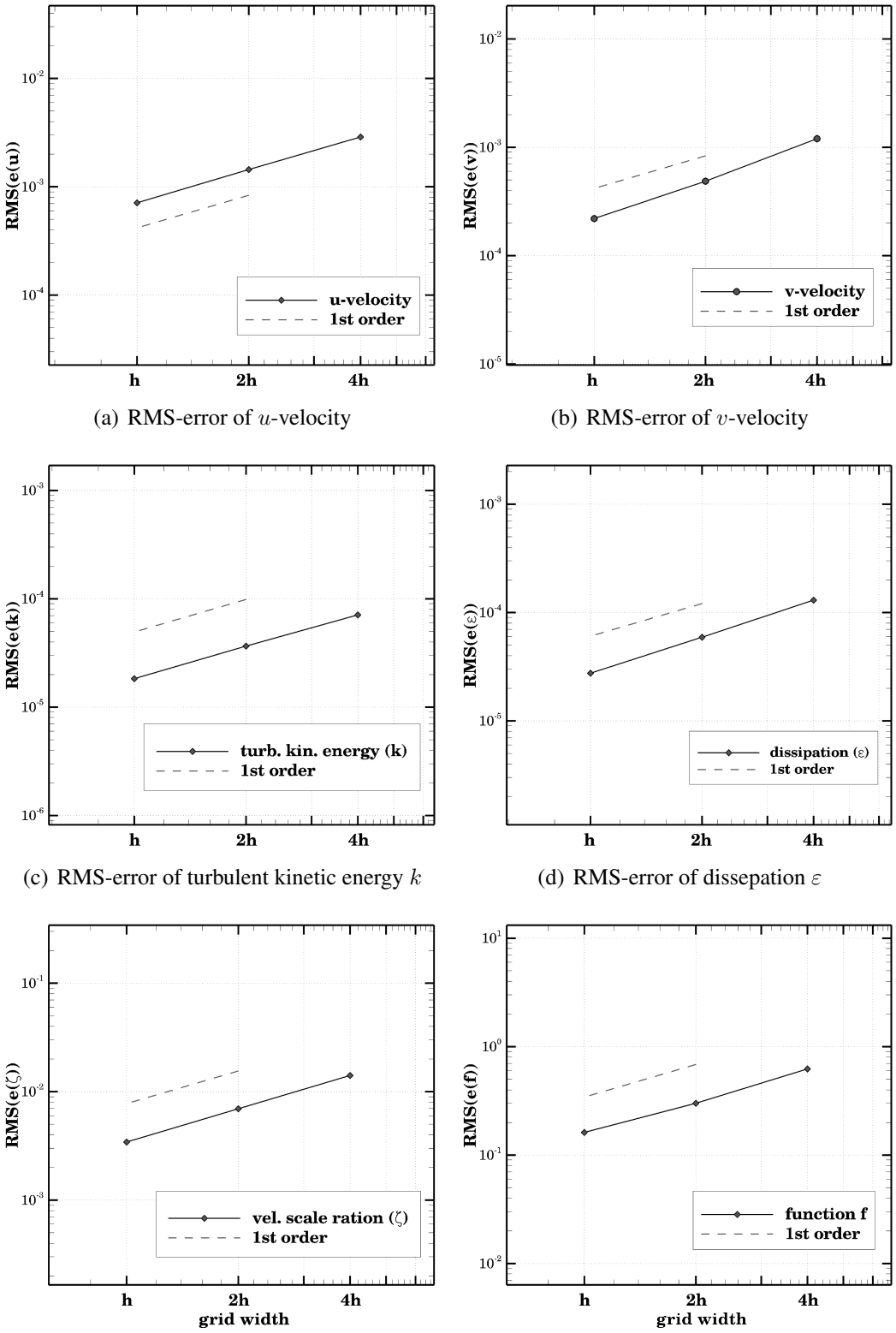

(a) RMS-error of u-velocity

(b) RMS-error of v-velocity

(c) RMS-error of turbulent kinetic energy k

(d) RMS-error of dissepation ε

(e) RMS-error of velocity scale ration k

(f) RMS-error of function f ε

Figure 5.3: Evolution of RMS-error for velocities and turbulent quantities obtained by $\zeta - f$ RANS model on different grids.

the implementation of the elliptic equation in code FASTEST, where the equation for f is solved with the algorithm for the standard transport equations. Figure 5.2 presents the evolution of the RMS-errors for u, v, k, ε, ζ and f (the stroke line presents the reference first order line). The error tends to zero with the refinement of the mesh for all quantities, as expected. This result additionally proves that the $\zeta - f$ model is implemented correctly.

Variable	RMS-error (201×201)	RMS-error (401×401)	Order
Velocity (u)	1.44×10^{-3}	7.12×10^{-4}	1.02
Velocity (v)	4.85×10^{-4}	$2,19 \times 10^{-4}$	1.15
Pressure (p)	2.66×10^{-4}	$1,49 \times 10^{-4}$	0.84
Turb. kinetic energy (k)	3.66×10^{-5}	1.83×10^{-5}	1.00
Dissipation (ε)	5.93×10^{-5}	2.75×10^{-5}	1.11
Velocity scales ratio (ζ)	6.93×10^{-3}	3.43×10^{-3}	1.01
Function f	3.01×10^{-1}	1.61×10^{-1}	0.91

Table 5.2: RMS-error and order of accuracy obtained by the verification of the $\zeta - f$ model.

6 Validation and Modification of the Very Large Eddy Simulation Model (VLES)

The main object of this chapter is the validation of the VLES model presented in Chapter 3. Therefore, the simulation results are compared with experiments or other reference data, such as DNS or LES results. After the validation of the standard VLES method, the influence of the filter width (i.e. is a part of the definition of the VLES approach), on the results is investigated.

In contrast to the verification procedure described in the previous chapter, where no physically correct solution is required, the goal of validation is to examine whether the implemented equations yield the correct physical results. Three different test cases are considered for the validation of the VLES model implemented in the in-house code FASTEST. These flow configurations were selected to demonstrate the ability of the VLES approach to predict different types of turbulent flows.

In the beginning of the present chapter, the flow over a two-dimensional periodic hill at $Re_b \approx 10,595$ is calculated. The challenge of this case is the correct prediction of the point of separation from the curved surface, which is not clearly dependent on the geometry and has a strong impact on the point of reattachment. This flow phenomenon is quite common in engineering applications; for example, similar effects occur in a flow over an airfoil. Moreover, this validation case demonstrates well the advantage of the VLES model compared to the RANS method. The second validation case is a fully-developed turbulent flow in a channel at $Re_\tau = 590$. This test case highlights the feasibility of the new hybrid model in computation of flows with attached boundary layers. Since the turbulent flows past bluff bodies include many flow phenomena, such as separation, reattachment or vortex shedding for the last test case the flow over the circular cylinder at $Re = 3,900$ was chosen to verify the performance of the VLES method in modeling of such complex flows.

In the second part of this chapter, the modified filter width is introduced in the formulation of the VLES approach. By means of the fully developed turbulent channel flow, the improvement of the results with this modification is demonstrated.

6.1 Validation of the very large eddy simulation model (VLES)

6.1.1 Flow over two-dimensional periodic hills

As a first validation case of the VLES model on a static grid the flow over two-dimensional periodic hills at a Reynolds number of $Re_b \approx 10,595$ is considered. The size of the computational domain in x-, y- and z-direction is defined in accordance with the available reference data as $L_x = 9h, L_y = 3.036h$ and $L_z = 4.5h$, with h being the hill height (Figure 6.1). On the top and bottom edges of the domain, the wall boundary conditions are applied, while periodic boundary conditions (BC) are assigned in streamwise and spanwise directions. The validation is conducted at the Reynolds number $Re = u_b h/\nu$ based on the bulk velocity u_b, which is defined as follows:

$$u_b = \frac{1}{2.035} \int_h^{3.036h} u(y)\, dy\,. \tag{6.1}$$

The computational domain illustrated in Figure 6.1 is covered with a mesh of 184320 (72x80x32) grid points, which fulfills the condition for the non-dimensional wall distance $y^+ \approx 1$ at the lower wall. After 20 flow-through times, the flow is averaged over at least 30 flow-through times to obtain statistical converged results. The results are also averaged in space over the spanwise direction. The simulation is compared to the reference LES data from Temmerman [159] obtained by a high-resolved simulation with $4.6 \cdot 10^6$ grid nodes.

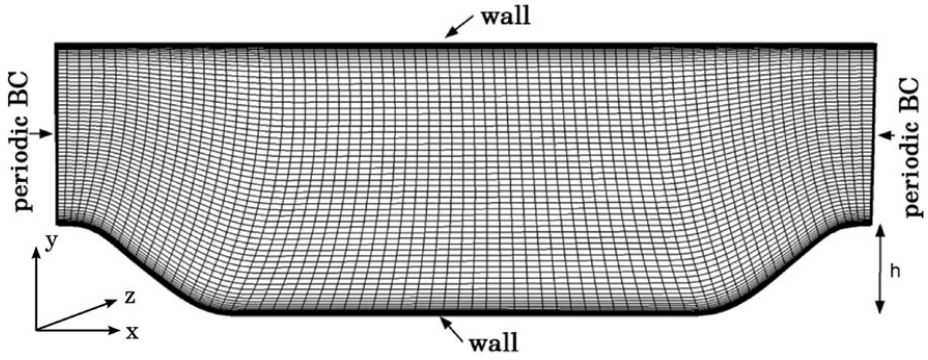

Figure 6.1: Computational domain and mesh for flow over periodic hills.

The reference results indicate that the flow separates in the proximity of the hill crest ($x_s = 0.2h$) and that a recirculation zone is generated in the downstream of the hill side until the flow is reattached near the middle of the channel ($x_r = 4.72h$). As mentioned at the beginning of the chapter, the separation of the flow is not clearly determined by the geometry; therefore it is especially challenging to correctly predict the separation and reattachment points x_s and x_r. It is well known that RANS models demonstrate weaknesses in this specific test case [87]. A typical outcome of many RANS models is insufficient intensity of the turbulence activity in

the separated region, resulting in a much larger recirculation zone. This results occurs due to the isotropy assumption applied in the RANS modeling, which does not include the anisotropic effects that appear in the recirculation region. Due to its ability to simulate the anisotropic effects in the near-wall region, the $\zeta - f$ RANS model shows better results than the other RANS models, as reported in Billard and Laurence [12]. Due to the combination of the RANS and LES or DNS methods, the hybrid models, such a VLES or DES, are able to reproduce these anisotropic effects and therefore very reliably predict separation and reattachment points.

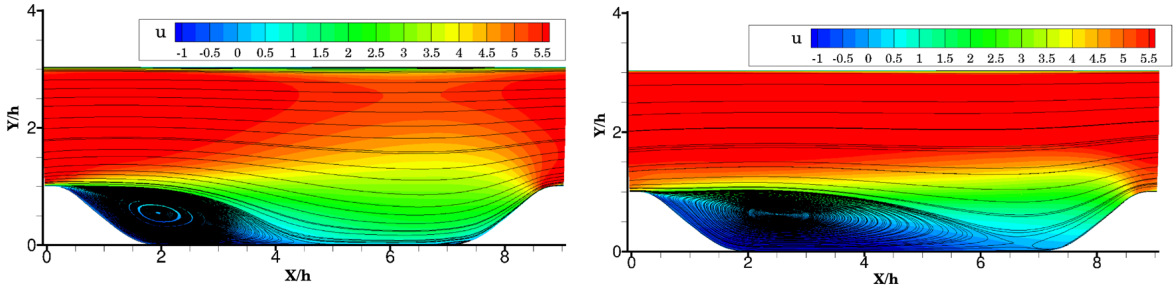

(a) VLES $k - \omega$ model (b) RANS $k - \omega$

Figure 6.2: Comparison of velocity field and streamlines for two-dimensional periodic hill flow for $k - \omega$ VLES and $k - \omega$ RANS model.

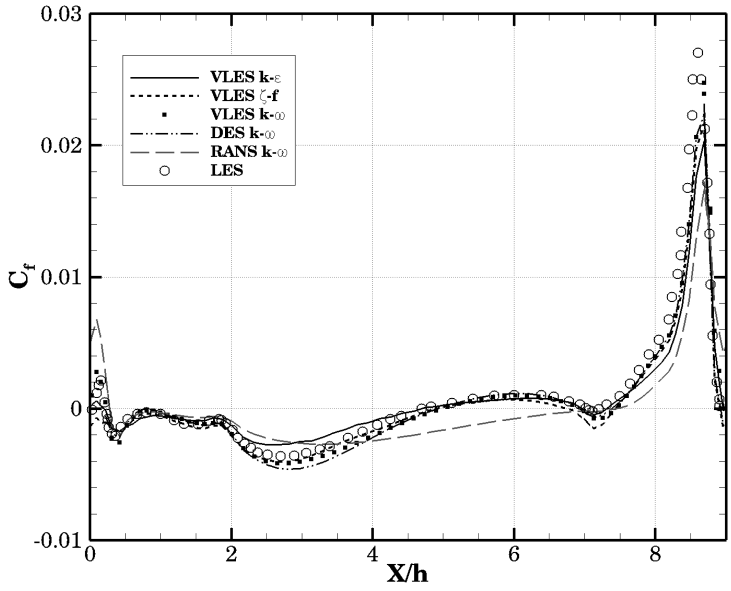

Figure 6.3: Skin friction coefficient along bottom wall for two-dimensional periodic hill flow.

Figure 6.2 illustrates the difference between results produced by VLES and RANS models. This comparison of the streamlines and velocity fields demonstrates that the recirculation zone in the

simulation with the VLES method occupies about 50% of the streamwise domain, while in the RANS simulation the separation region is much longer.

For a detailed comparison of the simulation results from the different turbulence models, the distribution of the skin friction coefficient $C_f = \tau_w / \frac{1}{2}\rho U_0^2$ along the lower wall is shown in Figure 6.3. The C_f obtained with the RANS method shows much deviation from the reference data, while the C_f values produced by different hybrid models demonstrate good agreement with the data presented in literature. Due to the ability of ER models to behave like LES models in the separation region, the results are improved in comparison to the RANS method (see Figure 6.7). The $k-\varepsilon$ VLES model underpredicts the friction coefficient value in the recirculation region; however, the separation and reattachment points are captured very well. This graphic also reveals that the predictive accuracy of the VLES method depends on the specific RANS turbulence model. For example, the VLES based on the $\zeta - f$ model shows most agreement with the reference data in the separation region. This higher level of agreement can be explained by the properties of the $\zeta - f$ RANS model described in Section 3.1.4, which considers the near-wall anisotropy. The detailed separation and reattachment positions obtained with different models are listed in Table 6.1. All three VLES approaches capture the position of the separation and reattachment very well.

Model	x_s	x_r	error x_s	error x_r
ref. LES Temmerman [159]	0.22	4.72	-	-
VLES $k-\varepsilon$	0.20	4.70	9.09 %	0.42 %
VLES $\zeta - f$	0.21	4.90	4.55 %	3.81 %
VLES $k-\omega$	0.22	5.04	0.00 %	6.78 %
DES $k-\omega$	0.25	5.04	13.64 %	6.78 %
RANS $k-\omega$	0.29	7.56	31.82 %	60.17 %

Table 6.1: Separation and reattachment points for different VLES models.

In the rest of this section, only the results produced by the VLES model are presented, since the VLES approach is of central interest for this work. For the sake of clarity, the diagrams of velocities and Reynolds stresses show results obtained only by the $\zeta - f$ and the $k-\varepsilon$ VLES model, since the values produced by all three VLES models are almost identical. Because $\zeta - f$ and the $k-\varepsilon$ VLES model are investigated in following on the moving grid and in the context of FSI, they are chosen.

A detailed depiction of the mean velocities is presented in Figure 6.4, which illustrates the velocity profiles obtained with $\zeta - f$ and $k-\varepsilon$ VLES models at eight different positions in the x-direction, as compared to the reference LES solution. The recirculation region is characterized by a negative velocity, which detects the detachment of the boundary layer in the near-wall

region. The comparison shows that the difference between the two compared VLES models is minor and that both approaches produce very reasonable predictions.

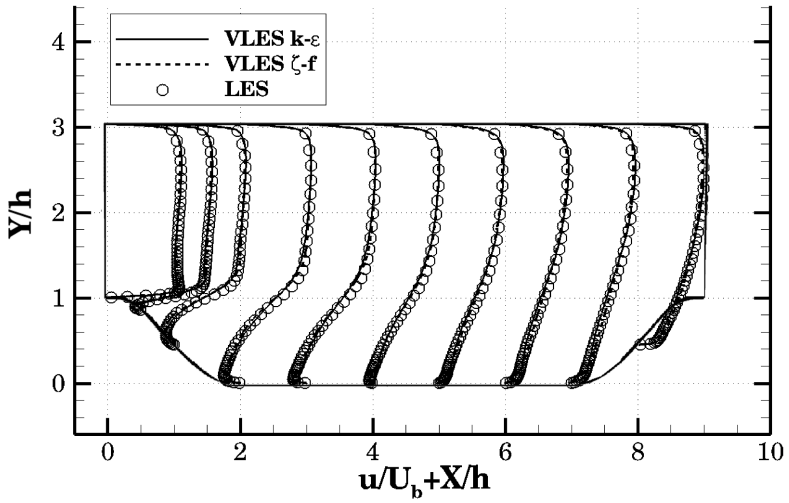

Figure 6.4: Mean velocity profiles for $k-\varepsilon$ and $\zeta-f$ VLES models for two-dimensional periodic hill flow.

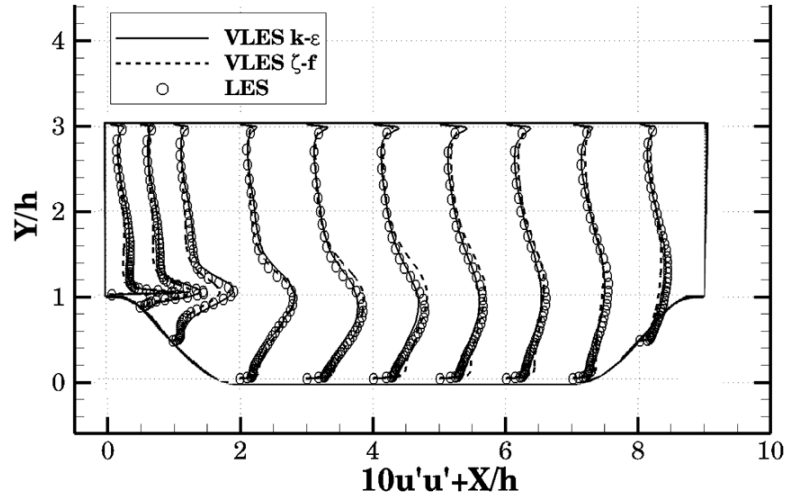

(a) $u'u'$ Reynolds stresses.

Figure 6.5: Reynolds stress profiles for $\zeta - f$ and $k - \varepsilon$ VLES models for two-dimensional periodic hill flow.

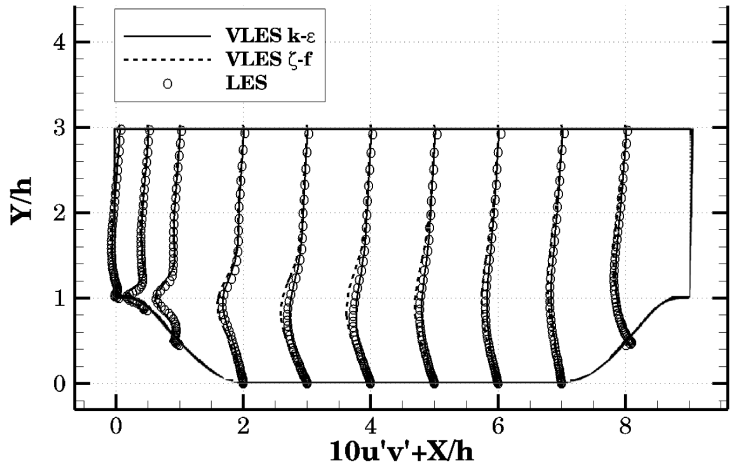

(a) $u'v'$ Reynolds stresses.

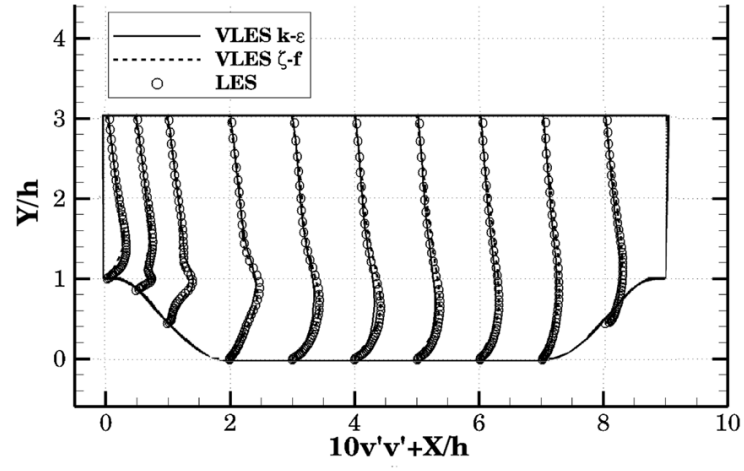

(b) $v'v'$ Reynolds stresses.

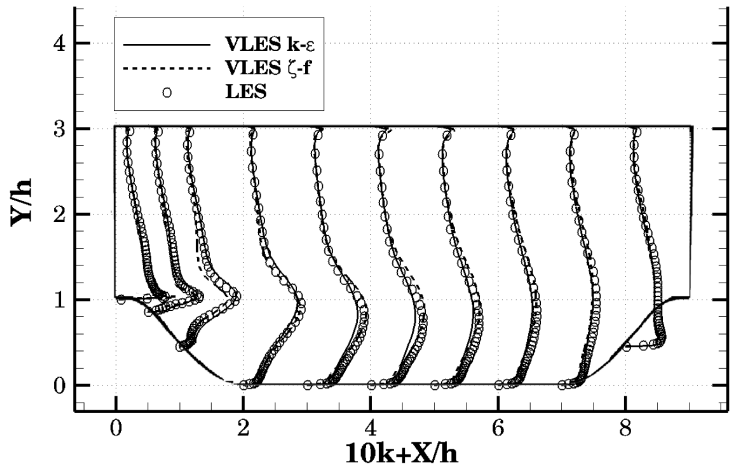

(c) turbulent kinetic energy.

Figure 6.6: Reynolds stress profiles and turbulent kinetic energy for $\zeta - f$ and $k - \varepsilon$ VLES models for two-dimensional periodic hill flow.

Figure 6.5 and Figure 6.6 offer a comparison of Reynolds stresses and the turbulent kinetic energy obtained by the simulations with VLES models and the results of LES. The small deviations in the Reynolds stresses occur in the middle of the lower boundary for both VLES models. The Reynolds stresses and the turbulent kinetic energy obtained with the $k - \varepsilon$ VLES are insignificantly underpredicted. This finding is consistent with the friction coefficient values in Figure 6.3, since the intensity of the recirculation zone is underpredicted. The $u'u'$-Reynolds stresses obtained by the $\zeta - f$ VLES simulation are slightly overpredicted in the middle of the channel, while other quantities are predicted very well, and therefore the separation and reattachment points accord with the extant literature [159]. In general, the obtained Reynolds stresses and the turbulent kinetic energy are in quite good agreement with the reference data and other VLES results reported in [24].

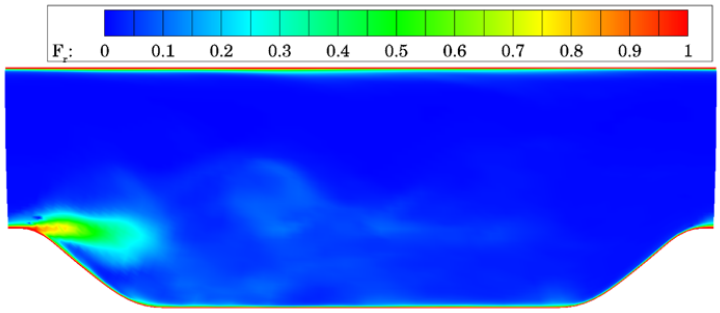

(a) Resolution control function F_r.

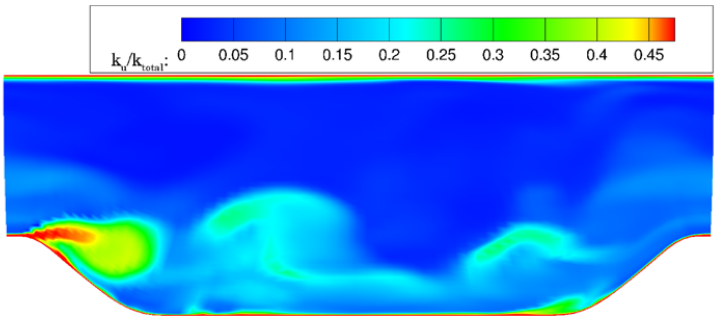

(b) Modeling ration.

Figure 6.7: Modeling parameter F_r and modeling ratio k_u/k_{total} for $\zeta - f$ VLES model for two-dimensional periodic hill flow.

A very important issue for the hybrid models is the modeling ratio, presented in Figure 6.7 (b). It is a rate between the modeled (unresolved) and total turbulent kinetic energy. The model part in the VLES simulation consist of about 45% maximally. This value is achieved in the vicinity of the wall, where the RANS mode dominates. According to the theory (see [48]), about $70 - 80\%$ of the turbulent kinetic energy should be resolved. Therefore it is well recognized that in the middle of the computational domain, the VLES model behaves like a LES method,

since the modeled part is much smaller. In Figure 6.7 (a), the resolution control function F_r as a modeling parameter confirms the results from Figure 6.7 (b). The RANS mode is active in the near-wall region, while the LES dominates in the separation zone, and in the rest of the domain the modeling part is minimal, meaning that the VLES model tends to DNS mode.

Subsequently, by means of the two-dimensional periodic hill flow, it could be shown that the VLES model is able to predict the separation flows very well even on the coarse grid, as compared to the LES simulation, which requires a minimum of two million cells for the correct prediction of this flow.

6.1.2 Fully developed turbulent flow in channel

The second case for the validation of the VLES model is a fully developed flow between two parallel flat plates at a Reynolds number of $Re_\tau = 590$ based on the friction velocity u_τ and the half of the channel width h. This case is a common test case to demonstrate the important feasibility of turbulence models to predict wall-bounded flows. A wide range of calculation results for different Reynolds numbers can be found in literature; for instance, the simulation results at $Re_\tau = 590$ obtained by the VLES model are reported in Han and Krajnović [60] and those for the channel flow at $Re_\tau = 395$ in Chang et al. [24]. Moreover the investigation of the channel flow at $Re_\tau = 395$ achieved by the commonly used hybrid model DES is reported in [57] and [143], while the results of the LES calculation can be found, for example, in [76] or [94].

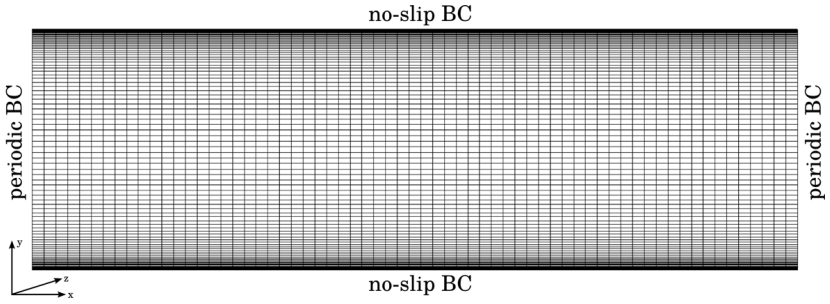

Figure 6.8: Computational domain for channel flow at $Re_\tau = 590$.

The size of the computational domain is chosen in accordance with other simulations obtained by the hybrid models and defined as $L_x = 2\pi$ in the streamwise direction (x), $L_y = 2$ in the wall-normal direction (y) and $L_z = \pi$ in the spanwise direction (z). In x- and z-directions, periodicity is assumed, while on the top and bottom wall, no-slip boundary conditions are imposed. The flow is derived by the streamwise pressure gradient $dp/dx = \tau_w/h$.

A mesh for the VLES simulation illustrated in Figure 6.8 consists of $64 \times 100 \times 64$ grid points, with the first grid node located at the normalized wall distance $y^+ \approx 1$. For the numerical convection scheme, the CDS method is used, and for time discretization, the implicit time scheme is applied. The flow is averaged in time over 30 flow-through times.

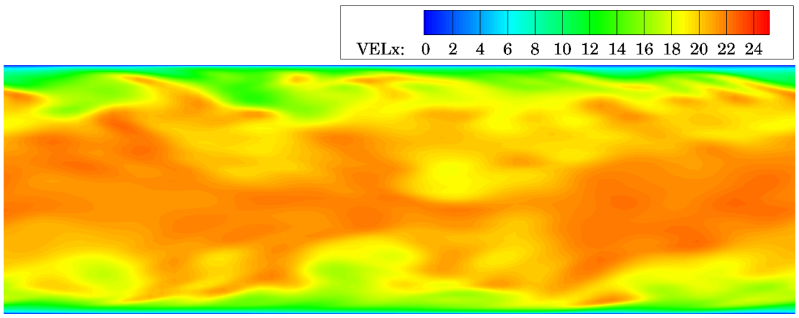

(a) Mean-velocity field obtained by the VLES model

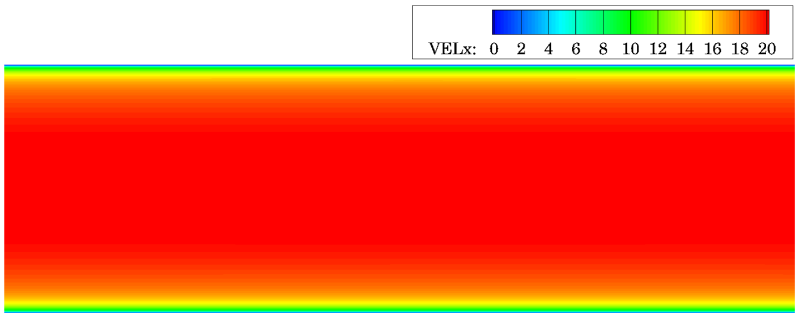

(b) Mean-velocity field obtained by RANS model

Figure 6.9: Difference in the mean-velocity field for $k-\omega$ RANS and $k-\omega$ VLES models for channel flow at $Re_\tau = 590$.

As can be seen from Figure 6.9, the VLES calculation (Figure 6.9 [a]) yields the unsteady and inhomogeneous flow feature in the channel, the eddy structures are captured by this simulation in contrast to the RANS calculation (figure 6.9 [b]), where the velocity field stays steady without turbulent structures.

Figure 6.10 (a) demonstrates the mean streamwise velocity from the DNS data, contributed by Moser et al. [112], in comparison to the VLES results given by different background RANS models. Here and in the following, the results are averaged in space over the spanwise and the streamwise directions. The mean velocities obtained by the VLES approach based on the $k-\omega$ model are underpredicted in the buffer layer and insignificantly overpredicted in the log-low region. The profile of the mean velocity is not captured correctly. The reason, therefore, is the high sensitivity of the $k-\omega$ VLES model to the mesh resolution, as reported in [58]. A refinement of the grid in the z-direction improves the results. However, the velocities achieved from the $k-\varepsilon$ and $\zeta - f$ VLES calculations are reasonably well predicted. The velocities obtained by the $k-\varepsilon$ VLES model are insignificantly overpredicted in the log-law region ($30 < y+ < 100$), but the maximum of the mean velocity in the middle of the channel is captured very well. Compared to the DNS simulation the best results are achieved by the $\zeta - f$ VLES model in all three regions of the boundary layer (listed in Section 2.4.4). A similar tendency has been shown in the previous

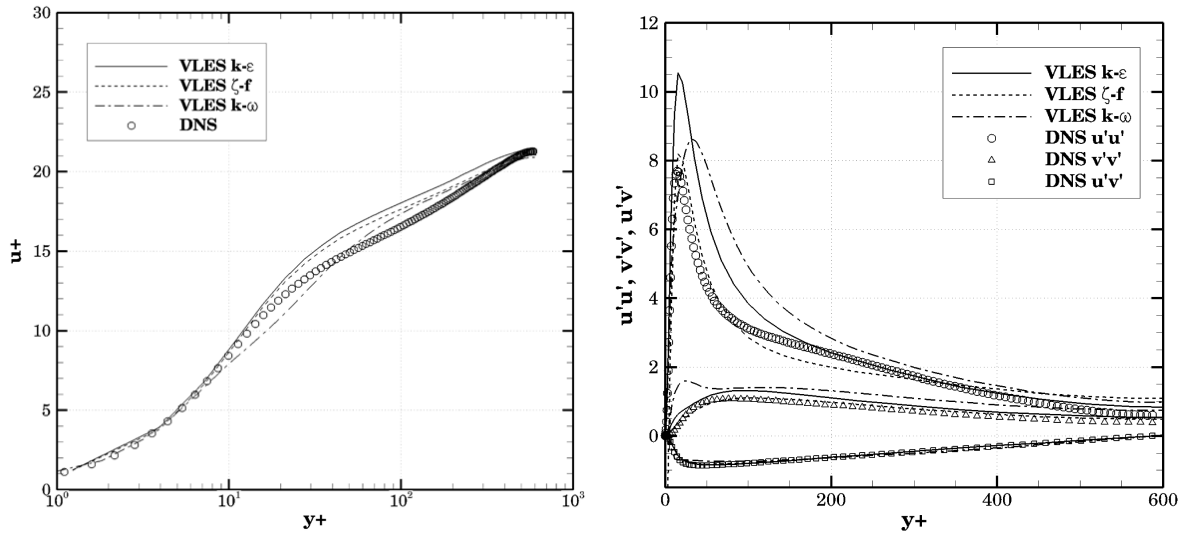

(a) Mean velocity profiles

(b) Reynolds stress components

Figure 6.10: Mean velocity profiles and Reynolds stress components for different VLES models in comparison to DNS data [112] for channel flow at $Re_\tau = 590$.

section, where the $\zeta - f$ VLES model shows the best agreement with the reference data for a flow with separation.

Figure 6.11 illustrates the influence of mesh resolution on the results of the VLES model. In this figure, the velocity profile obtained by the VLES $k - \varepsilon$ and the VLES $\zeta - f$ models for two different grids (Grid 1: $32 \times 50 \times 64$ and Grid 2: $64 \times 100 \times 64$) are presented in comparison with the reference data. The figure shows that with refinement of the mesh the results move towards the DNS data.

The Reynolds stress components produced with different VLES methods together with the reference DNS data are presented in Figure 6.10 (b). The VLES approach based on the $\zeta - f$ model predicts the results quite well for the three presented components. The VLES $k - \varepsilon$ approach shows good agreement in the $v'v'$ and $u'v'$ components, while the values for $u'u'$ are overpredicted in the boundary layer ($y_+ < 100$), similar to the velocity profiles for this method. However, the position of the peak of the $u'u'$-Reynolds stress component is captured very well. As expected, the Reynolds stresses yielded by the $k - \omega$ VLES model show the biggest deviations from the reference data, especially for the dominant $u'u'$ components, where the values are strongly overpredicted.

In addition to the turbulent flow in a channel at $Re_\tau = 590$, the channel flow at $Re_\tau = 395$ was investigated. In this investigation, the computational domain and the grid were assumed from the test case at $Re_\tau = 590$. The results of the simulation for the channel flow at lower Reynolds number for three different VLES models can be found in Figure 6.13. The turbulence models yield better results in the channel flow at the lower Reynolds numbers, when the mesh is the same

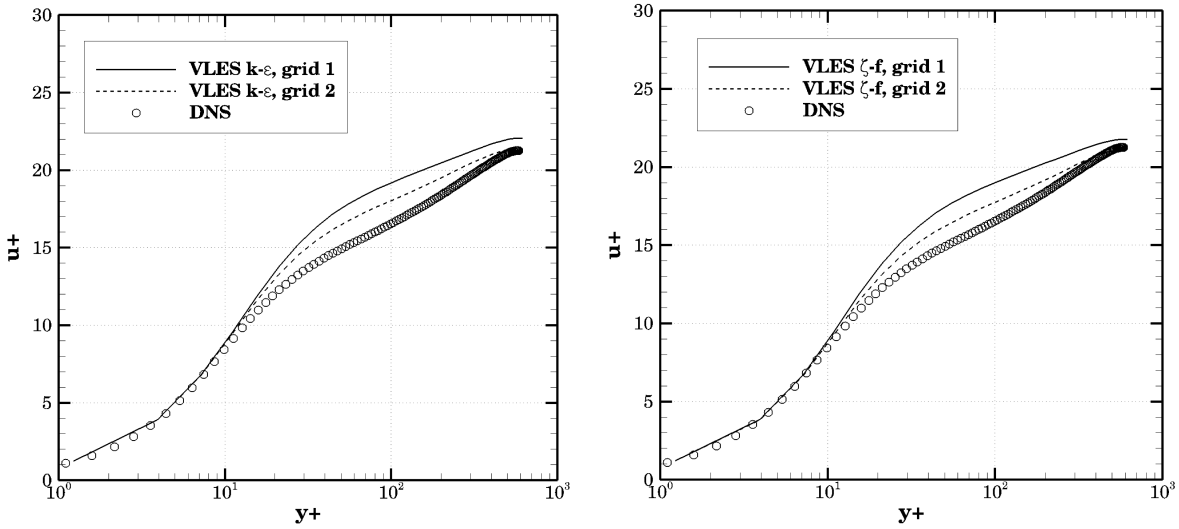

(a) VLES $k-\varepsilon$ model. (b) VLES $\zeta-f$ model.

Figure 6.11: Comparison of mean velocity profiles for coarse and fine mesh for channel flow at $Re_\tau = 590$.

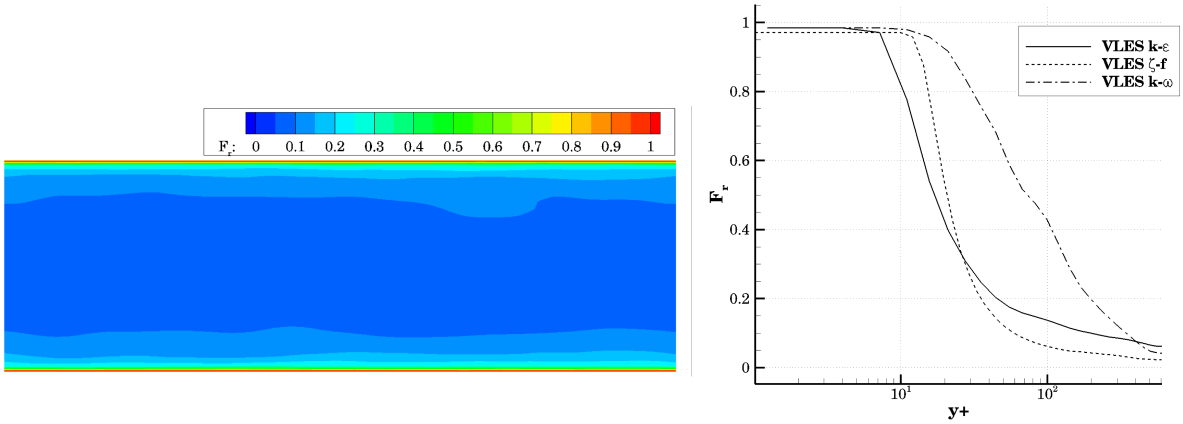

(a) Distribution of resolution control function in computational domain. (b) Profiles of the resolution control function F_r.

Figure 6.12: Resolution control function F_r for $k-\varepsilon$ VLES model for channel flow at $Re_\tau = 590$.

as when applied for the calculation at higher Re. Since the turbulent eddies become smaller with the increasing Reynolds number, the simulation of the channel flow for different Re on the equal grids leads to a lower resolution for the turbulent structures, especially in the vicinity of the wall.

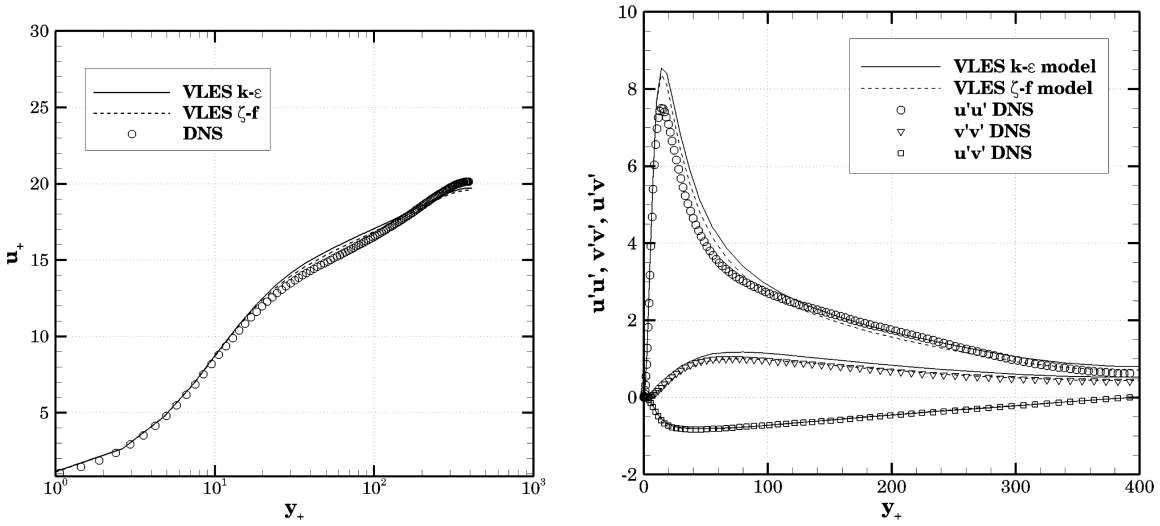

(a) Mean velocity profiles

(b) Reynolds stress components

Figure 6.13: Mean velocity profiles and Reynolds stress components in comparison to DNS data [112] in channel flow at $Re_\tau = 395$.

Consequently, larger deviations from the reference data occur with increasing Re. The results of all models for the flow between two parallel flat plates demonstrate better agreement with the reference data at Reynolds number $Re_\tau = 395$ for the velocities profiles as well as for the Reynolds stresses.

The distribution of the RANS and DNS-LES mode in the channel by the VLES simulation is illustrated by means of the resolution control function F_r in Figure 6.12 (a). The F_r field has a similar character in all three investigated VLES models. Therefore the resolution control function over the whole computational domain is presented for only the $\zeta - f$ VLES model. The modeled part is prevalent in the near-wall region, where the F_r function tends to one, while most of the scales are resolved in the middle of the channel where $F_r \longrightarrow 0$. This behavior accords with the theory highlighted in Section 3.3. For the F_r profiles in the wall-normal direction the results of all three VLES models are displayed in Figure 6.12 (a). Deviations in the values of F_r function obtained by the $k - \omega$ VLES method from the values produced by the other two VLES models are well recognized. While in the $\zeta - f$ VLES model the RANS mode is mainly active in the viscose layer (up to $y_+ \approx 7$), in the $k - \omega$ VLES method the RANS mode is much larger and is valid up to the logarithmic region (up to $y_+ \approx 30$). Moreover, the transition between RANS and DNS mode is slower in the $k - \omega$ VLES approach than in the two other methods. This behavior of the F_r function is responsible for the deviations in the results produced by the $k - \omega$ VLES model.

The VLES approach based on the $k - \varepsilon$ and $\zeta - f$ models shows reasonably close agreement with the reference data for the bounded flow considering that the mesh is quite coarse. The

velocity profiles as well as the Reynolds stresses are in good agreement with the data found in the literature. The $k-\omega$ VLES approach shows weaknesses on the current grid. For improvements of the results this method requires a finer mesh than the two other models require. Section 6.2 highlights, how the results produced by the $k-\omega$ VLES model can be improved by the introduction of the modified filter width without refining the grid.

6.1.3 Flow over circular cylinder

The last simulation case to demonstrate the abilities of the VLES model is the flow over a circular cylinder. The flows past a bluff body, such as a circular cylinder, are relevant in a wide range of engineering applications. For instance, such flow presents one of the most studied cases in aerodynamics. Flow over a two-dimensional circular cylinder is a challenging test case because the flow is characterized by the boundary layer separation without a fixed separation point and by strong flow oscillations in the wake region behind the body, the so-called Karman vortex street.

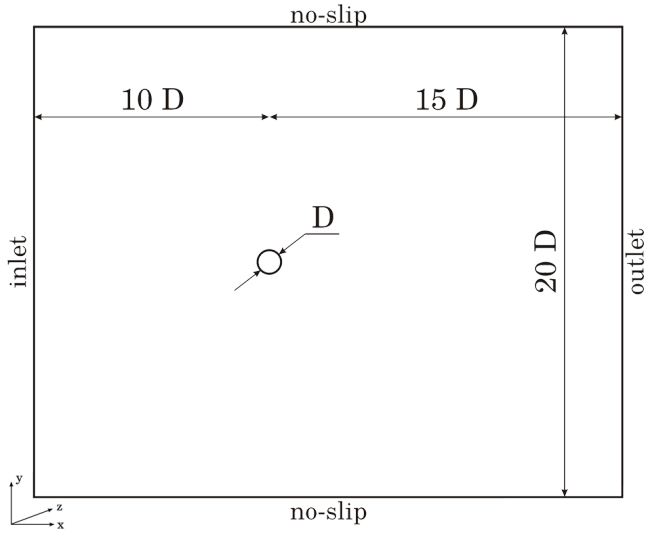

Figure 6.14: Computational domain for cylinder flow at $Re = 3,900$.

The present section investigated the flow over the circular cylinder at a Reynolds number of $Re = 3,900$ (based on the cylinder diameter D and the freestream velocity u_0). The computational domain in the streamwise direction extends $10D$ before the cylinder and $15D$ behind it. In the wall-normal direction the cylinder is found in the middle of the channel with a height of $20D$. The length of the channel in the spanwise direction is equal to πD. On the top and bottom surfaces, symmetry boundary conditions are imposed, while in the spanwise direction periodic boundary conditions are applied (see Figure 6.14). This test case is widely investigated and different experimental data are available in the literature. As reported in [47] and [99], this flow is very sensible to the spanwise length of the computational domain, to the boundary conditions and to small disturbances caused by insufficient resolution. Ma et al. [99] have shown by means of DNS that depending on the length of the domain in the z-direction, the size of the recirculation

zone becomes shorter or longer. For the present work the experimental data from Lourenco and Shih [97] and from Ong and Wallace [116] are used for reference, where the experimental domain extends πD in the spanwise direction. The same experimental results are chosen for reference data in the work of, for example, Breuer [18], Kravchenko and Moin [86] and Lübcke et al. [98], where the flow over the circular cylinder with the LES model is investigated.

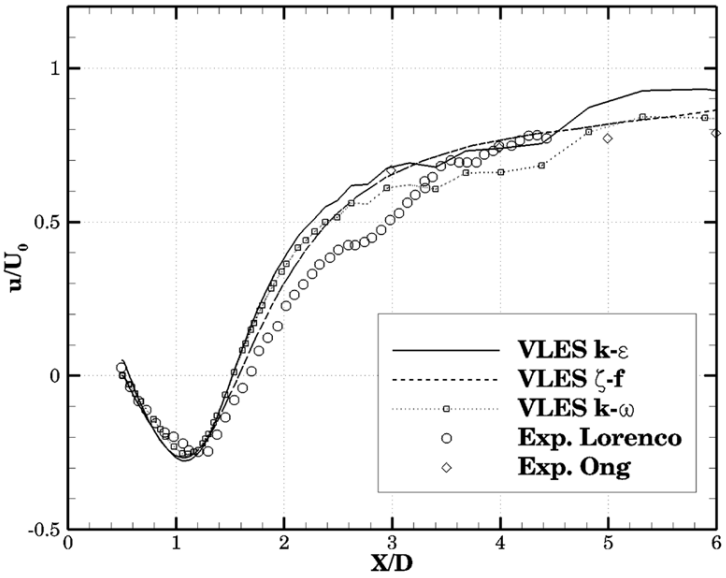

Figure 6.15: u-velocity along $y = 0$ for cylinder flow.

The solution domain is meshed with a block-structured grid, clustered around the cylinder. The mesh consists of $550,000$ control volumes, with the first node near the cylinder set at $y^+ \approx 1$. The grid has 32 cells in the z-direction, in accordance to the results reported in [60]. It is important to emphasize, that the mesh is much coarser than the one used for the LES simulation mentioned in [18] and [86], where the grid consists of approximately 11 million cells. In the current simulation, the second-order CDS is used for the discretization of the convective term, while for the turbulent quantities the QUICK scheme is applied. The time term is discretized as in the previous two test cases with the second-order implicit scheme.

The mean stream velocity along the centerline obtained with the different VLES models in comparison to the experimental data is plotted in Figure 6.15. This velocity profile demonstrates, that the flow separates on the cylinder sides and then joins at the free reattachment point in $x \approx 1.33$ at the symmetry plane. The VLES results with different underlying RANS models demonstrate quite close agreement with the reference data. A difference can be seen in the minimum value of the velocity. Here (see Table 6.2) the best agreement with the experiment is shown in the simulation with the VLES $\zeta - f$ model, as in the two previous cases. However, the position of the minimum value is predicted better by the VLES $k - \omega$ model, which very well captures also the length of the recirculation zone (see Table 6.2). In the wake region after the recirculation zone, the values produced by the $k - \omega$ and $k - \varepsilon$ VLES approaches are insignificantly overpredicted,

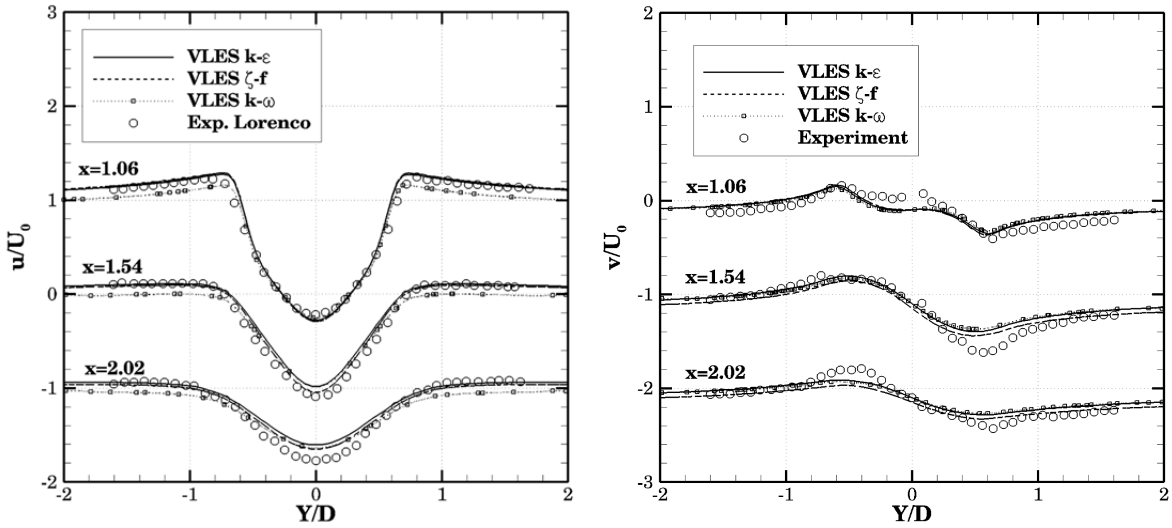

(a) u velocity profiles (b) v velocity profiles

Figure 6.16: Velocity profiles at three different positions in wake region for cylinder flow.

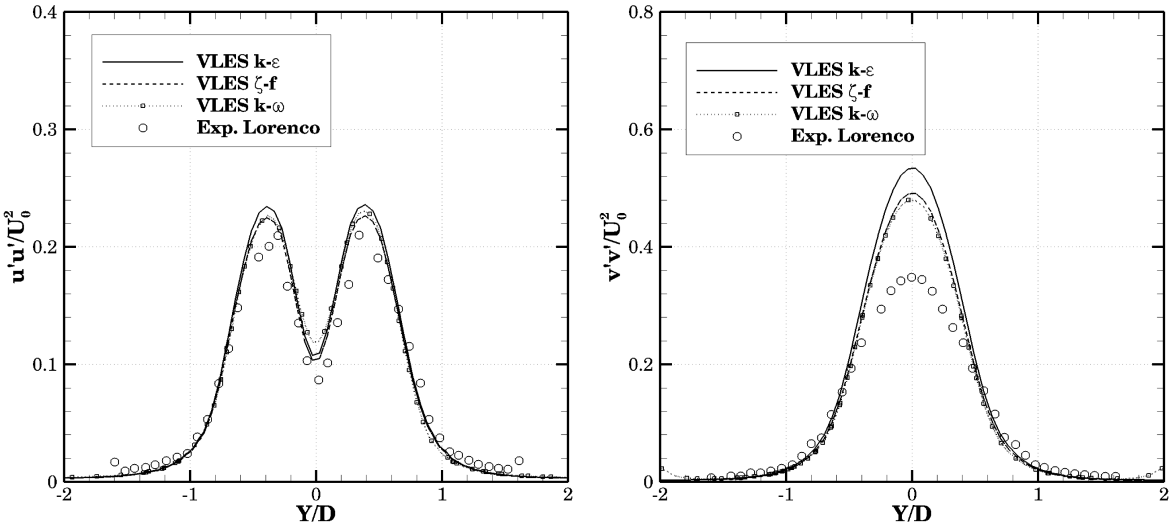

(a) $u'u'$-Reynolds stresses (b) $v'v'$-Reynolds stresses

Figure 6.17: Reynolds stresses at $x_2 = 1.54$ for cylinder flow.

while the VLES $\zeta - f$ model captures the maximum value of the velocity in this region very well.

For a detailed investigation of the velocities, the streamwise velocity profiles for three different positions in the x-direction ($x_1 = 1.06, x_2 = 1.54; x_3 = 2.02$) are plotted in Figure 6.16 (a). The VLES models accurately capture the form of the mean velocity profiles in all three positions next to the cylinder. However, in the profiles of the v-velocities deviations occur in the position $x_2 = 1.54$, while in the other two positions the velocities are captured well.

Figure 6.17 shows the Reynolds stresses in the position $x = 1.54$ for different VLES models in comparison with the experimental data. The $u'u'$-Reynolds stresses obtained by the VLES models are in very good agreement with the reference data, while deviations occur in the $v'v'$ components. The same effect is described by Breuer in [18].

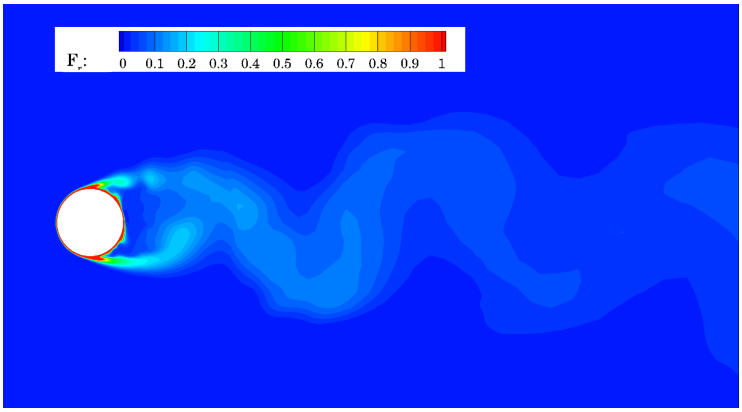

(a) Resolution control function F_r

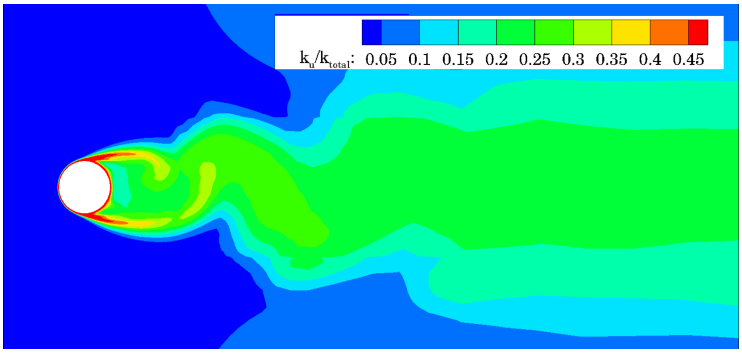

(b) Modeling ratio k_u/k_{total}

Figure 6.18: Resolution control function F_r and modeling ratio k_u/k_{total} for cylinder flow.

The resolution control function is displayed in Figure 6.18 (a). For all three models, the distribution of the resolution function has a similar character. The F_r function tends to zero on the cylinder surface, where the no-slip boundary conditions are applied, and therefore the RANS mode dominates. In the rest of the computational domain, the VLES model behaves like a LES model, since a part of the scales is resolved and another part is modeled. The ratio of the modeled turbulent kinetic energy to the total kinetic energy demonstrates, that no more than $20 - 30\%$ of

the scales are modeled (see Figure 6.18 [b]), and most of these scales are located near the cylinder.

Model	C_D	Θ	L_r/D
ref. experiment	0.98 ± 0.05	85.0 ± 2.0	1.33 ± 0.2
ref. LES[18]	1.07	87.6	1.21
VLES $k-\varepsilon$	1.17	88.45	1.02
VLES $\zeta - f$	1.12	88	1.07
VLES $k-\omega$	1.13	88.8	1.02

Table 6.2: Comparison of flow parameters for cylinder flow.

The main flow parameters for the VLES model, together with values from experiment and the LES data are listed in Table 6.2. The length of the recirculation zone L_r/D is insignificantly underpredicted by the VLES models, as demonstrated in Figure 6.15. The drag coefficient C_D obtained by the VLES models, as well as the separation angle Θ, agree well with the reference data. The difference is minor for the results produced by the VLES models with different underlying RANS models.

This challenging test case confirms that the VLES approach performs well for complex configurations. The drag coefficient values are predicted very well. Some minor deviations occur in the recirculation zone for the velocity components. They can be explained by the sensitivity of this flow to the simulation parameters, such as domain length in the spanwise direction or the boundary conditions, as mentioned in the beginning of this section.

6.2 Influence of filter width criterion

The main idea behind the VLES model is to switch between RANS and DNS modes, depending on the numerical grid resolution, by means of the resolution control function F_r. This quantity determines the ratio of resolved to modeled scales in the VLES method, and due to this ratio, F_r damps Reynolds stresses in the momentum equation. The definition of the resolution control function F_r introduced in Section 3.3 (see Equation (3.3)) contains the integral length scale $l_0 = k^{3/2}/\varepsilon$ and the turbulent cut-off $l_c = C_x\Delta$, which in turn depends on the filter width Δ. Therefore, a variation of the filter width can lead to a change in values of the resolution control function, which implies modifications in the interface between RANS and DNS-LES mode. As a consequence, an improvement or impairment of overall results can occur. In this context, the choice of the expression for the filter width may play an essential role, especially in the case of strongly anisotropic grids, which are frequently used in practice for wall-bounded flows.

In the present section two additional filter criteria are investigated on three grids with systematic refinements by means of a fully developed flow in a channel at $Re_\tau = 395$.

As mentioned in Section 3.3 the standard LES filter width (volume criterion) is used in the original formulation of the VLES model:

$$\Delta_{vol} = (\Delta_x \Delta_y \Delta_z)^{1/3} \ . \tag{6.2}$$

For the study of the behavior of the VLES model with different Δ, two additional filter widths were chosen: the criterion based on the maximum of the control volumes sides Δ_{max} (maximum criterion):

$$\Delta_{max} = \max(\Delta_x \ , \Delta_y \ , \Delta_z) \ , \tag{6.3}$$

and the IDDES formulation introduced by Travin [162] for the DES model [162] (IDDES criterion):

$$\Delta_{IDDES} = \min(\max[C_w d_w, C_w h_{max}, h_{wn}], h_{max}) \ , \tag{6.4}$$

where d_w denotes a distance to the wall, h_{wn} is a grid distance in the wall-normal direction, h_{max} is a maximum local grid spacing, and $C_w = 0.15$ is a constant. The formulation (6.4) includes an explicit wall-distance dependence and improves the distribution of F_r in the vicinity of the wall. For the DES, introducing this filter width has helped to resolve the mismatch in a log layer. This filter width modification is easy to implement, and this formulation does not require any additional computational effort [143].

Since the $k - \omega$ VLES model showed the most significant deviations to the reference data in Section 6.1.2, this model is selected to demonstrate the influence of the different filter widths on the results produced by the VLES model.

The computation domain and boundary conditions for the plane channel flow at $Re_\tau = 395$ are identical to the settings presented in section 6.1.2 (Figure 6.8). Calculations are performed on three grids with different level of refinement: Grid 1 ($64 \times 50 \times 64$ control volumes), Grid 2 ($64 \times 100 \times 64$ control volumes) and Grid 3 ($64 \times 100 \times 128$ control volumes). As a reference, the DNS data obtained by Moser et al. [112] are used.

Figure 6.19 demonstrates the mean velocity profiles produced by the $k-\omega$ VLES model for three different filter widths on meshes with different refinement in comparison to the DNS data. On the coarse grid (Figure 6.19 [a]) all criteria demonstrate deviations from the reference data. The VLES model with the IDDES criterion coincides quite well with the DNS data in the buffer layer; however, differences occur in the logarithmic region, where the behavior of the VLES method with the IDDES filter width approaches the behavior of the standard VLES model. On Grid 2 the IDDES-VLES approach agrees strongly with the reference data, in contrast to the other criteria, which are mismatched in the logarithmic region and the buffer layer. The difference from the DNS simulation results decreases in comparison to the coarse grid, and on the finest mesh the VLES model with all Δ criteria demonstrates very good agreement with the reference data. It can be observed from the results that with an increase of the number of control volumes, the VLES results become less dependent on the filter width.

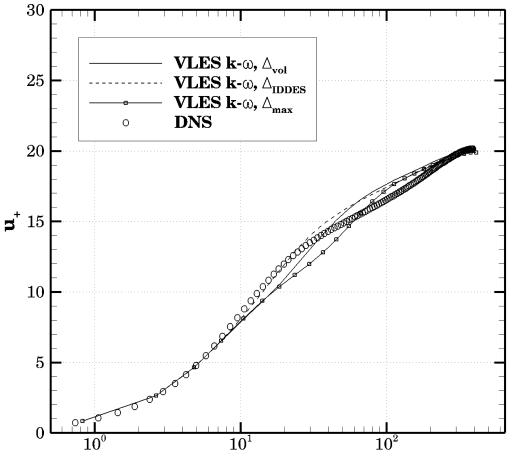

(a) Mean velocity profiles, Grid 1

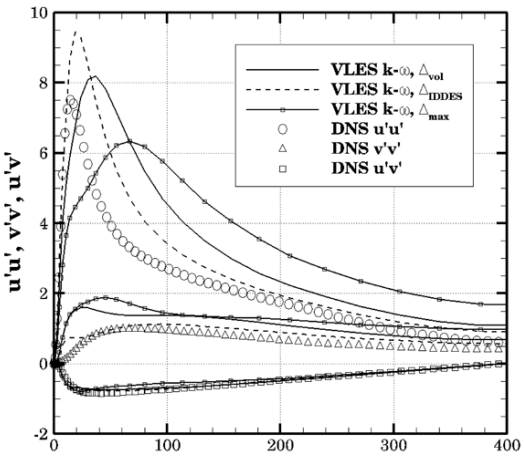

(b) Reynolds sress components, Grid 1

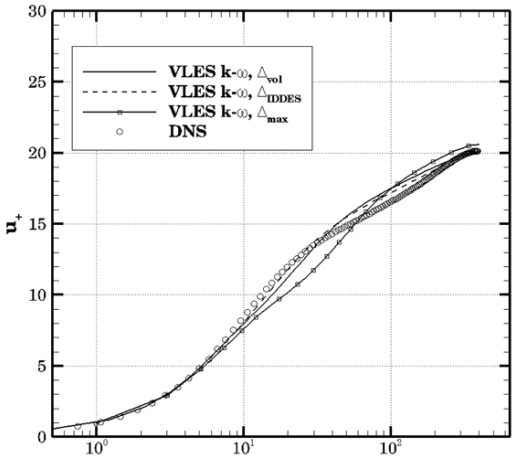

(c) Mean velocity profiles, Grid 2

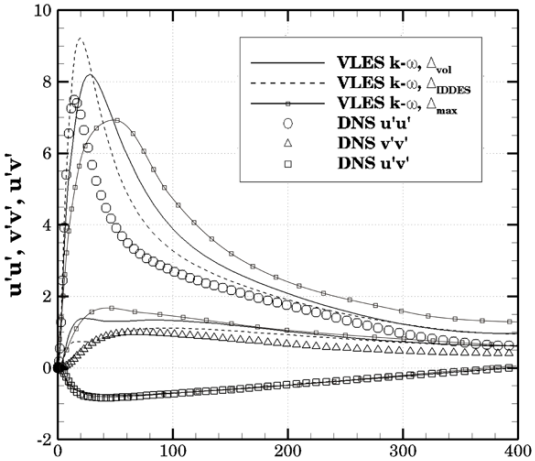

(d) Reynolds sress components, Grid 2

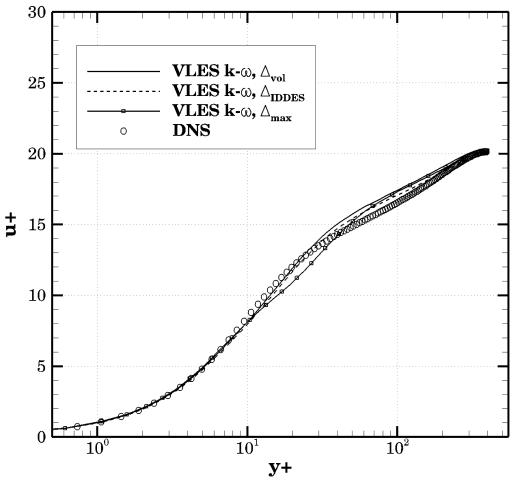

(e) Mean velocity profiles, Grid 3

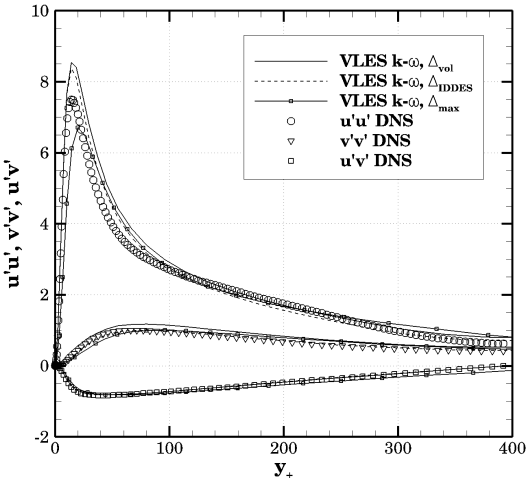

(f) Reynolds sress components, Grid 3

Figure 6.19: Velocity profiles and Reynolds stresses for three different filter width criteria on different grids for channel flow at $Re_\tau = 395$.

In the Reynolds stress components as in the mean-velocity profiles, the influence of the filter width decreases with refinement of the grid (see Figure 6.19, right). As expected, the Reynolds stresses produced by the VLES method with the IDDES criterion are in better agreement with the data from the literature. Already, on the coarse mesh, the position of the peak of the dominant $u'u'$-component is captured better by the IDDES-VLES method than by other formulations of the VLES model. The maximum value of the first Reynolds stress component produced by the VLES with Δ_{IDDES} approaches the DNS data with an increasing number of control volumes, and on Grid 3 the agreement between VLES and DNS data is quite well. The $u'u'$ values obtained by the VLES approach with the maximum criterion demonstrate a significant deviation from the DNS data on the coarse mesh; however, results approach the reference on the mesh with fine resolution.

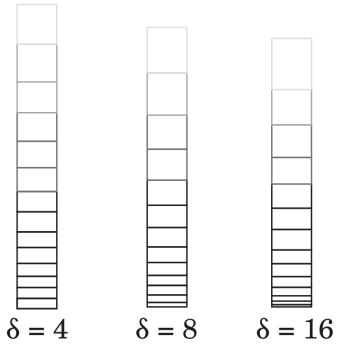

Figure 6.20: Two-dimensional schematic representation of grids with different stretching factors for channel flow at $Re_\tau = 395$.

As can be recognized from Figure 6.21, the filter width criterion has direct impact on the distribution of the F_r function in the channel flow. As expected, the VLES behaves like RANS in the vicinity of the wall, while the LES-like behavior is dominant in the rest of the computational domain. For the IDDES criterion, the RANS-region is shorter. With the $\max$ filter width, on the other hand, a more significant portion of the turbulent structures is modeled. Already on the coarser grid, this behavior leads to better results for the IDDES-VLES model and the mismatch of the $\max$-VLES method.

Additionally an influence of different grid configurations on the results obtained by the VLES model with IDDES and volume criteria was investigated. Grids are distinguished by different stretching factor in the normal direction. A two-dimensional schematic depiction of these grids is presented in Figure 6.20. Here, δ means a ratio of a side length in x- to a side length in y-directions $\delta = \Delta x/\Delta y$.

Results produced by the VLES methods, with different Δ on Grid 1 and Grid 2 with $\delta = 4$, demonstrate a significant deviation from the DNS results, although the IDDES-VLES model yields an improvement of mean velocity profiles in comparison to the standard formulation of the VLES method (Figure 6.22 [a] and [b]). The same tendency can be obtained for other stretching

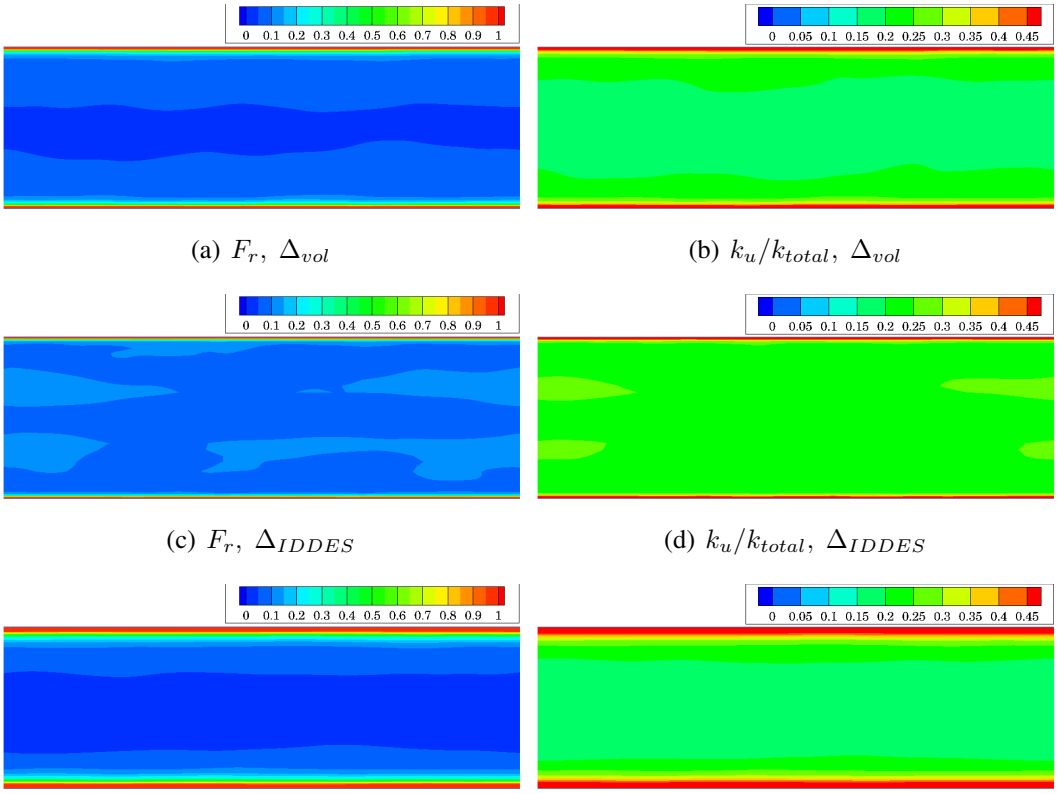

(a) $F_r,\ \Delta_{vol}$ (b) $k_u/k_{total},\ \Delta_{vol}$

(c) $F_r,\ \Delta_{IDDES}$ (d) $k_u/k_{total},\ \Delta_{IDDES}$

(e) $F_r,\ \Delta_{max}$ (f) $k_u/k_{total},\ \Delta_{max}$

Figure 6.21: Resolution control function F_r and modeling ratio k_u/k_{total} for three different filter widths on coarse grid for channel flow at $Re_\tau = 395$.

factors: $\delta = 8$ and $\delta = 16$. The difference between results on the grids with different δ decreases with increase of the stretching factor value and refinement of the mesh resolution. Thus the standard VLES method and the VLES model with IDDES filter width demonstrate very similar results on Grid 2 with $\delta = 16$.

In the present section, it has been shown that the filter width has a significant influence on the results within the VLES model in the case of anisotropic meshes. The influence of Δ decreases with the refinement of the mesh resolution. Thus a modification of the filter width criterion in the formulation of the VLES model leads to a significant improvement in the results already obtained on the coarse grid. Additionally, different grid configurations subdivided by stretching factors have been investigated. The results of the VLES model depend greatly on the mesh quality. In this case, the VLES method with IDDES filter width demonstrate the improvement of the result in comparison to the volume criterion too. Thus the IDDES-VLES approach captures well the mean velocity profiles with the biggest stretching factor $\delta = 4$ and on the mesh with $\delta = 8$ the results confirm the DNS data better than the standard formulation of the VLES model.

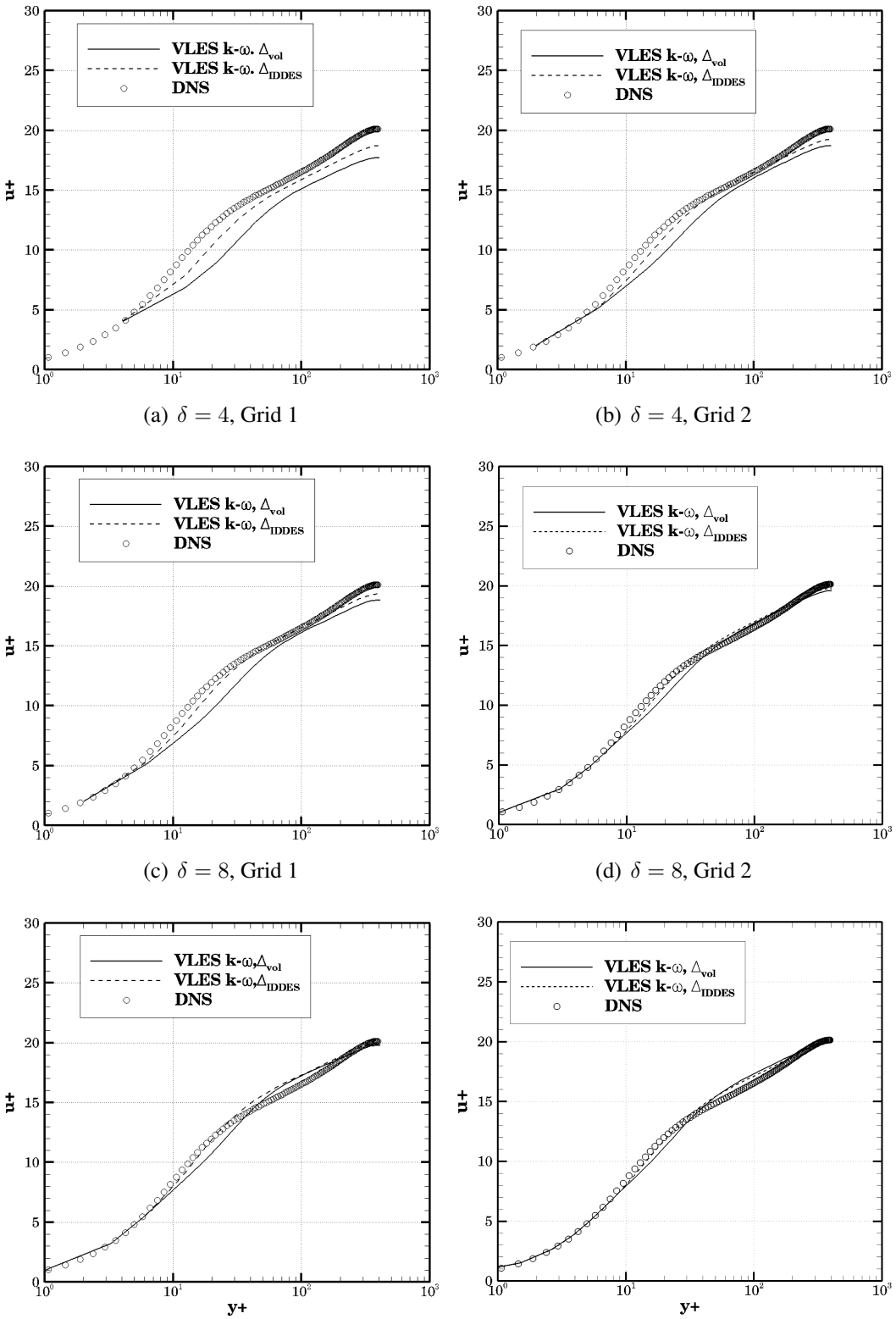

(a) $\delta = 4$, Grid 1

(b) $\delta = 4$, Grid 2

(c) $\delta = 8$, Grid 1

(d) $\delta = 8$, Grid 2

(e) $\delta = 16$, Grid 1

(f) $\delta = 16$, Grid 2

Figure 6.22: Velocity profiles for IDDES and volume filter width criteria on grids with different stretching factor δ for channel flow at $Re = 395$.

7 Very Large Eddy Simulation Model on Moving Grids

In Chapter 6, the VLES approach was validated with the different flow configurations on stationary grids. This hybrid turbulence model demonstrates good results for different kinds of applications and establishes its capability to correctly predict wall-bounded flows and flows with mild and massive separations. The next step in the investigation of this hybrid turbulence model is an examination of the behavior of the VLES approach on moving grids, which plays an essential role in many engineering fields for instance in FSI applications. In such cases, the problems become much more demanding in terms of computational cost [22]. Therefore a reduction of computational time provided by the VLES model is especially important and promising in this context.

The calculation with moving structures is an additional challenge for the VLES model. As remarked in Section 3.3, the VLES model switches seamlessly between two modes depending on the numerical grid resolution, which in this context changes in each step due to grid motion. For the VLES approach, the grid movement results in a change of the location of the interface between DNS mode and RANS mode, having a direct impact on the overall results. Moreover, the movement of the grid can cause a change of the non-dimensional wall distance, which should fulfill the condition $y^+ \approx 1$. Therefore, the behavior of the VLES approach in this context should be investigated in detail to determine any difficulties that might arise in the case of moving structures, before the simulation of the FSI cases can proceed.

The focus of this chapter lies on the investigation of $k-\varepsilon$ and $\zeta-f$ VLES models in the context of moving grids. Firstly, these techniques are applied to simulate the flow over a forced oscillating circular cylinder at $Re = 10,000$. This type of flow configuration occurs in many industrial applications with vortex-induced vibrations, for instance in piles of offshore platforms. Section 7.2 investigated a flow over a tandem of an oscillating and a static asymmetric SD7003 airfoil, a so-called tandem-airfoil or dragonfly flight, at $Re = 30,000$. This type of flow plays an essential role in the design of micro aerial vehicles. This configuration initially was introduced by Schmidt [140] to extract the energy of vortices from the upstream foil, the so-called wave generator, and use it to generate thrust on the static hindfoil, the so-called propeller.

7.1 Flow over oscillating cylinder

At the beginning, the flow past a rigid oscillating circular cylinder is investigated. The Reynolds number $Re = 10,000$ is based on the inflow velocity U_0 and the cylinder diameter D. This flow

configuration has been experimentally investigated by Gopalkrishnan [55]. The DNS results for this flow are reported in Dong and Karniadakis [36]. The results of the DNS calculation are in good agreement with the experimental data; the sharp change of the flow quantities as lift and drag coefficients C_L and C_D at oscillation frequency close to the Strouhal frequency ($St \approx 0.2$) is captured well. However, some deviations occur at low frequencies in the values for C_L. Some RANS results are also available in the literature, for example, in [158] and [72]. These works demonstrate that the RANS models in their classical formulations ($k-\varepsilon$ and $k-\omega$ as well as the one-equation Spalart-Allmaras RANS model) show weaknesses in the prediction of this type of flow. Two equation models are able to capture the critical area, but values for the drag coefficient obtained with the classical $k-\varepsilon$ model are massively underpredicted, while the lift coefficients achieved with the $k-\omega$ approach are overpredicted at low frequencies. Values obtained by the Spalart-Allmaras model do not show the obvious "jump" in C_L and C_D coefficients; however, the C_L and C_D values approach the experimental data on low and high frequencies. The reason for this issue with the RANS model is high damping caused by high turbulent viscosity and as a result a relatively low intensity of the turbulence activity in the separated region, as mentioned in Section 6.1.1.

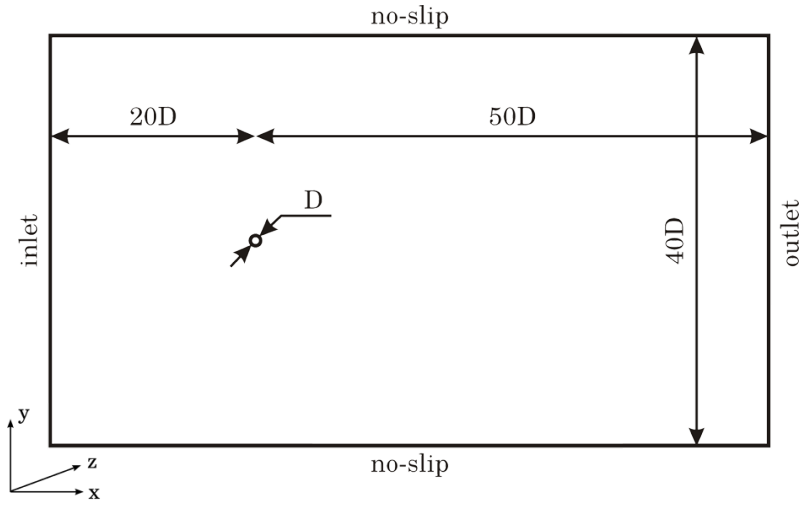

Figure 7.1: Computational domain for flow over oscillating circular cylinder.

In the present work, the computational domain is constructed in accordance with the simulation of Dong and Karniadakis [36] and extends $70D$ in x-direction, $40D$ in y-direction and πD in z-direction. In the initial position, the cylinder is placed symmetrically at the channel, midhight. The domain is covered with a block-structured grid with an O-grid block around the cylinder (see Figure 7.2). The movement of the grid realized with linear interpolation techniques (briefly outlined in Section 4.6) occurs within the O-block. The mesh in the rest of the computational domain stays unchanged, leading to a reduction of computational effort. The grid contains approximately 1.1 million control volumes with 55 cells in z-direction. The first grid cell corresponds to the condition for the non-dimensional normal distance to the wall $y_+ \approx 1$ at the start position of the cylinder. In the current simulation, the convective terms in the Navier-Stokes

equations are discretized using the second-order CDS scheme for the $k-\varepsilon$ VLES model and the flux-blending-approximation scheme with the coefficient $\alpha = 0.8$ for the $\zeta - f$ VLES model. For the turbulence quantities the Gamma scheme [75] is applied. The temporal approximation is carried out with the three-point-backward-method with a second order of accuracy (SOFI).

The following equation describes the cylinders displacement in the cross flow direction:

$$y = Y_0 \sin\left(2\pi f_0 t\right), \tag{7.1}$$

where Y_0 is the cylinder displacement amplitude ($Y_0/D = 0.3$) and f_0 is the oscillation frequency of the cylinder.

To cover the abrupt change in drag and lift coefficients five different oscillating frequencies are considered in this simulation: $f_0 D/U_0 = 0.14$, 0.17, 0.19, 0.21 and 0.25.

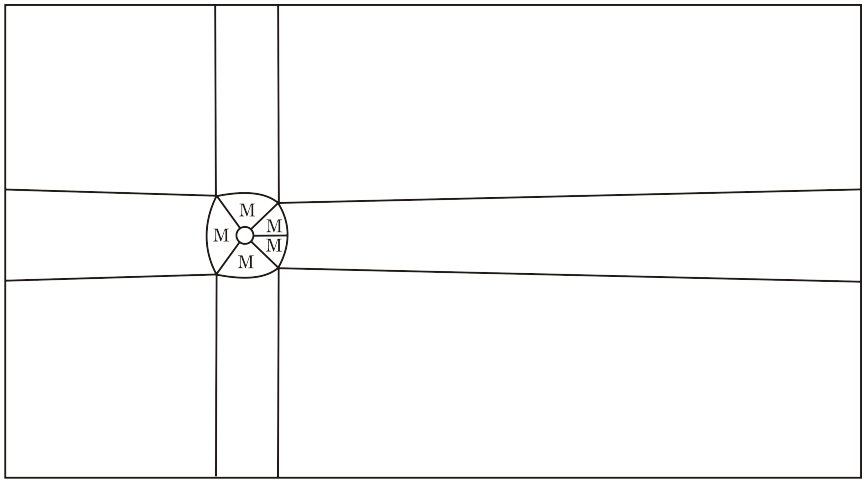

Figure 7.2: Block structure of computational domain for flow over oscillating cylinder; M indicates moving block.

The lift and drag coefficients obtained with the $k-\varepsilon$ VLES model as a function of the dimensionless frequency are presented in Figure 7.3, together with DNS and experimental data. The $k-\varepsilon$ VLES approach captures quite accurately the abrupt change in the lift coefficient around the vortex-shedding frequency. However, this model underpredicts the C_L values for higher oscillation frequencies ($f_r > 0.17$), while the value at the low frequency ($f_r = 0.14$) shows quite good agreement with the experimental data from Gopalkrishnan [55]. This finding contrasts the DNS simulation from [36], where the lift coefficient values on the low oscillation frequencies are overpredicted and are captured well for $f_r > 0.17$.

Since on the static grid the modification of the filter width in the formulation of the VLES model demonstrated direct influence on the results, the impact of the IDDES criterion is investigated in the context of moving grids. For this reason, the simulation with the $k-\varepsilon$ IDDES-VLES model was carried out on four different frequencies. The results are illustrated in Figure 7.3 (a). In the case of a moving mesh, the modified VLES model yields no significant improvement in

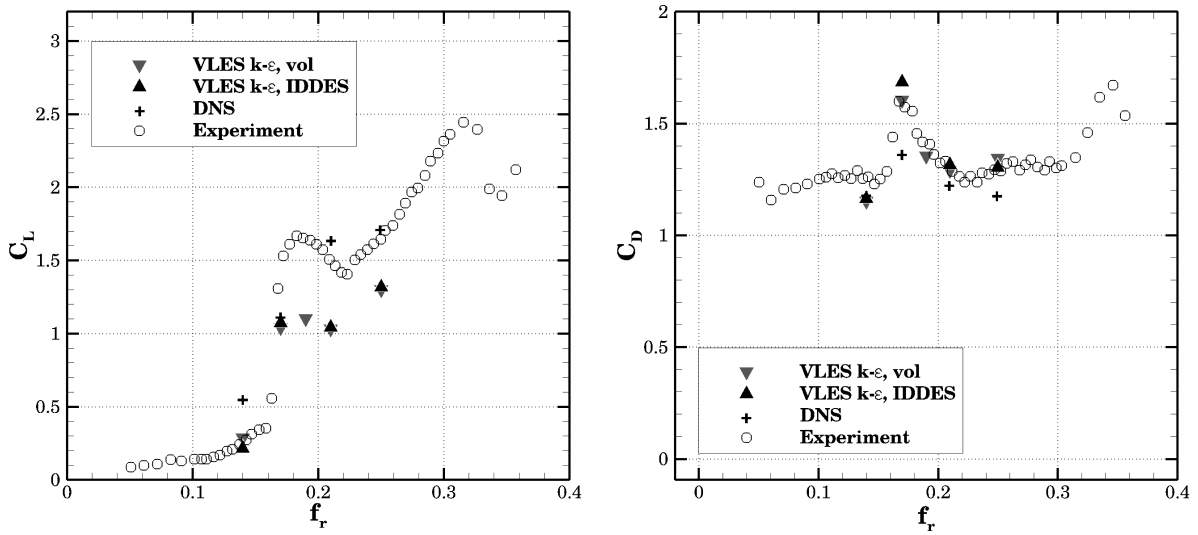

(a) Lift coefficients

(b) Drag coefficients

Figure 7.3: Lift and drag coefficients as a function of non-dimensional frequency for $k-\varepsilon$ VLES model with different filter widths for flow over oscillating cylinder.

comparison to the standard $k-\varepsilon$ VLES. One of the reasons may be the sufficient refinement of the used mesh. As reported in Section 6.2, the influence of the filter width criterion decreases with the increase of the number of control volumes. Moreover, a significant improvement of the results is obtained by the $k-\omega$ VLES model, which is not investigated in the context of moving grids, because this approach in its classical formulation has demonstrated the biggest deviation from the reference data on the stationary grids.

In Figure 7.3 (b), the drag coefficients produced by the standard $k-\varepsilon$ VLES model and IDDES $k-\varepsilon$ VLES model are compared to the experimental values and DNS data. The agreement between the VLES models and the reference data is reasonable. The standard $k-\varepsilon$ VLES approach slightly underpredicts the drag coefficient at low frequencies, but for higher frequencies the prediction is fairly accurate. As in the case of the lift coefficient, the differences between the results obtained with the different filter widths is insignificant. The drag coefficient values produced by the $k-\varepsilon$ VLES model are in better agreement with the experimental data than the DNS results.

The results achieved by the $\zeta-f$ VLES model show a behavior similar to that seen in the $k-\varepsilon$ VLES results (see Figure 7.4). The lift coefficient is underpredicted for higher frequencies and captured well for the low frequencies ($f_r = 0.14$). The critical area is shifted insignificantly in comparison to the $k-\varepsilon$ VLES model, and therefore the C_L value is underpredicted at $f_r = 0.17$. As for the $k-\varepsilon$ VLES approach, the drag coefficient is in very good agreement with the experimental data, especially for the higher oscillation frequencies. The movement of the cylinder can cause a change of y^+, such that the condition $y^+ \approx 1$ might no more fulfilled in

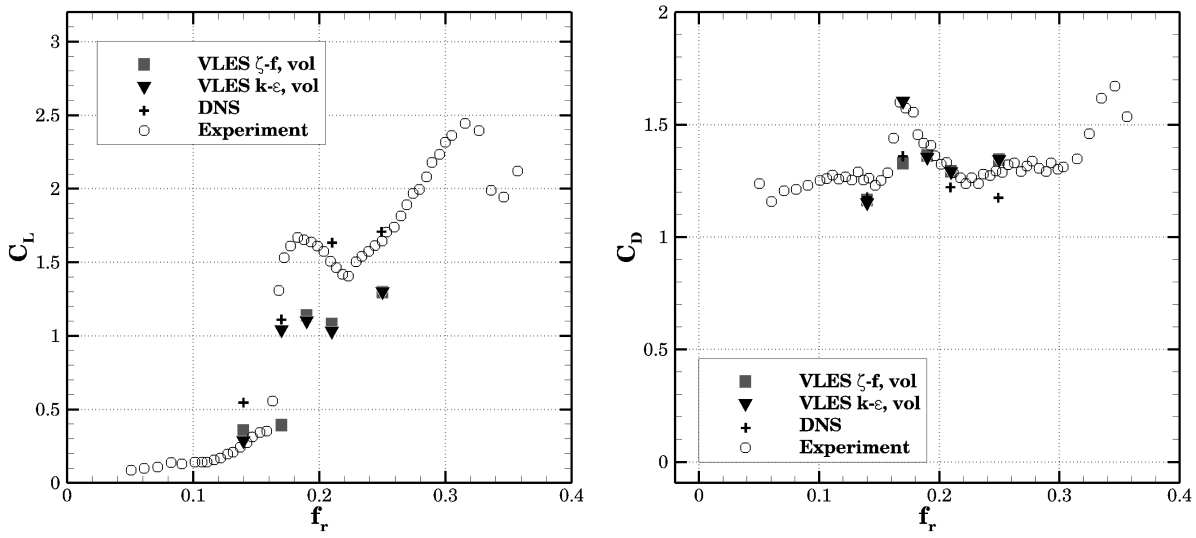

(a) Lift coefficients

(b) Drag coefficients

Figure 7.4: Lift and drag coefficients as a function of non-dimensional frequency for $\zeta - f$ and $k - \varepsilon$ VLES model for flow over oscillating cylinder.

each time step. This change is responsible for the inaccurate calculation of the velocities in the near-cylinder region and as a result, the underprediction of the C_L values, which are more sensitive to the numerical grid resolution than the C_D values. Another possible reason for the underprediction of the coefficients is an erroneous calculation of F_r and as a result an incorrect switching between the two basic modes in the VLES simulation. To exclude this course, the resolution control function is investigated in the following paragraph.

The distribution of the resolution control function is a significant issue in the simulations with theVLES model. It demonstrates the correctness of the performance of this hybrid turbulent approach. An incorrect calculation of F_r can lead to wrong positions of RANS and DNS modes and in consequence to incorrect results. Especially in the case of moving structures, where the mesh changes with each time step, the risk of incorrect calculation of F_r is high. The F_r function and the modeling ratio k_u/k_{total} produced by the $k - \varepsilon$ VLES model are presented in Figure 7.5 for the non-dimensional frequency $f_0 = 0.21$, since the behavior of F_r is similar for all f_0. As can be recognized from these figures, the RANS mode dominates in the region close to the cylinder interface ($F_r \longrightarrow 0$), where the wall-boundary conditions are applied. However, the RANS region is active only near the top surface of the cylinder, when the cylinder is located over the zero-line (starting position, $y = 0$) and near the bottom surface in the opposite case (Figure 7.5, [b], [d], [f]). Such a distribution of the F_r function can lead to VLES results that deviate from the reference data. It is desirable that in the wake region, the VLES approach behaves mostly in a LES-like manner (Figure 7.5 [e], [f]), where the major part of turbulent structures is resolved and the other part is modeled. This distribution corresponds to the idea of hybrid models, where

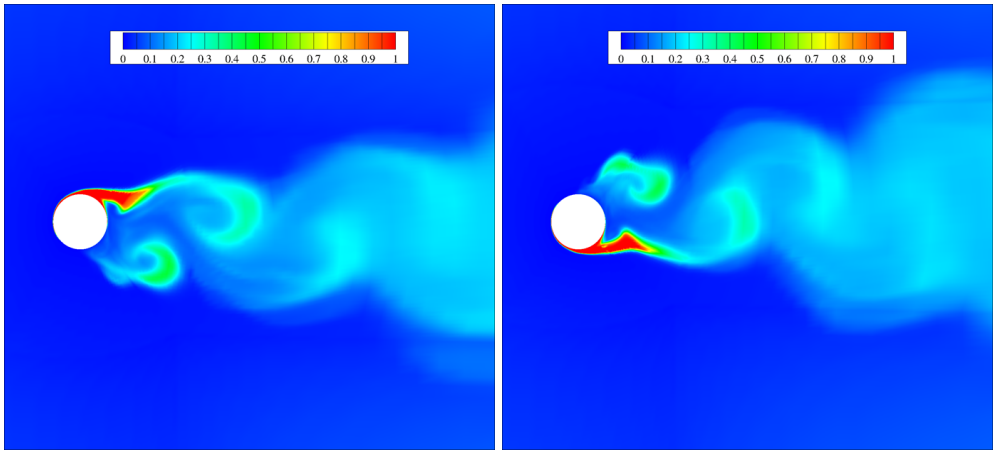

(a) F_r, top position of cylinder

(b) F_r, bottom position of cylinder

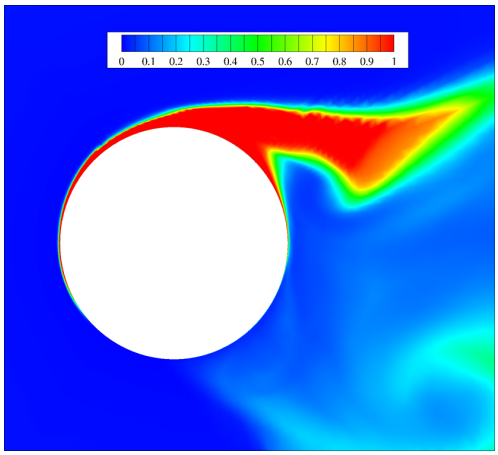

(c) F_r, zoom view, top position of cylinder

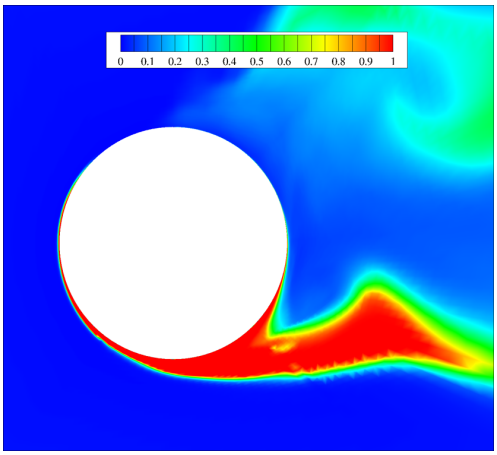

(d) F_r, zoom view, bottom position of cylinder

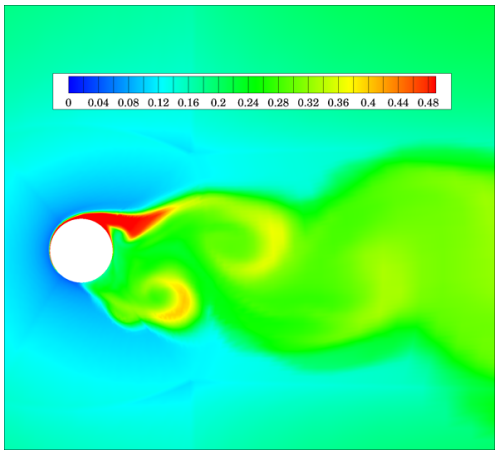

(e) k_u/k_{total}, top position of cylinder

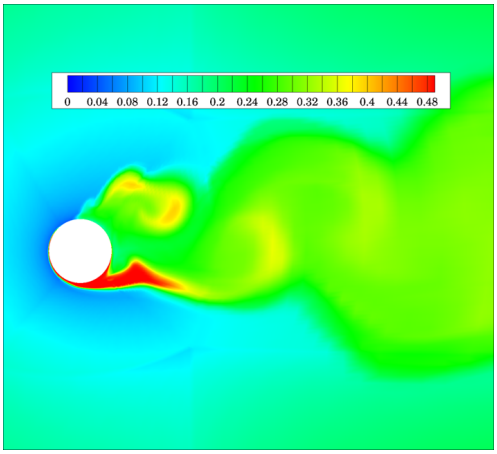

(f) k_u/k_{total}, bottom position of cylinder

Figure 7.5: Resolution control function F_r and modeling ratio k_u/k_{total} for $k-\varepsilon$ VLES model at $f_0 = 0.21$ for different cylinder positions for flow over oscillating cylinder.

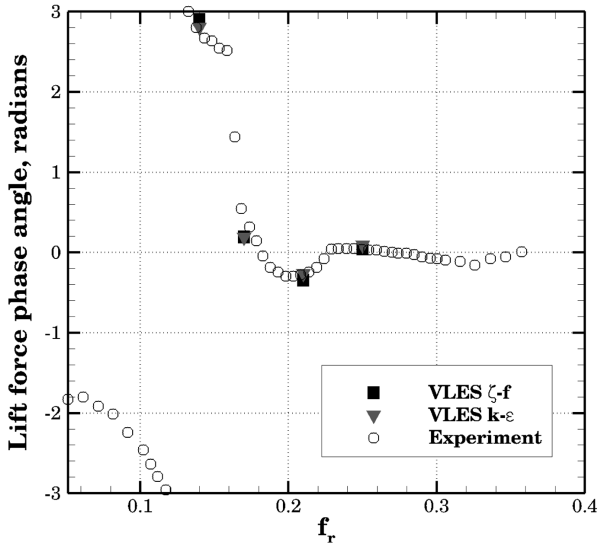

Figure 7.6: Phase angle between lift force and cylinder displacement obtained by $k-\varepsilon$ VLES and $\zeta - f$ VLES model for flow over oscillating cylinder.

the large separation regions with the domination of anisotropic effects are calculated with the LES models, because of the weakness of RANS approaches in simulation of such flow behavior (see Chapters 3 and 6).

The displacement of the cylinder together with the time history of the lift coefficient obtained by the $\zeta - f$ VLES model for four different frequencies before and after the abrupt change of lift and drag forces is plotted in Figure 7.7. These plots illustrate the increase of the lift coefficient frequency by increase of the non-dimensional frequency f_0 as already depicted in Figure 7.4 (a). It is well recognized that lift coefficients on the low ($f_0 < 0.17$) and high frequencies ($f_0 \geq 0.7$) (before and after the "jump") have a different behavior. The same effect is reported in [23] and confirmed by the LES simulation in [82], where this flow is investigated for a lower Reynolds number and a higher amplitude ratio, Y_0/D. The detailed presentation of this behavior can be found in Figure 7.6, where the phase angle between the lift force and displacement of the cylinder is depicted for different non-dimensional frequencies. This effect is denoted as the low-frequency state before transition and the high-frequency state after transition. For the high-frequency state ($f_0 \geq 0.17$), the maximum of the lift force is obtained when the cylinder approaches the top position in y-direction, while for the low f_0 this position is not clearly defined.

In simulations of turbulent phenomena, it is important to reproduce the three-dimensionality of the turbulent flows. The VLES approach is able to capture three-dimensional eddy structures in the flow over the oscillating cylinder and yields the inhomogeneous flow feature. In contrast, the URANS simulation demonstrates a two-dimensional flow behavior. To illustrate this effect, Figure 7.8 presents the comparison of the velocity fields in three different positions in z-direction for the $k-\varepsilon$ URANS and the $k-\varepsilon$ VLES models. The velocity field produced by the URANS simulation is equal in all three positions, while the VLES results produce an inhomogeneous

velocity field.

The present section has shown that the $\zeta - f$ and the $k - \varepsilon$ VLES model can predict the abrupt changes in drag and lift coefficients around the crucial frequencies in the flow over the circular cylinder. The values for the drag coefficients correspond closely to the reference data, while the values of the lift coefficients are underpredicted on higher frequencies for both VLES models. The VLES method is able to predict the three-dimensional character of the flow in contrast to the RANS simulations. Moreover the difference in the behavior of the flow over the cylinder before

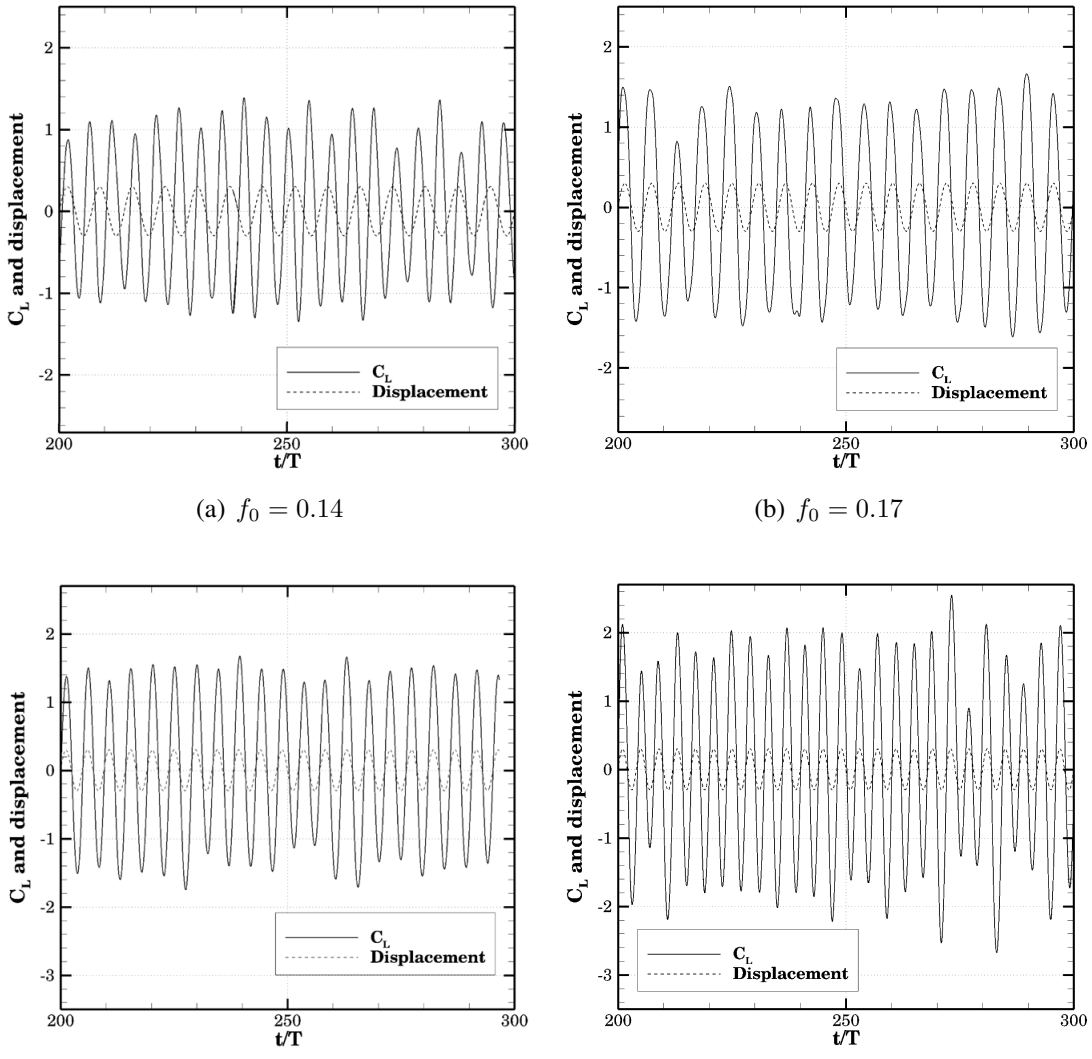

(a) $f_0 = 0.14$ (b) $f_0 = 0.17$

(c) $f_0 = 0.21$ (d) $f_0 = 0.25$

Figure 7.7: Displacement of cylinder and time history of lift coefficient as function of non-dimensional frequency f_0 for $\zeta - f$ VLES model flow over the oscillating cylinder.

the transition and after the transition are captured very well.

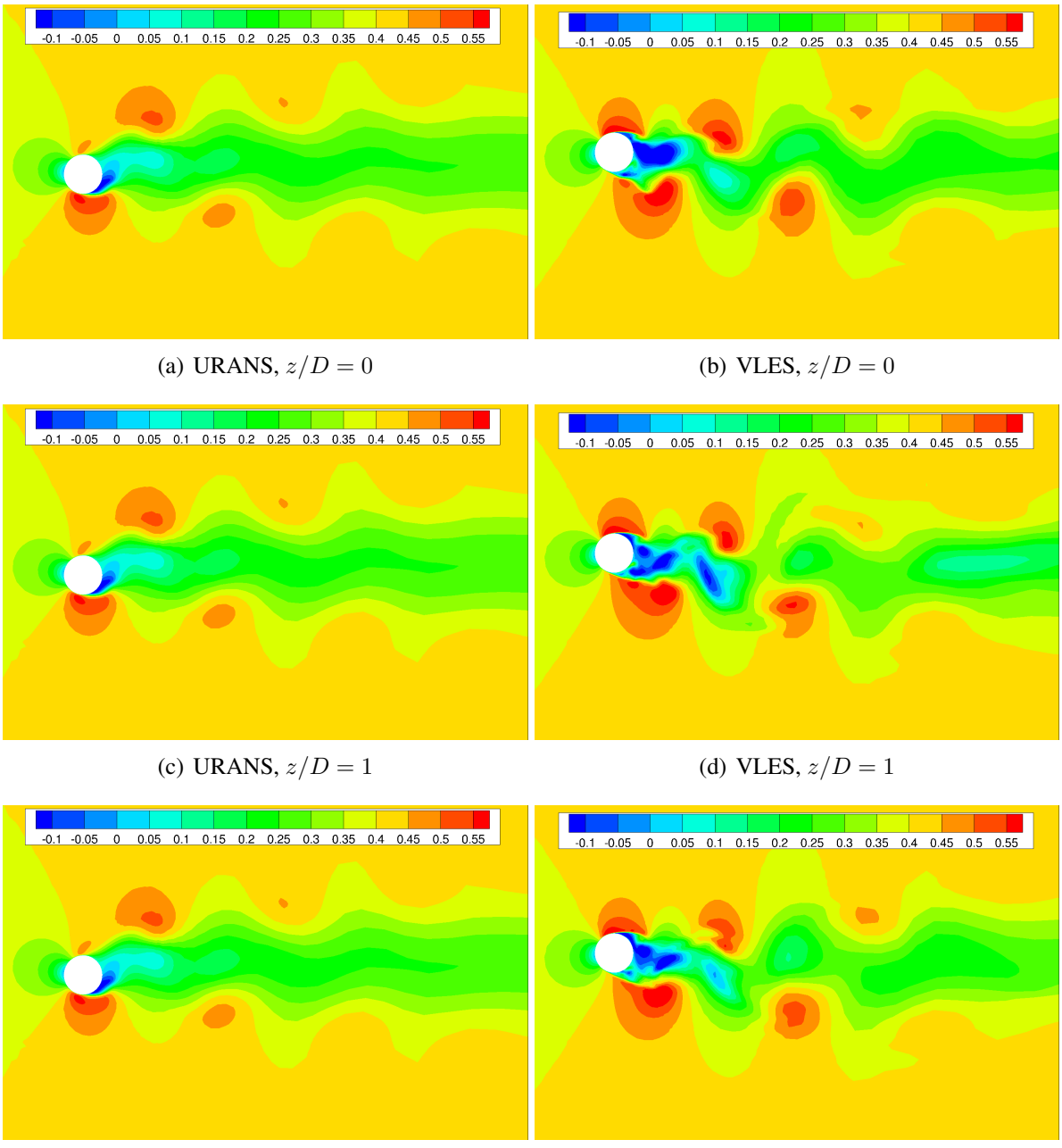

(a) URANS, $z/D = 0$ (b) VLES, $z/D = 0$

(c) URANS, $z/D = 1$ (d) VLES, $z/D = 1$

(e) URANS, $z/D = 2$ (f) VLES, $z/D = 2$

Figure 7.8: Velocity field on different positions in z-direction for $k - \varepsilon$ VLES and $k - \varepsilon$ URANS model for flow over oscillating cylinder.

7.2 Flow over tandem of airfoils

This section focuses on the investigation of a flow over a tandem of an oscillating and a static asymmetric SD7003 airfoil at $Re = 30,000$ based on the chord length c and inflow velocity U_0. This simulation draws on the experiment from Rival et al. [130]. They investigated the optimal vortex formation by vortex dynamics to better understand thrust production and power reduction. Rival et al. tested many kinds of different configurations for these airfoils, such as the static airfoil's unloaded position (when the hindfoil generates negligible lift) or the loaded position (when the hindfoil produces considerable lift). In the current work, the experiment with the loaded position was chosen, where the leading airfoil (forefoil) with the geometric angle of attack of $\alpha_F = 8°$ moves in the y-direction and generates a wake of vortices through a plunging motion, while the trailing airfoil (hindfoil) is fixed at a position $x/c = 2$ and a specified angle of attack $\alpha_H = 0°$.

A harmonic motion of the forefoil is described with the time-dependent plunge position h_t, which depends on a plunge amplitude $h_0 = 0.5c$ and the period frequency f_t:

$$h_t = h_0 \cos(2\pi f_t t) . \tag{7.2}$$

The computational domain is assumed from the work of Rival [132] and amounts to $x = 7.25c$ before the forefoil and $x = 8.15c$ after the hindfoil in x-direction. The height of the domain is $y = 8c$, and the length of the domain in z-direction is $z = \pi c$. The simulation is performed on a block-structured mesh with approximately one million grid cells with 32 control volumes in z-direction. The grid is constructed with a C-mesh around the leading airfoil. As in the first test case in this chapter the movement of the mesh is performed only in blocks around the moving airfoil (see Figure 7.9, gray area), leading to a reduction of computation effort in each time step, since only the deformation of the grid in these blocks must be calculated.

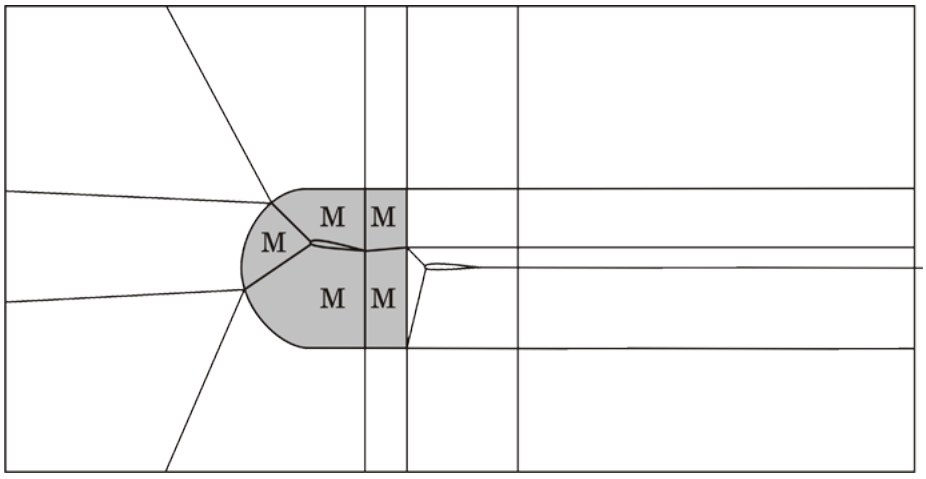

Figure 7.9: Block structure in computational domain for flow over tandem of airfoils; M indicates a moving block.

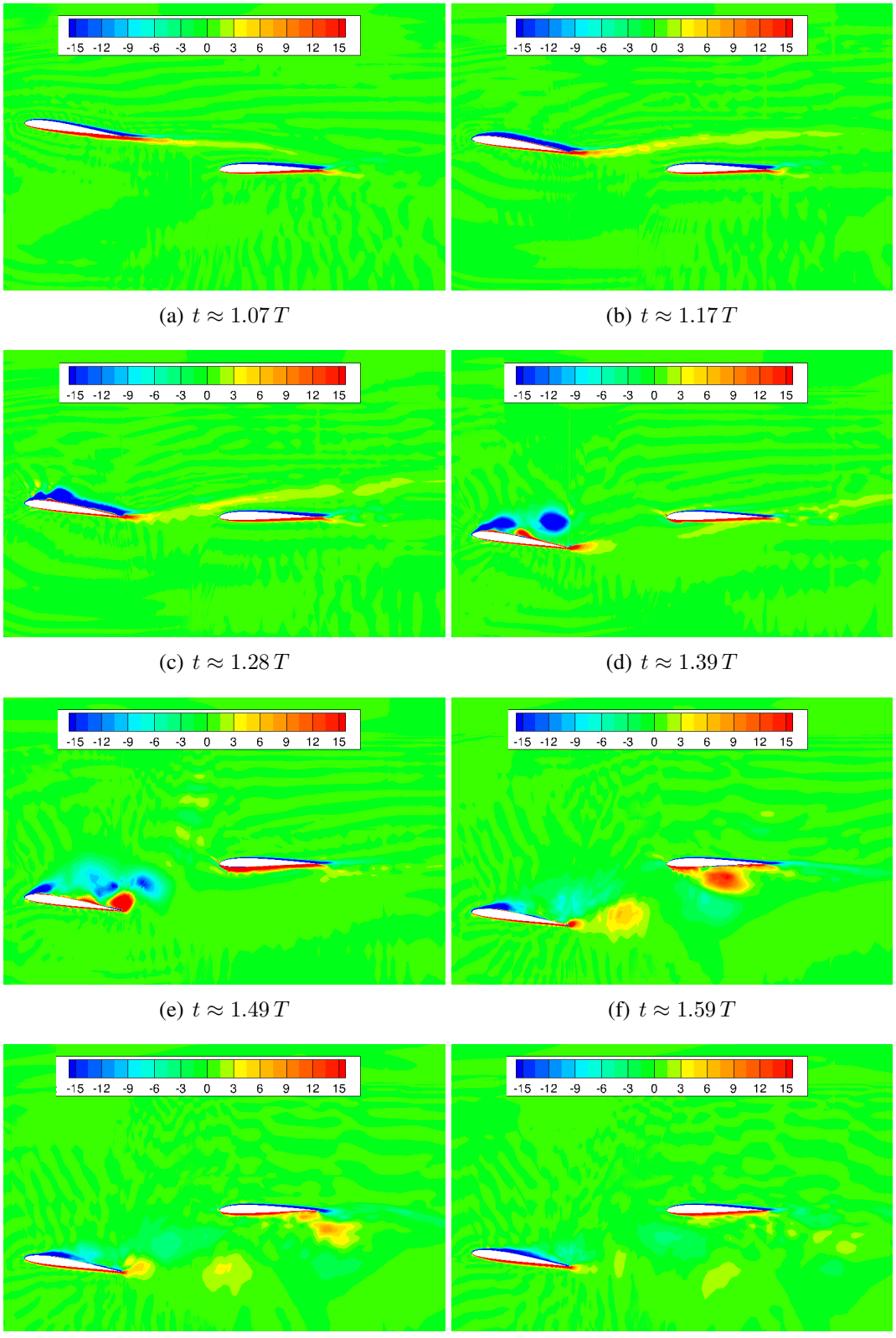

(a) $t \approx 1.07\,T$ (b) $t \approx 1.17\,T$

(c) $t \approx 1.28\,T$ (d) $t \approx 1.39\,T$

(e) $t \approx 1.49\,T$ (f) $t \approx 1.59\,T$

(g) $t \approx 1.49\,T$ (h) $t \approx 1.59\,T$

Figure 7.10: Blade-vortex interaction obtained by $k - \varepsilon$ VLES model for flow over tandem of airfoils.

In the present simulation the convective term in the Navier-Stokes equations is discretized with the CDS method for the $k-\varepsilon$ VLES and with the flux-blending approximation with $\alpha = 0.8$ for the $\zeta - f$ VLES model. For the turbulent transport equations, the QUICK and GAMMA schemes are applied for the $k-\varepsilon$ VLES and $\zeta - f$ VLES models accordingly. The unsteady term is approximated with the SOFI method.

From the experiments of Rival et al. [131], the lift and drag coefficients C_L and C_D are available as reference data. It is important to remark, that in the experiments individual forces from each airfoil have not been separated, due to the experiments' configuration. Additionally the shape of the force curve is distorted in time (shift by $t/T = 0.25$), since the control-volume analyses were used in the evaluation of the experiment. These factors are considered in the presentation of the simulation results.

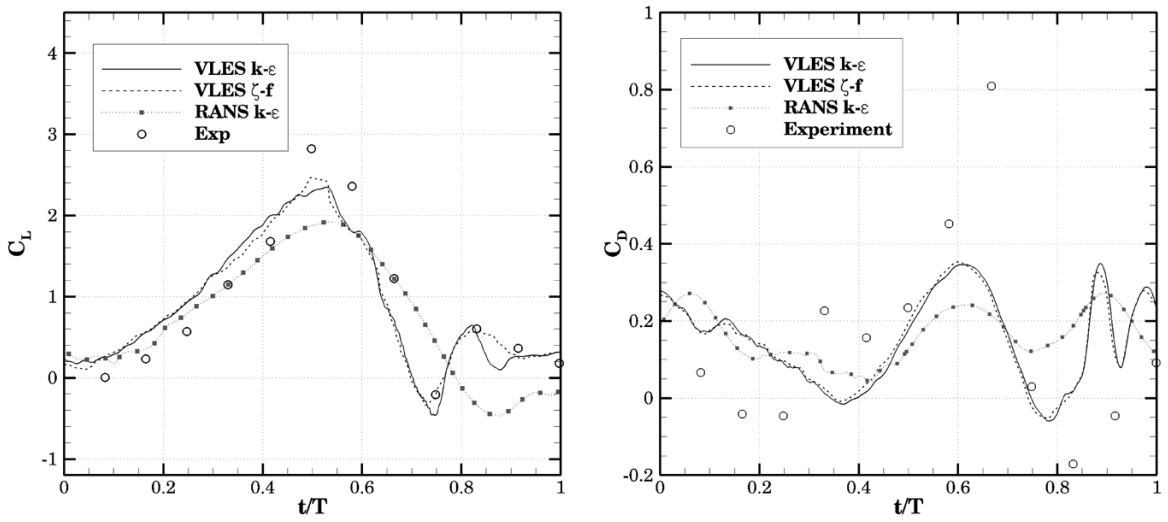

(a) Lift coefficients

(b) Drag coefficients

Figure 7.11: Lift and drag coefficients as a function of non-dimensional frequency for $k-\varepsilon$ and $\zeta - f$ VLES model for flow over tandem of airfoils.

Figure 7.10 demonstrates the detailed behavior of the flow over the tandem of airfoils by means of the dimensionless z-vorticity ($\omega_z\, c/U_0$) for eight different positions of the moving airfoil. The evolution of the flow clearly identifies leading-edge vortex (LEV) and trailing-edge vortex (TEV) separations from the forefoil, which induce flow separation from the lower surface of the hindfoil and the generation of a wake region behind the stationary airfoil. The effect of the vortex-induced separation is clearly recognized in this configuration.

Before the airfoil reaches its position corresponding to a quarter of the movement period (image [b]), the counter-clockwise vortex generates an upwash at the leading edge of the forefoil. This induces a boundary-layer separation from the upper airfoil surface (image (c)). The generation of the clockwise-oriented TEV is recognized after the forefoil reaches a quarter of the movement

period $t > T/4$ (image [c]). Before the moving airfoil is located in a position corresponding to half of the period $t = T/2$, the vortex separates from the trailing edge of the forefoil. This induces the separation of the boundary-layer on the lower surface of the hindfoil (image [e]).

Figure 7.11 (a) presents the lift coefficients C_L observed in the simulation with the $k-\varepsilon$ and the $\zeta - f$ VLES models over non-dimensional time, in comparison to the reference data and to the results from the $k-\varepsilon$ URANS simulation. The distribution of C_L is predicted well with the VLES models. Both hybrid approaches capture the peak of the lift coefficient at $t/T \approx 0.5$ and the minimum value at $t/T \approx 0.75$, in accordance with the experiment. The URANS simulation results show significant deviation from these values. The positions of the minimum and maximum of the lift coefficient are shifted, and the minimum and maximum values of C_L are significantly underpredicted.

Concerning the prediction of the drag coefficient C_D, the VLES models show deviation from the experimental data, as shown in Figure 7.11 (b). The clear peak can not be identified in the simulation, while the experimental data demonstrate the clear maximum of the drag coefficient in the position $t/T \approx 0.65$. However, the tendency in the distribution of the drag coefficient is captured well by the VLES models. In the beginning of the period C_D decreases and takes on negative values, so the position of minimum drag coefficient in this region is shifted by the numerical simulation. Then, the drag coefficient increases and reaches maximum. In accordance with the experiment it happens in $t/T \approx 0.68$, while the VLES model predicts the maximum value at $t/T = 0.63$. After this position, C_D decreases again and takes on negative values, as captured by the VLES simulation.

Since this configuration of a tandem flow is not widely investigated experimentally, additional experiments are required to examine the sensitivity of the experimental values to the configuration of the domain, boundary conditions and other flow parameters. Additionally, this flow can be investigated numerically with other turbulence models to show the difficulties of the different approaches predicting this type of flow and highlight the delicate points of this flow configuration.

As in the case of the oscillating cylinder, the VLES approach demonstrates the ability to simulate the flows with moving structures. The character of the flow is captured well for both test cases on the moving grid. The results for the flow parameters such as lift and drag coefficients are predicted with reasonable reliability. The deviations occur in the first case in the calculation of the lift coefficient, while in the second test case, the drag coefficient distribution cannot be captured in accordance with the experiment. A refinement of the grid in the second case can lead to an improvement of results, due to the fact, that the drag in this flow configuration depends strongly on the shear stress τ_w, which is sensitive to the mesh resolution. It was not investigated in the framework of this work, because the goal is to test the VLES model on the coarse meshes that are suitable for the URANS simulations. It is important to notice that the URANS models demonstrate weaknesses in the prediction of both investigated flow configurations. Another possible reason for the difference between VLES results and the reference data is the deformation of the mesh during the calculation. The required condition for the y^+ is not fulfilled during the whole calculation. The testing of adaptive meshes or the deformation of the mesh without the changing of the non-dimensional wall distance of the first grid cell seems promising.

8 Hybrid turbulence methods in the context of fluid-structure interaction (FSI)

In the previous two chapters the hybrid VLES model with different underlying RANS models demonstrated good results for stationary as well as for moving grids. The last step in the investigation of the VLES model in the present work is an examination of this hybrid approach in the context of a fluid-structure coupling. For this goal, two FSI test cases are investigated, denoted as *FSI-PfS-1a* and *FSI-PfS-2a*. Both configurations consist of a flexible thin structure attached to a fixed rigid circular cylinder. These simulations are based on the experiments from De Nayer et al. [31] and Kalmbach and Breuer [80], respectively. These measurements have been proposed specifically to set up a simple benchmark for the validation of FSI codes, and they have been validated with LES models in works of De Nayer et al. [31] and De Nayer and Breuer [30]. The Reynolds number $Re = 30,470$, chosen for both experiments, ensures the sub-critical regime of the flow, where the boundary layers on a cylinder stay laminar, while in the free shear layers the transition takes place, resulting in the development of three-dimensional structures of different sizes. For such flows, the application of hybrid models is promising, as they are able to capture large and small turbulent vortices on a coarse mesh, in contrast to the LES simulation. In this chapter, the VLES results are compared to the experimental data and to the results obtained with other turbulence modeling methods (LES, DDES and URANS).

8.1 FSI-PfS-1a test case

The first FSI test case, denoted as FSI-PfS-1a, is based on the experiment performed by De Nayer et al. [31]. The test case consists of a flexible rubber sheet with a thickness of $h_s = 0.0021\,\mathrm{m}$ and length of $l_s = 0.060\,\mathrm{m}$, attached to a non-rotating circular cylinder. The Reynolds number, $Re = 30,470$, is based on the cylinder diameter ($D = 0.022\,\mathrm{m}$) and the inflow velocity ($U_0 = 1.385\,\mathrm{m/s}$). As a flexible thin structure, a rubber sheet ($\rho = 1.360\,\mathrm{kg/m^3}$) is chosen. For this material model, Young's modulus $E = 16\,\mathrm{MPa}$ and Poisson's ratio $\nu_P = 0.48$ are defined. The cylinder with the sheet is placed inside a vertical channel filled with a fluid ($\rho = 1.000\,\mathrm{kg/m^3}$ and $\mu = 1.0 \times 10^{-3}$ Pa s). The length of the channel is $L_x = 0.338\,\mathrm{m}$; the height of the channel is $L_y = 0.24\,\mathrm{m}$; and the width is $L_z = 0.18\,\mathrm{m}$ (see Figure 8.1). The gravitational acceleration g points in x-direction. Main geometry, flow and structure parameters are listed in Table 8.1.

For the current test case, a block-structured mesh with 1.7 million grid cells was designed. The mesh contains 32 control volumes in z-direction. The grid's block structure is demonstrated in

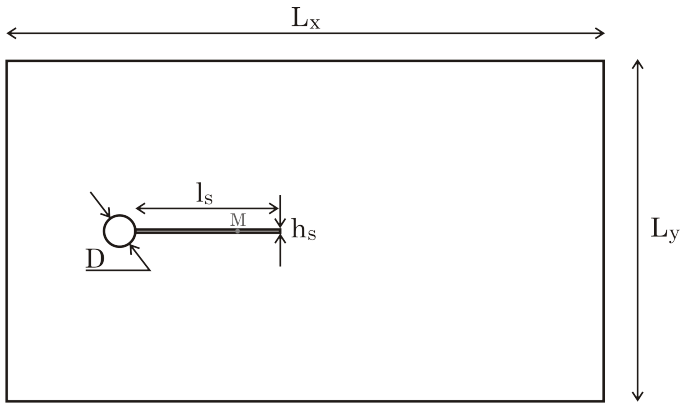

Figure 8.1: Computational domain for the FSI-PfS-1a test case.

Figure 8.2. Since Ali [1] has been proved that the application of the 20-node element for spatial discretization instead of 8-node yields no significant advantages, but leads to a 50% increase of computational time, the structural mesh in the present work is chosen to consist of 30×1 eight node linear brick elements (with enhanced strain formulation).

In the fluid part, the wall boundary conditions are applied on the surface of the cylinder and on the sheet. In accordance to the simulation presented in [31], the symmetry boundary conditions are imposed on the top and bottom walls. In the fluid solver for the discretization of the convective term the hybrid blending approach between the CDS and GAMMA schemes is applied. The time discretization is proceeded with the second-order SOFI method, while in the structural part of the problem the Newmark method is applied to advance the solution in time (for details see [9]). For the coupling between the structure and fluid solvers, a 0^{th}-order force extrapolation with an under-relaxation parameter for the structure distortions $\omega_{FSI} = 0.3$ is used. With this parameter, the code requires about eight coupling iterations to fulfill the convergence criteria for the structural distortion, which is set to $\varepsilon_{FSI} < 1 \times 10^{-9}$ in accordance with LES investigations [31]. The simulation involves about 30 swiveling cycles of the flexible structure after the initial phase.

For an investigation of the movement of the sheet the averaged y-displacement ($U_y^* = U_y/D$) at point M (see Figure 8.1) over the phase angle is plotted in Figure 8.3. The URANS and DDES results in this test case are taken from [1] (in the following URANS is denoted as RANS). Simulation results of different turbulence modeling techniques demonstrate good coincidence with the experimental data for the phase-averaged displacement. Deviations occur in the prediction of extrema for all turbulence models. The $\zeta - f$ VLES demonstrates good results and an improvement of the extrema values in comparison to the $k - \varepsilon$ VLES approach, which produces results very similar to the DDES $\zeta - f$ model. The best agreement with the measured data is demonstrated with the $\zeta - f$ RANS method, which produces the smallest difference from the reference data in the prediction of the maximum and minimum values. The symmetry of the averaged y-displacement that appeared in the experiment can be captured by $\zeta - f$ VLES and $\zeta - f$ RANS methods, whereas the other two models produce asymmetrical issues.

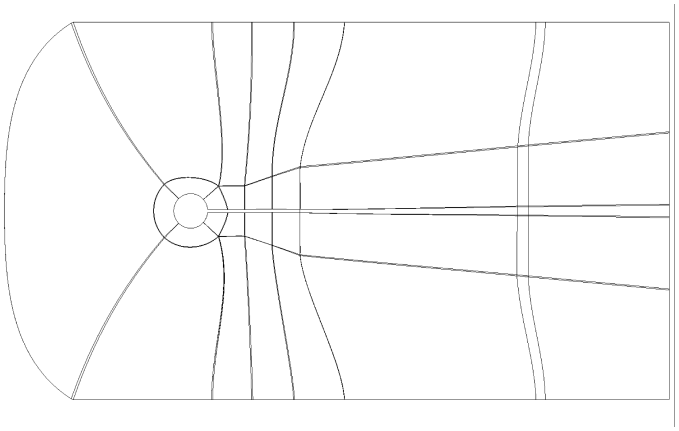

Figure 8.2: Block distribution in the grid for FSI-PfS-1a test case.

Geometry	
Cylinder diameter	$D = 0.0220\,\mathrm{m}$
Deformation structure length	$l_s = 0.0600\,\mathrm{m}$
Deformation structure height	$h_s = 0.0021\,\mathrm{m}$
Flow parameters	
Inflow velocity	$U_0 = 1.385\,\mathrm{m/s^2}$
Density	$\rho_f = 1000\,\mathrm{kg/m^3}$
Dynamic viscosity	$\mu_f = 1.0 \times 10^{-3}$Pa s
Structure parameters	
Structure density	$\rho_s = 1360\,\mathrm{kg/m^3}$
Young's modulus	$E_s = 16\,\mathrm{MPa}$
Poisson's ration	$\nu_s = 0.48$

Table 8.1: Geometrical configuration, flow and structure parameters for FSI-PfS-1a test case [31].

In Table 8.2, the flow parameters obtained by the experiment and produced by the LES [31] and VLES simulations are presented. The VLES results show reasonably good agreement with the experimental data. The biggest deviation from the experimental data is demonstrated by the $k-\varepsilon$ VLES model. The difference in the maximum value is about 10.5% and the error in the value of $U^*_{y_{\min}}$ is greater due to the asymmetry in the $k-\varepsilon$ VLES results, amounting to about 16.2%. The difference in maximum and minimum values between experimental data and results produced by the VLES $\zeta - f$ simulation for both positions is about 11.0%. Values of the oscillation

frequency f_{FSI} as well as values of the extrema of y-displacement, are underpredicted by both VLES models. The same tendency is exhibited in the DDES $\zeta - f$ model (see figure 8.3), which applies the same grid. In contrast to these results, the values obtained by the LES simulation [31] are overpredicted, with $\approx 10\%$ on the mesh, which consist of about 13.5 million control volumes. It is recognized, that the VLES model demonstrates results very similar to those of the LES method already on a mesh with eight times less control volumes than the LES grid. Therefore, the application of VLES model leads to significant reduction of computational effort in comparison to the LES.

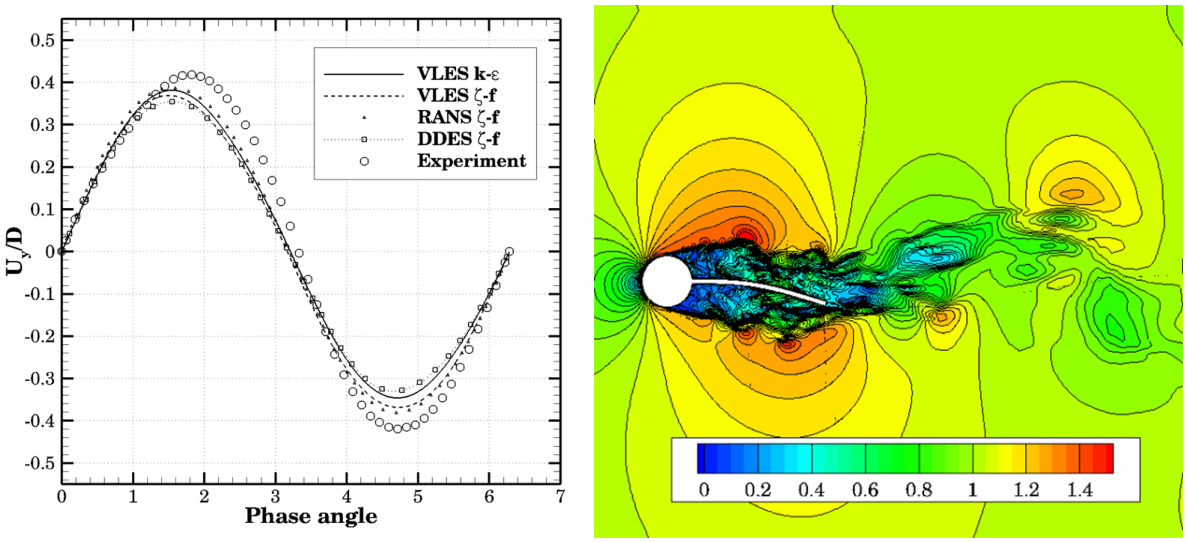

(a) Averaged y-displacement for FSI-PfS-1a test case (b) Velocity magnitude obtained by $\zeta - f$ VLES

Figure 8.3: Averaged y-displacement and velocity magnitude for FSI-PfS-1a test case.

Model	f_{FSI}	Err %	$U_{y_{max}}$	Err %	Uy_{min}	Err %
ref. experiment [31]	7.1	-	0.418	-	-0.420	-
ref. LES [31]	7.08	-0.25	0.456	9.1	-0.464	10.6
VLES $k - \varepsilon$	6.98	-1.69	0.374	-10.5	-0.350	-16.2
VLES $\zeta - f$	6.99	-1.55	0.369	-11.72	-0.370	-11.9

Table 8.2: Comparison of the flow parameters for FSI-PfS-1a test case.

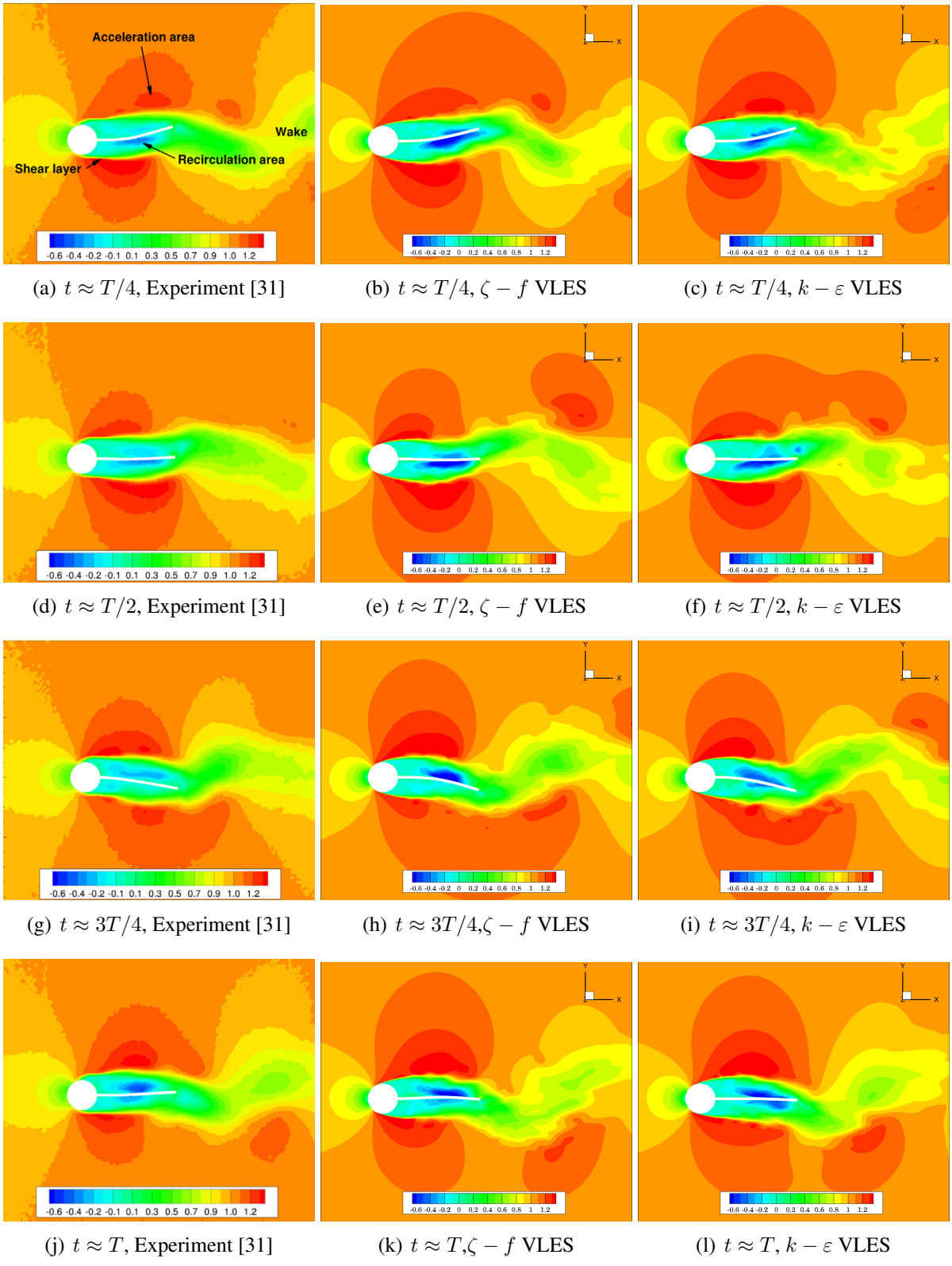

(a) $t \approx T/4$, Experiment [31] (b) $t \approx T/4$, $\zeta - f$ VLES (c) $t \approx T/4$, $k - \varepsilon$ VLES

(d) $t \approx T/2$, Experiment [31] (e) $t \approx T/2$, $\zeta - f$ VLES (f) $t \approx T/2$, $k - \varepsilon$ VLES

(g) $t \approx 3T/4$, Experiment [31] (h) $t \approx 3T/4$,$\zeta - f$ VLES (i) $t \approx 3T/4$, $k - \varepsilon$ VLES

(j) $t \approx T$, Experiment [31] (k) $t \approx T$,$\zeta - f$ VLES (l) $t \approx T$, $k - \varepsilon$ VLES

Figure 8.4: Comparison of experimental and numerical streamwise velocity components for FSI-PfS-1a.

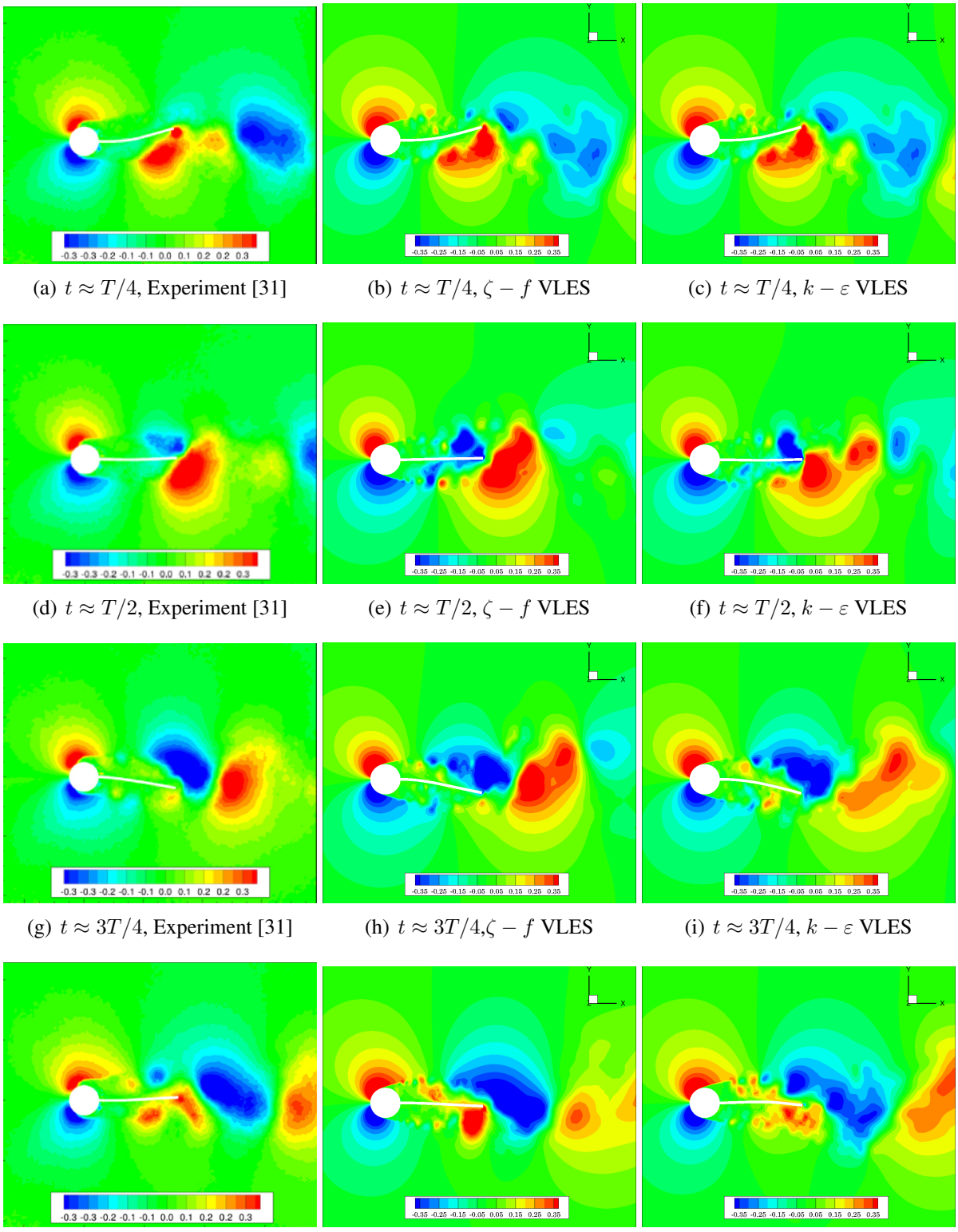

(a) $t \approx T/4$, Experiment [31] (b) $t \approx T/4$, $\zeta - f$ VLES (c) $t \approx T/4$, $k - \varepsilon$ VLES

(d) $t \approx T/2$, Experiment [31] (e) $t \approx T/2$, $\zeta - f$ VLES (f) $t \approx T/2$, $k - \varepsilon$ VLES

(g) $t \approx 3T/4$, Experiment [31] (h) $t \approx 3T/4$,$\zeta - f$ VLES (i) $t \approx 3T/4$, $k - \varepsilon$ VLES

(j) $t \approx T$, Experiment [31] (k) $t \approx T$,$\zeta - f$ VLES (l) $t \approx T$, $k - \varepsilon$ VLES

Figure 8.5: Comparison of experimental and numerical transverse velocity components for FSI-PfS-1a.

The VLES results demonstrate qualitatively good agreement with the experimental data for the phase-averaged streamwise and transverse velocity components (see Figures 8.4 and 8.5). The images in Figure 8.4 in the top row illustrate the position of the cylinder with the attached sheet at $t \approx T/4$. In this position, the attached structure reaches its maximum displacement in an upward direction. Afterwards, the flexible sheet moves downwards, and at $t \approx T/2$ takes almost undeformed shape (Figure 8.4, second row). Then, the downwards movement proceeds further, until the sheet reaches its maximum deflection on the bottom at $t \approx 3T/4$ (Figure 8.4, third row). At the end of the movement period ($t \approx T$), the attached structure takes the horizontal, almost undeformed position again (Figure 8.4, bottom row).

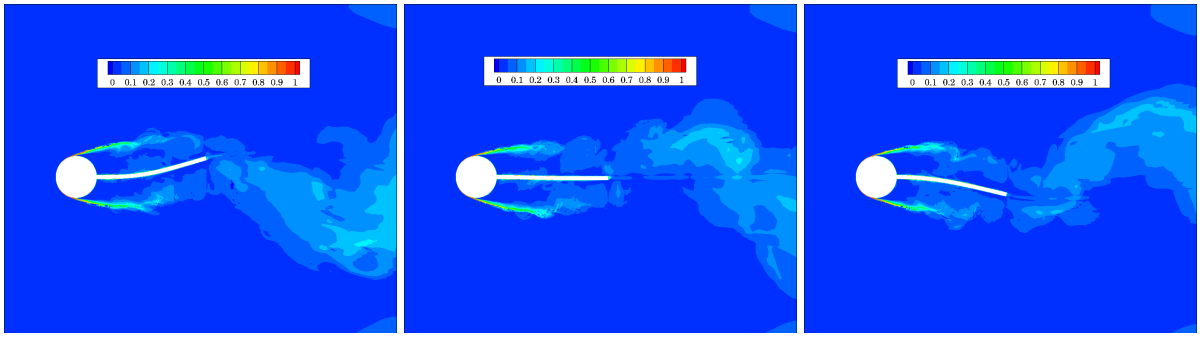

(a) $F_r, t \approx T/4$ (b) $F_r, t \approx T/2$ (c) $F_r, t \approx 3T/4$

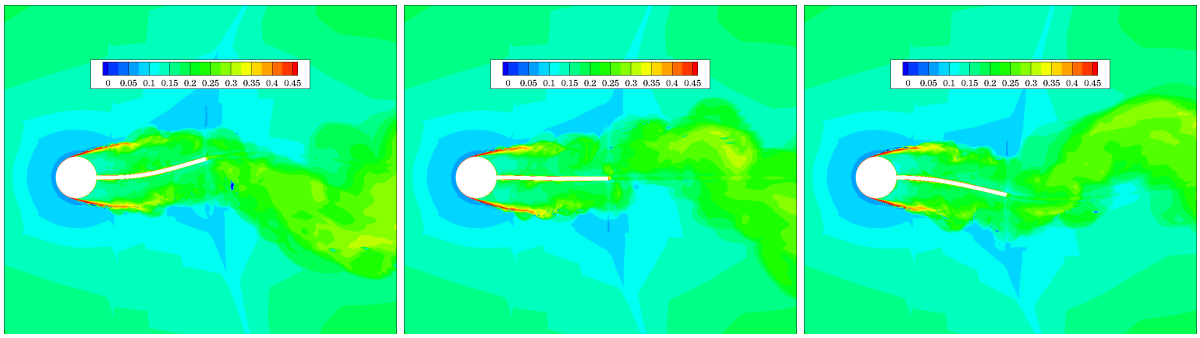

(d) $k_u/k_{total}, t \approx T/4$ (e) $k_u/k_{total}, t \approx T/2$ (f) $k_u/k_{total}, t \approx 3T/4$

Figure 8.6: Resolution control function F_r and modeling ration k_u/k_{total} in FSI-PfS-1a simulation.

A turbulent wake region generated in the upstream of the cylinder with the attached flexible structure at $t \approx T/4$ is very well captured by the VLES methods. The predicted size and position of the vortices in the wake region coincide well with the experimental data. The acceleration area and the shear layer around the attached structure are well recognized in experiment, as well as in the simulation for all positions. The intensity of the recirculation zone around the sheet is insignificantly overestimated by the VLES simulation. In the v-velocities the VLES approach overpredicts the intensity of the small recirculation zone near the sheet, while the big structures are captured very well.

The F_r and the modeling ratio (k_u/k_{total}) are plotted in Figure 8.6 for three different positions of the flexible structure. The RANS mode dominates in the vicinity of the cylinder and the sheet surface, where the wall boundary conditions are applied. The ratio of the modeled length scale to the filter width in this region approaches 1 and therefore most of the turbulent scales are modeled, and the modeling ratio in this area reaches its maximum (Figure 8.6 [d]-[f]). In the wake region, the LES-like behavior is well recognized. It allows the VLES model to resolve different turbulent structures in the vortex-shedding region, and thus, the VLES approach captures well the velocity fluctuations in this area. Although the modeling ratio close to the back surface of the cylinder is quite low, it has no impact on the results, which are in good agreement with the experiment in this region. Due to the correct application of F_r, which damps the turbulent stress tensor, the VLES method demonstrates a capability to resolve small scale flow structures (Figure 8.3 [b]).

The VLES model demonstrates good agreement with the experimental data on a reasonably coarse mesh in comparison to the grid used for the LES simulation. The FSI parameters, such as the oscillating frequency and the extrema of y-displacement, are underpredicted. The values of the error are similar to that produced by the LES simulation. The behavior of the flow is captured very well by the VLES methods: the shedding phenomenon behind the cylinder is clearly identifiable, as are the acceleration zone and recirculation areas close to the flexible structure.

8.2 FSI-PfS-2a test case

The second simulated FSI problem (FSI-PfS-2a) is based on an experiment from Kalmbach and Breuer [80]. This FSI configuration consists of a circular cylinder with an attached flexible rubber sheet with a rear mass at its extremity. The addition of the mass on the end of the sheet leads to the limiting of the structural deflections in two-dimensions, in contrast to the first case, where three-dimensional movement is possible. The geometrical and structural parameters of the rear mass as well as the structural parameters of the flexible rubber sheet, are listed in Table 8.3. All flow parameters and geometrical dimensions remain identical to the settings in the FSI-PfS-1a case. The grid configuration, boundary conditions and numerical setup are also assumed from the Section 8.1 (see Table 8.1 and Figure 8.1). It is important to notice that the simulation contains about 14 swiveling cycles of the flexible structure after the initial phase in contrast to the LES simulation with 30 swiveling cycles.

As mentioned in [30], in this flow configuration in the beginning of the entire cycle ($t \approx T/24$) the flexible structure moves upwards and the sheet is curved. After reaching the maximum position at the top, the sheet changes direction and starts to move downwards ($t \approx 5T/24$). At $t \approx 9T/24$, the middle of the sheet sags down. After the sheet reaches its minimum position in the y-direction ($t \approx 17T/24$), the middle of the sheet distorts upwards, and the sheet sags in the other direction ($t \approx 21T/24$). This structural distortion is correctly captured by the VLES simulation (see Figures 8.8 and 8.9). The acceleration area occurring around the cylinder with the attached sheet easily recognized in the measurements, as well as in the simulation results. The VLES models accurately predict the shedding street and the vortices' position behind the cylinder. Therefore for all positions of the sheet, the predicted structure distortion as well as

the velocity field are in good qualitative agreement with the experimental data. The differences occurring in the velocity field are explained in [30] by means of the measurement problems in the vicinity of the structure boundary.

Geometry	
Rear mass length	$l_m = 0.010\,\mathrm{m}$
Rear mass height	$h_m = 0.002\,\mathrm{m}$
Structure parameters	
Structure density	$\rho_s = 1090\,\mathrm{kg/m^3}$
Structure Young's modulus	$E_s = 4.1\,\mathrm{MPa}$
Structure Poisson's ration	$u_s = 0.48$
Rear mass density	$\rho_r = 7850\,\mathrm{kg/m^3}$
Rear mass Young's modulus	$E_r = 210 \times 10^3$MPa
Rear mass Poisson's ration	$\nu_r = 0.3$

Table 8.3: Geometrical configuration and structure parameters for FSI-PfS-2a test case.

As in the FSI-PfS-1a case, the oscillation frequency is well-know from the experiment and amounts to $f_{FSI} = 11.25$. The $\zeta - f$ VLES model predicts the frequency of the y-displacement very well, with a deviation of 3%. The comparison of the maximum and minimum values shows an error of 2.84% and 0.32%. The error in the prediction of the FSI frequency with the $k - \varepsilon$ VLES model amounts to 4.7%. The deviation from the experimental data for extrema values of the y-displacement is about two times smaller for the minimum value (1.54%) and about seven times bigger for the maximum value than the $\zeta - f$ VLES model. The visible asymmetry is captured very well by the $\zeta - f$ VLES method and is less pronounced by the $k - \varepsilon$ VLES approach. Additionally, Figure 8.7 demonstrates the comparison of the averaged phase between the experimental data and the simulation results produced by the LES, DDES and VLES models.

Model	f_{FSI}	Err %	$U_{y_{max}}$	Err %	Uy_{min}	Err %
ref. experiment [80]	11.25	-	0.667	-	-0.629	-
ref. LES [30]	11.53	2.49	0.670	0.5	-0.674	7.2
VLES $k - \varepsilon$	10.72	-4.7	0.657	-1.54	-0.643	-2.18
VLES $\zeta - f$	10.90	-3.1	0.648	-2.84	-0.627	-0.32

Table 8.4: Comparison of the flow parameters for FSI-PfS-2a test case.

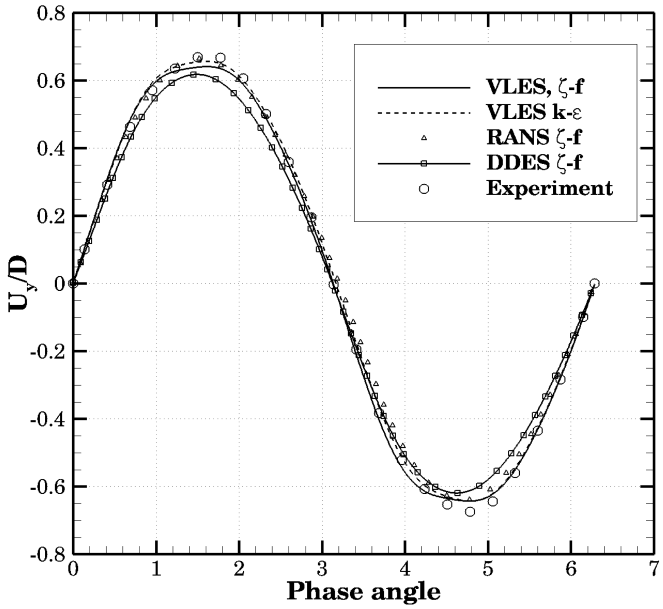

Figure 8.7: Averaged y-displacement for FSI-PfS-2a test case.

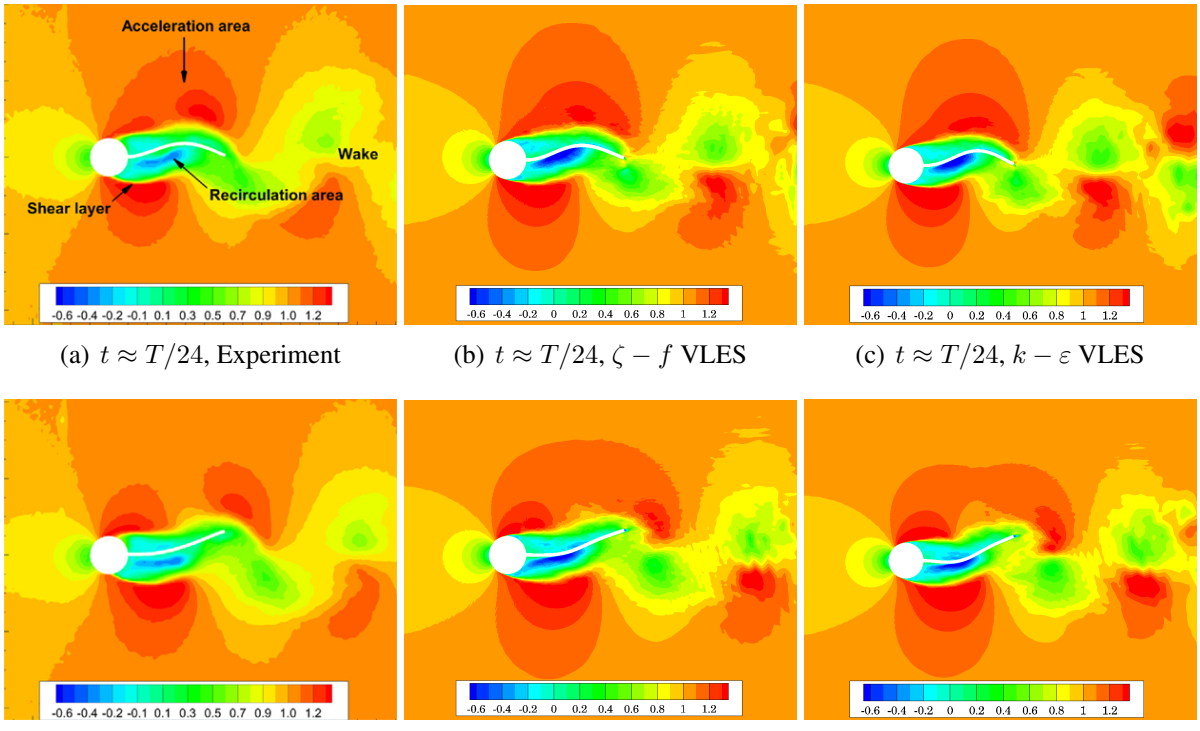

(a) $t \approx T/24$, Experiment (b) $t \approx T/24$, $\zeta - f$ VLES (c) $t \approx T/24$, $k - \varepsilon$ VLES

(d) $t \approx 5T/24$, Experiment (e) $t \approx 5T/24$, $\zeta - f$ VLES (f) $t \approx 5T/24$, $k - \varepsilon$ VLES

Figure 8.8: Comparison of experimental and numerical streamwise transverse components for FSI-PfS-2a.

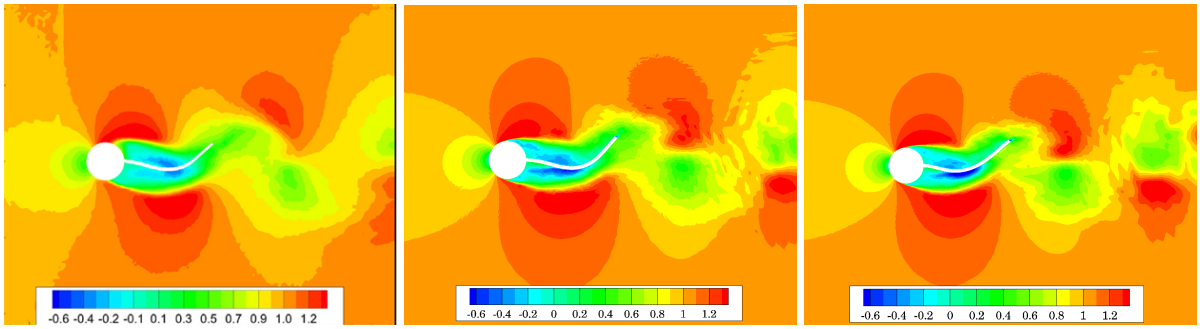

(a) $t \approx 9T/24$, Experiment (b) $t \approx 9T/24$, $\zeta - f$ VLES (c) $t \approx 9T/24$, $k - \varepsilon$ VLES

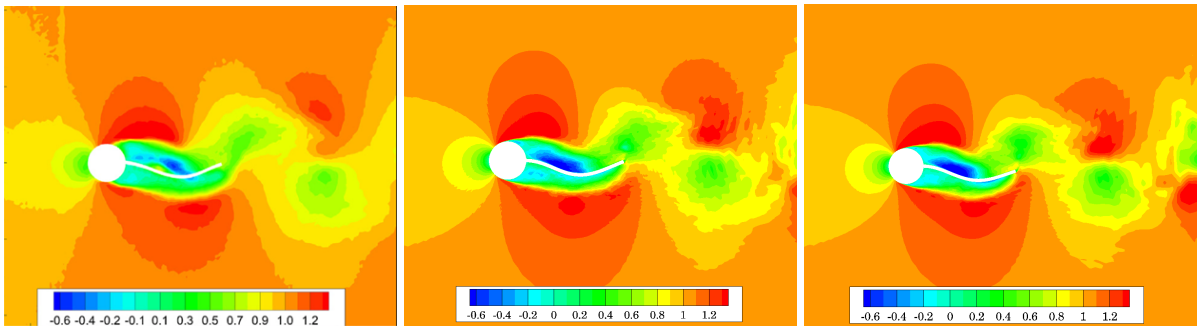

(d) $t \approx 13T/24$, Experiment (e) $t \approx 13T/24$, $\zeta - f$ VLES (f) $t \approx 13T/24$, $k - \varepsilon$ VLES

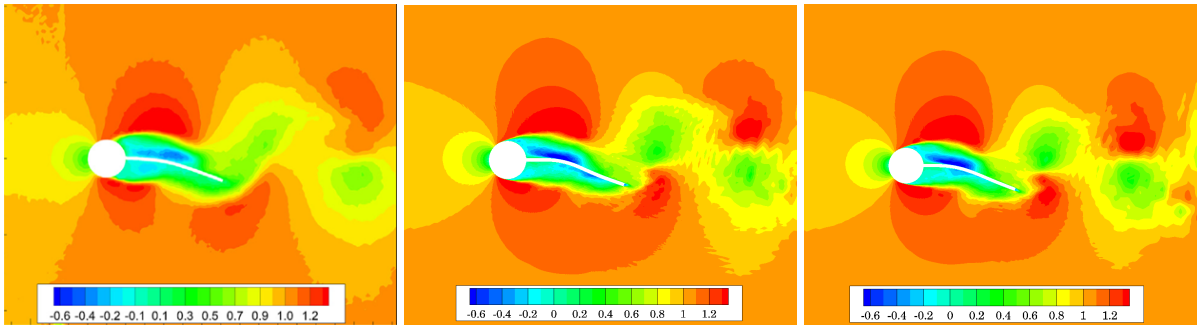

(g) $t \approx 17T/24$, Experiment (h) $t \approx 17T/24$, $\zeta - f$ VLES (i) $t \approx 17T/24$, $k - \varepsilon$ VLES

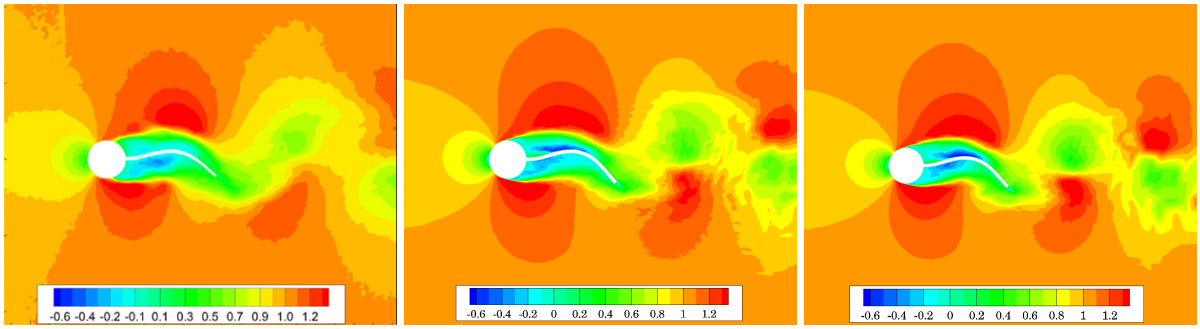

(j) $t \approx 21T/24$, Experiment (k) $t \approx 21T/24$, $\zeta - f$ VLES (l) $t \approx 21T/24$, $k - \varepsilon$ VLES

Figure 8.9: Comparison of experimental and numerical streamwise components for FSI-PfS-2a.

As in the first test case, the DDES result are assumed from the work of [1]. The deviations between different modeling techniques in the FSI-PfS-2a test case are less significant than in the first test case. As in the FSI-PfS-1a simulation, the $\zeta - f$ RANS model demonstrates the best agreement with the measurement data, and the $\zeta - f$ DDES method shows the biggest deviation from the experiment.

The VLES method demonstrates the capability to capture a variety of turbulent structures in this multiphysics flow configuration. The displacement frequency and the extrema of the y-displacement coincide well with the experimental data. The main behavior of the flow, such as vortex shedding, shear layer and acceleration area, are predicted very well by the VLES simulation. Furthermore, the VLES method is able to resolve small scale flow structures (Figure 8.10)

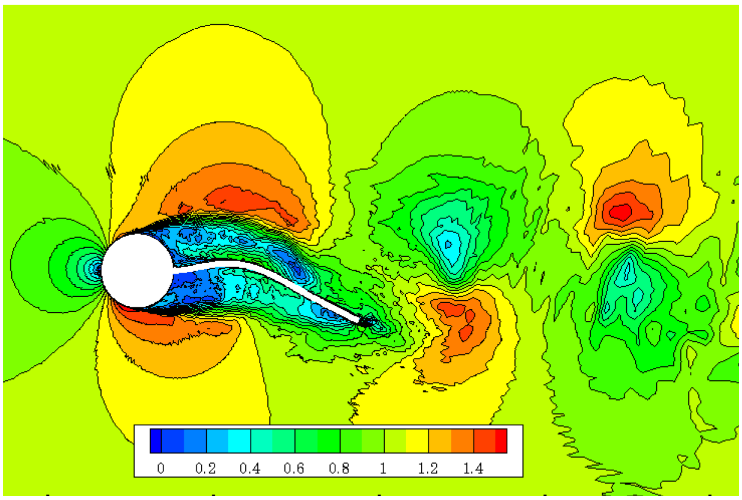

Figure 8.10: Velocity magnitude for FSI-PfS-2a test case.

9 Conclusion

This study has been conducted at the department of numerical methods in mechanical engineering at the TU Darmstadt in order to extend the turbulence modeling part in the in-house code FASTEST with the new turbulence hybrid model, so-called very large eddy simulation method. By means of this solver, the abilities of this relatively new turbulence model were investigated on both stationary and on moving grids and in the context of fluid-structure interaction.

9.1 Summary of findings

The VLES model with three different underlying RANS methods, namely Chien $k-\varepsilon$, Wilcox $k-\omega$ and $\zeta-f$ approaches, was implemented in the in-house code FASTEST. Each of these models is suitable for prediction of different types of turbulent flows due to their properties. For instance, the capability of the Wilcox $k-\omega$ model to predict correctly the wall-bounded flows is well-known, as are the advantages of the Chien $k-\varepsilon$ in a simulations of flows with mild separations [171]. In contrast to the other two models, the $\zeta-f$ method is able to capture anisotropy effects in the vicinity of the wall, so this approach is better suited for wall-bounded flows than the models with damping functions, as the Chien $k-\varepsilon$ model. Since the RANS equations are applied in the formulation of the VLES approach, the verification of these RANS methods with the method of manufactured solution was realized to ensure the correct performance of the VLES model. The verification results have demonstrated the correct implementation of equations and boundary conditions within the FASTEST code.

After the verification procedure, the newly implemented VLES models were systematically validated on stationary grids. Three different flow configurations were selected to demonstrate the ability of the VLES approach to predict different types of turbulent flows. To cover wall-bounded flows, the channel flow at $Re_\tau = 590$ and $Re_\tau = 395$ was simulated. For examination of the VLES model in a simulation of a flow over a bluff body, a flow over a circular cylinder at $Re = 3,900$ was investigated. Finally a flow over periodic hills at $Re = 10,595$ was chosen to demonstrate the advantages of the VLES approach in a flow with separations. The $k-\varepsilon$ and $\zeta-f$ VLES methods have shown a reasonably good agreement with the reference data for all three test cases. It is important to notice that the simulations were performed on coarser grids compared to the grids required for the LES method. The $k-\omega$ VLES model yielded very good results for the cylinder flow and for the two-dimensional periodic hills flow, while in the prediction of the fully developed turbulent channel flow this method demonstrated weaknesses. To improve the results of the $k-\omega$ VLES model, this method was modified by means of the introduction of a new filter width, so-called IDDES, in the formulation of the VLES model. It was shown that the application of the IDDES criterion Δ_{IDDES} instead of the standard volume Δ_{vol} leads to a

significant improvement of the results already on a quite coarse grid. It was well recognized that the filter width has a significant influence on the results within the VLES model in the case of anisotropic meshes and that this influence decreases with the refinement of the mesh resolution. Additionally, different grid configurations subdivided by stretching factors were investigated. As expected, the results of the VLES model depends of the mesh quality. However, the results produced with the IDDES-VLES method demonstrated improvement over the volume criterion already on the grid with a big stretching factor.

The next step was an examination of the behavior of the VLES approach on moving grids. Firstly, this technique was applied to simulate the flow over a forced oscillating circular cylinder at $Re = 10,000$. Afterwards, a flow over a tandem of an oscillating and a static asymmetric SD7003 airfoil, at $Re = 30,000$, was investigated. The VLES method demonstrated an ability to simulate turbulent flows with strongly moving structures. The character of investigated flows was captured very well for both test cases. The lift and drag coefficients were also predicted reasonably well. Deviations occurred in the first case in the calculation of the lift coefficient, while in the second test case, the drag coefficient distribution could not be captured in accordance with the experiment. A refinement of the grid in the second case may lead to improved results, since the drag force depends strongly on the shear stress in this flow configuration, which is sensitive to the mesh resolution. The fine mesh was not investigated in the framework of this work, because the goal was to test the VLES model on coarse meshes that are suitable for URANS simulations.

The last step was an investigation of the VLES approach in the context of a fluid-structure coupling. To this end, two FSI test cases were investigated. In both cases, the VLES method demonstrated a capability to capture a variety of turbulent structures in these configurations. The displacement frequency and the extrema of the y-displacement coincided well with the experimental data. The behavior of the flow was captured correctly by both VLES methods: the shedding phenomenon behind the cylinder was clearly identifiable as were the acceleration zone and recirculation areas close to the flexible structure. Furthermore, the VLES method is able to resolve small scale flow structures.

In summary, the ability of the VLES model to predict different kinds of turbulent flows correctly was demonstrated by means of different test cases on stationary as well on moving grids. For all simulations, a relatively coarse grid, in comparison to this required for the correct LES calculation, was applied. The application of this hybrid turbulence model is very promising because of its capability to predict flows with mild and massive separations, more accurately that RANS methods and due to the reduced computational effort in comparison to LES approaches.

9.2 Outlook

In the present work, the dependence of the VLES results on grid quality was demonstrated. A detailed investigation of the influence of the mesh resolution on the results obtained by the VLES model can be further investigated, though, especially in the case of moving grids, where the grid configuration changes in each time step. With grid refinement, an improvement of the lift and the drag coefficient values is expected. The calculation with moving structures is an additional

challenge for the VLES model, which switches seamless between two modes depending on the numerical grid resolution. For this approach a change of the interface between DNS and RANS modes can directly impact the overall results. In the case of moving grids, the RANS mode is active in the shear layer region, this behavior can be reduced by means of the grid adaptation. Therefore, for future work, it is of interest to investigate adaptive grid techniques in the context of moving structures. Adaptive grids can influence the switching between the two modes in the VLES method and may lead to a reduction of computational time and an improvement in results.

Since the application of the new filter width in the formulation of the VLES model leads to significant improvements of the results, the detailed investigation of the influence of Δ in the FSI cases and on moving grids would be useful in future studies. Moreover, another alternative formulation of the filter width can be investigated.

Additionally, the investigation of the VLES model, which demonstrated very good results in academic cases, for complex FSI cases is very promising and therefore interesting for subsequent investigations of the VLES method.

List of Figures

List of Tables

Glossary

Δ	filter width
δ_{ij}	Kronecker delta
ε	dissipation of the turbulent kinetic energy
η	Kolmogorov length scale
κ	wavenumber
λ	Taylor length scale
μ	dynamic viscosity
ν	kinematic viscosity
ν_P	Poisson's ratio
ν_t	turbulent viscosity
ω	specific dissipation
$\phi'(x,t)$	fluctuation part of ϕ
ϕ_{ms}	manufactured solution
$\phi(x,t)$	generic flow quantity
$\overline{\phi}(x,t)$	ensemble averaged ϕ
ρ	density
τ	shear stress
τ_0	turbulent time scale
τ_η	Kolmogorov time scale
τ_λ	Taylor time scale
τ^{turb}	Reynolds stresses
τ_w	wall shear stress
ζ	velocity scale ratio
C_D	drag coefficient
C_f	skin friction coefficient
C_L	lift coefficient
C_μ^ζ	model constant in the $\zeta - f$ model

E	Young's modulus
$E(\kappa)$	energy spectrum
F_r	resolution control function
L	characteristic linear dimension
Ma	Mach number
Q	source term
Re	Reynolds number
Re_{cr}	critical Reynolds number
$\overline{S_{ij}}$	mean rate of strain tensor
T	Cauchy stress tensor
T_{ij}	components of the Cauchy stress tensor
U	characteristic flow velocity
U_0	inflow velocity
V	material volumes
d	the minimum distance to the wall
d_w	distance to the wall
e_h	approximation error
f	elliptic relaxation function
f_0	non-dimensional frequency
f_i	volume forces
f_t	period frequency in the case of tandem flow
h_0	plunge amplitude in the case of tandem flow
h_{max}	maximum local grid spacing
h_t	time-depend plunge position in the case of tandem flow
h_{wn}	grid distance in the wall-normal direction
k	turbulent kinetic energy
l	length scale
l_0	turbulent length scale
l_c	turbulent length scale related to the spectral cut-off
m	mass
n_j	normal vector
p	pressure
p_0	formal order of accuracy

p_c	observer order of accuracy
$\overline{u_i' u_j'}$	components of Reynolds stress tensor
u_0	turbulent velocity scale
u_b	bulk velocity
u_η	Kolmogorov velocity scale
u_i	velocity components in the i direction
u_λ	Taylor velocity scale
u^+	non-dimensional mean velocity
u_τ	shear velocity
y^+	non-dimensional wall distance

Acronyms

ALE	arbitrary Lagrangian-Eulerian
CBC	convection boundedness criterion
CDS	central differencing scheme
CFL	Courant–Friedrichs–Lewy
CV	control volume
DDES	delayed detached eddy simulation
DES	detached eddy simulation
DNS	direct numerical simulation
ER	eddy-resolved (model)
EVM	eddy-viscosity model
FASTEST	Flow Analysis by Solving of Transport Equations Simulating Turbulence
FSI	fluid structure interaction
FVM	finite volume method
IDDES	improved delayed detached eddy simulation
LES	large eddy simulation
MMS	method of the manufactured solution
MUSCL	monotone upstream-centered schemes of conservation laws
NVF	normalized variable formulation
QUICK	quadratic upstream interpolation for convective kinematics
RANS	Reynolds-average Navier-Stokes
RMS	root mean square
RMS	Reynolds stress model
SGS	sub-grid scale
SIMPLE	semi-implicit method for pressure linked equations
SIP	strongly implicit procedure
SOFI	second order fully implicit method
TEV	eading-edge vortex

TEV	trailing-edge vortex
TVD	total variation diminishing scheme
UDS	upwind differencing scheme
URANS	unsteady Reynolds-average Navier-Stokes
VLES	very large eddy simulation

Bibliography

[1] A. Ali. *On the Simulation of Turbulent Fluid-Structure Interaction*. dissertation, FNB, TU Darmstadt, 2017.

[2] A. Ali, T. Reimann, D. C. Sternel, and M. Schäfer. Comparison of advanced turbulence modeling approaches for fluid-structure interaction. In *Coupled Problems in Science and Engineering VI*, International Center for Numerical Methods in Engineering (CIMNE), pages 512–523, June 2015. URL `http://tubiblio.ulb.tu-darmstadt.de/73950/`.

[3] N. Alkishriwi, M. Meinke, and W. Schröder. A large-eddy simulation method for low mach number flows using preconditioning and multigrid. *Computers & fluids*, 35(10): 1126–1136, 2006.

[4] M. Alves, P. Oliveira, and F. Pinho. A convergent and universally bounded interpolation scheme for the treatment of advection. *International journal for numerical methods in fluids*, 41(1):47–75, 2003.

[5] F. P. Baaijens. A fictitious domain/mortar element method for fluid-structure interaction. *International Journal for Numerical Methods in Fluids*, 35(7):743–761, 2001.

[6] B. S. Baldwin and H. Lomax. *Thin layer approximation and algebraic model for separated turbulent flows*, volume 257. American Institute of Aeronautics and Astronautics, 1978.

[7] Y. Bazilevs, K. Takizawa, and T. E. Tezduyar. *Computational fluid-structure interaction: methods and applications*. John Wiley & Sons, 2013.

[8] Y. Bazilevs, K. Takizawa, T. E. Tezduyar, M.-C. Hsu, N. Kostov, and S. McIntyre. Aerodynamic and fsi analysis of wind turbines with the ale-vms and st-vms methods. *Archives of Computational Methods in Engineering*, 21(4):359–398, 2014.

[9] T. Belytschko and T. J. Hughes. Computational methods for transient analysis. *Computational Methods in Mechanics*, 1, 2013.

[10] T. Belytschko, J. M. Kennedy, and D. Schoeberle. Quasi-eulerian finite element formulation for fluid-structure interaction. *Journal of Pressure Vessel Technology*, 102(1):62–69, 1980.

[11] R. P. Beyer. A computational model of the cochlea using the immersed boundary method. *Journal of Computational Physics*, 98(1):145–162, 1992.

[12] F. Billard and D. Laurence. A robust k- ε-/k elliptic blending turbulence model applied to near-wall, separated and buoyant flows. *International Journal of Heat and Fluid Flow*, 33 (1):45–58, 2012.

[13] G. Biswas and V. Eswaran. *Turbulent flows: fundamentals, experiments and modeling*. CRC Press, 2002.

[14] F. J. Blom. A monolithical fluid-structure interaction algorithm applied to the piston problem. *Computer methods in applied mechanics and engineering*, 167(3):369–391, 1998.

[15] I. Borazjani, L. Ge, and F. Sotiropoulos. Curvilinear immersed boundary method for simulating fluid structure interaction with complex 3d rigid bodies. *Journal of Computational physics*, 227(16):7587–7620, 2008.

[16] J. Boussinesq. *Essai sur la théorie des eaux courantes*. Imprimerie nationale, 1877.

[17] P. Bradshaw. *An Introduction to Turbulence and Its Measurement: Thermodynamics and Fluid Mechanics Series*. Elsevier, 2013.

[18] M. Breuer. Large eddy simulation of the subcritical flow past a circular cylinder: numerical and modeling aspects. *International Journal for Numerical Methods in Fluids*, 28(9): 1281–1302, 1998.

[19] M. Breuer and M. Münsch. Les meets fsi–important numerical and modeling aspects. In *Direct and Large-Eddy Simulation VII*, pages 239–245. Springer, 2010.

[20] M. Breuer, G. De Nayer, and M. Münsch. Fluid–structure interaction of a flexible structure in a turbulent flow using les. In *Direct and Large-Eddy Simulation VIII*, pages 449–454. Springer, 2011.

[21] M. Breuer, G. De Nayer, M. Münsch, T. Gallinger, and R. Wüchner. Fluid–structure interaction using a partitioned semi-implicit predictor–corrector coupling scheme for the application of large-eddy simulation. *Journal of Fluids and Structures*, 29:107–130, 2012.

[22] U. Bunge. Numerische simulation turbulenter strömungen im kontext der wechselwirkung zwischen fluid und struktur. 2005.

[23] J. Carberry, J. Sheridan, and D. Rockwell. Controlled oscillations of a cylinder: forces and wake modes. *Journal of Fluid Mechanics*, 538:31–69, 2005.

[24] C.-Y. Chang, S. Jakirlić, K. Dietrich, B. Basara, and C. Tropea. Swirling flow in a tube with variably-shaped outlet orifices: An les and vles study. *International Journal of Heat and Fluid Flow*, 49:28–42, 2014.

[25] K.-Y. Chien. Predictions of channel and boundary-layer flows with a low-reynolds-number turbulence model. *AIAA journal*, 20(1):33–38, 1982.

[26] J.-I. Choi, R. C. Oberoi, J. R. Edwards, and J. A. Rosati. An immersed boundary method for complex incompressible flows. *Journal of Computational Physics*, 224(2):757–784, 2007.

[27] H. N. Das. Effect of structural deformation on performance of marine propeller. *Journal of Maritime Research*, 11(3):43–49, 2014.

[28] P. A. Davidson. *Turbulence: an introduction for scientists and engineers*. Oxford University Press, 2015.

[29] J. De Hart, G. W. Peters, P. J. Schreurs, and F. P. Baaijens. A two-dimensional fluid–structure interaction model of the aortic value. *Journal of biomechanics*, 33(9):1079–1088, 2000.

[30] G. De Nayer and M. Breuer. Numerical fsi investigation based on les: Flow past a cylinder with a flexible splitter plate involving large deformations (fsi-pfs-2a). *International Journal of Heat and Fluid Flow*, 50:300–315, 2014.

[31] G. De Nayer, A. Kalmbach, M. Breuer, S. Sicklinger, and R. Wüchner. Flow past a cylinder with a flexible splitter plate: A complementary experimental–numerical investigation and a new fsi test case (fsi-pfs-1a). *Computers & Fluids*, 99:18–43, 2014.

[32] J. Degroote, K.-J. Bathe, and J. Vierendeels. Performance of a new partitioned procedure versus a monolithic procedure in fluid–structure interaction. *Computers & Structures*, 87 (11):793–801, 2009.

[33] I. Demirdžić and M. Perić. Space conservation law in finite volume calculations of fluid flow. *International journal for numerical methods in fluids*, 8(9):1037–1050, 1988.

[34] A. Dervieux, M. Braza, and J.-P. Dussauge. *Computation and Comparison of Efficient Turbulence Models for Aeronautics—European Research Project ETMA*, volume 5. Springer Science & Business Media, 2013.

[35] J. Donea, S. Giuliani, and J.-P. Halleux. An arbitrary lagrangian-eulerian finite element method for transient dynamic fluid-structure interactions. *Computer methods in applied mechanics and engineering*, 33(1-3):689–723, 1982.

[36] S. Dong and G. E. Karniadakis. Dns of flow past a stationary and oscillating cylinder at. *Journal of Fluids and Structures*, 20(4):519–531, 2005.

[37] P. Durbin. A reynolds stress model for near-wall turbulence. *Journal of Fluid Mechanics*, 249:465–498, 1993.

[38] P. Durbin. On the k-3 stagnation point anomaly. *International journal of heat and fluid flow*, 17(1):89–90, 1996.

[39] P. A. Durbin. Near-wall turbulence closure modeling without "damping functions". *Theoretical and Computational Fluid Dynamics*, 3(1):1–13, 1991.

[40] L. Eça, M. Hoekstra, A. Hay, and D. Pelletier. On the construction of manufactured solutions for one and two-equation eddy-viscosity models. *International journal for numerical methods in fluids*, 54(2):119–154, 2007.

[41] L. Eça, M. Hoekstra, A. Hay, and D. Pelletier. A manufactured solution for a two-dimensional steady wall-bounded incompressible turbulent flow. *International Journal of Computational Fluid Dynamics*, 21(3-4):175–188, 2007.

[42] L. Eça, M. Hoekstra, A. Hay, and D. Pelletier. Verification of rans solvers with manufactured solutions. *Engineering with computers*, 23(4):253–270, 2007.

[43] C. Farhat. Cfd-based nonlinear computational aeroelasticity. *Encyclopedia of computational mechanics*, 2004.

[44] H. Fasel, J. Seidel, and S. Wernz. A methodology for simulations of complex turbulent flows. *Journal of fluids engineering*, 124(4):933–942, 2002.

[45] J. H. Ferziger and M. Perić. *Computational methods for fluid dynamics*, volume 3. Springer Berlin, 2002.

[46] C. Förster. *Robust methods for fluid-structure interaction with stabilised finite elements*. 2007.

[47] J. Franke and W. Frank. Large eddy simulation of the flow past a circular cylinder at re d= 3900. *Journal of wind engineering and industrial aerodynamics*, 90(10):1191–1206, 2002.

[48] J. Fröhlich. *Large Eddy Simulation turbulenter Strmungen*. Springer DE, 2006.

[49] J. Fröhlich and D. von Terzi. Hybrid les/rans methods for the simulation of turbulent flows. *Progress in Aerospace Sciences*, 44(5):349–377, 2008.

[50] W. Frost. *Handbook of Turbulence: Volume 1 Fundamentals and Applications*. Springer Science & Business Media, 2012.

[51] P. Gaskell and A. Lau. Curvature-compensated convective transport: Smart, a new boundedness-preserving transport algorithm. *International journal for numerical methods in fluids*, 8(6):617–641, 1988.

[52] M. Germano, U. Piomelli, P. Moin, and W. H. Cabot. A dynamic subgrid-scale eddy viscosity model. *Physics of Fluids A: Fluid Dynamics (1989-1993)*, 3(7):1760–1765, 1991.

[53] S. S. Girimaji. Partially-averaged navier-stokes model for turbulence: A reynolds-averaged navier-stokes to direct numerical simulation bridging method. *Journal of Applied Mechanics*, 73(3):413–421, 2006.

[54] R. Golshan, A. E. Tejada-Martínez, M. J. Juha, and Y. Bazilevs. Les and rans simulation of wind-and wave-forced oceanic turbulent boundary layers in shallow water with wall modeling. *Computers & Fluids*, 2016.

[55] R. Gopalkrishnan. Vortex-induced forces on oscillating bluff cylinders. Technical report, DTIC Document, 1993.

[56] W. J. Gordon and C. A. Hall. Construction of curvilinear co-ordinate systems and applications to mesh generation. *International Journal for Numerical Methods in Engineering*, 7(4):461–477, 1973.

[57] M. S. Gritskevich, A. V. Garbaruk, J. Schütze, and F. R. Menter. Development of ddes and iddes formulations for the k-ω shear stress transport model. *Flow, turbulence and combustion*, 88(3):431–449, 2012.

[58] X. Han and S. Krajnović. A new very large eddy simulation model for simulation of turbulent flow. In *Progress in Hybrid RANS-LES Modelling*, pages 131–140. Springer, 2012.

[59] X. Han and S. Krajnović. An efficient very large eddy simulation model for simulation of turbulent flow. *International Journal for Numerical Methods in Fluids*, 71(11):1341–1360, 2013.

[60] X. Han and S. Krajnović. Validation of a novel very large eddy simulation method for simulation of turbulent separated flow. *International Journal for Numerical Methods in Fluids*, 73(5):436–461, 2013.

[61] K. Hanjalic. *Two-dimensional asymmetric turbulent flow in ducts*. PhD thesis, Ph. D. Thesis, University of London, 1970.

[62] K. Hanjalic and B. Launder. A reynolds stress model of turbulence and its application to thin shear flows. *Journal of fluid Mechanics*, 52(04):609–638, 1972.

[63] K. Hanjalić, M. Popovac, and M. Hadžiabdić. A robust near-wall elliptic-relaxation eddy-viscosity turbulence model for cfd. *International Journal of Heat and Fluid Flow*, 25(6): 1047–1051, 2004.

[64] F. H. Harlow and P. I. Nakayama. Transport of turbulence energy decay rate. Technical report, Los Alamos Scientific Lab., N. Mex., 1968.

[65] A. Harten. High resolution schemes for hyperbolic conservation laws. *Journal of computational physics*, 49(3):357–393, 1983.

[66] M. Heil, A. L. Hazel, and J. Boyle. Solvers for large-displacement fluid–structure interaction problems: segregated versus monolithic approaches. *Computational Mechanics*, 43 (1):91–101, 2008.

[67] C. Hirt, A. A. Amsden, and J. Cook. An arbitrary lagrangian-eulerian computing method for all flow speeds. *Journal of Computational Physics*, 14(3):227–253, 1974.

[68] G. Hou, J. Wang, and A. Layton. Numerical methods for fluid-structure interaction—a review. *Communications in Computational Physics*, 12(02):337–377, 2012.

[69] J. Hron and S. Turek. A monolithic fem/multigrid solver for an ale formulation of fluid-structure interaction with applications in biomechanics. In *Fluid-structure interaction*, pages 146–170. Springer, 2006.

[70] B. Hübner, E. Walhorn, and D. Dinkler. A monolithic approach to fluid–structure interaction using space–time finite elements. *Computer methods in applied mechanics and engineering*, 193(23):2087–2104, 2004.

[71] T. J. Hughes, W. K. Liu, and T. K. Zimmermann. Lagrangian-eulerian finite element formulation for incompressible viscous flows. *Computer methods in applied mechanics and engineering*, 29(3):329–349, 1981.

[72] R. N. Ihi, L. A. C. Schiavo, J. H. A. Azevedo, and J. L. F. Azevedo. Numerical investigation of the fluid-structure interaction in 2-d flow over a cylinder. 2013.

[73] D. M. Israel. A new approach for turbulent simulations in complex geometries. 2005.

[74] S. Jakirlic and K. Hanjalic. A new approach to modelling near-wall turbulence energy and stress dissipation. *Journal of fluid mechanics*, 459:139–166, 2002.

[75] H. Jasak, H. Weller, and A. Gosman. High resolution nvd differencing scheme for arbitrarily unstructured meshes. *International journal for numerical methods in fluids*, 31(2): 431–449, 1999.

[76] H. Jeanmart and G. Winckelmans. Comparison of recent dynamic subgrid-scale models in turbulent channel flow. In *Proceedings of the summer program*, pages 105–116. Citeseer, 2002.

[77] S. T. Johansen, J. Wu, and W. Shyy. Filter-based unsteady rans computations. *International Journal of Heat and fluid flow*, 25(1):10–21, 2004.

[78] D. A. Johnson and L. King. A mathematically simple turbulence closure model for attached and separated turbulent boundary layers. *AIAA journal*, 23(11):1684–1692, 1985.

[79] W. Jones and B. Launder. The prediction of laminarization with a two-equation model of turbulence. *International journal of heat and mass transfer*, 15(2):301–314, 1972.

[80] A. Kalmbach and M. Breuer. Experimental piv/v3v measurements of vortex-induced fluid–structure interaction in turbulent flow—a new benchmark fsi-pfs-2a. *Journal of Fluids and Structures*, 42:369–387, 2013.

[81] J. Kim, D. Kim, and H. Choi. An immersed-boundary finite-volume method for simulations of flow in complex geometries. *Journal of Computational Physics*, 171(1):132–150, 2001.

[82] S. Kim, P. A. Wilson, and Z.-M. Chen. Numerical simulation of force and wake mode of an oscillating cylinder. *Journal of Fluids and Structures*, 44:216–225, 2014.

[83] B. Kniesner. *Ein hybrides LES/RANS-Verfahren für konjugierte Impuls-, Wärme-und Stoffübertragung mit Relevanz zu Brennkammerkonfigurationen*. PhD thesis, TU Darmstadt, 2008.

[84] A. N. Kolmogorov. The local structure of turbulence in incompressible viscous fluid for very large reynolds numbers. In *Dokl. Akad. Nauk SSSR*, volume 30, pages 301–305. JSTOR, 1941.

[85] A. N. Kolmogorov. Equations of turbulent motion of an incompressible fluid. In *Dokl. Akad. Nauk SSSR*, volume 6, pages 56–58, 1942.

[86] A. G. Kravchenko and P. Moin. Numerical studies of flow over a circular cylinder at red= 3900. *Physics of Fluids (1994-present)*, 12(2):403–417, 2000.

[87] G. Kumar, S. Lakshmanan, H. Gopalan, and A. De. Investigation of the sensitivity of turbulent closures and coupling of hybrid rans-les models for predicting flow fields with separation and reattachment. *International Journal for Numerical Methods in Fluids*, 2016.

[88] B. Launder and B. Sharma. Application of the energy-dissipation model of turbulence to the calculation of flow near a spinning disc. *Letters in heat and mass transfer*, 1(2): 131–137, 1974.

[89] B. Launder, G. J. Reece, and W. Rodi. Progress in the development of a reynolds-stress turbulence closure. *Journal of fluid mechanics*, 68(03):537–566, 1975.

[90] L. Lee and R. J. LeVeque. An immersed interface method for incompressible navier–stokes equations. *SIAM Journal on Scientific Computing*, 25(3):832–856, 2003.

[91] A. Leonard. Energy cascade in large-eddy simulations of turbulent fluid flows. *Advances in geophysics*, 18:237–248, 1975.

[92] B. Leonard. A stable and accurate convective modelling procedure based on quadratic upstream interpolation. *Int. J. Mech. Sci*, 16:183–308, 1976.

[93] B. Leonard. Locally modified quick scheme for highly convective 2-d and 3-d flows. In *Numerical methods in laminar and turbulent flow*, volume 1, pages 35–47, 1987.

[94] E. Lévêque, F. Toschi, L. Shao, and J.-P. Bertoglio. Shear-improved smagorinsky model for large-eddy simulation of wall-bounded turbulent flows. *Journal of Fluid Mechanics*, 570:491–502, 2007.

[95] F. Lien and M. Leschziner. Computational modelling of 3d turbulent flow in s-diffuser and transition ducts. *Engineering Turbulence Modelling and Experiments*, 2:217–228, 1993.

[96] D. K. Lilly. A proposed modification of the germano subgrid-scale closure method. *Physics of Fluids A: Fluid Dynamics (1989-1993)*, 4(3):633–635, 1992.

[97] L. Lourenco and C. Shih. Characteristics of the plane turbulent near wake of a circular cylinder, a particle image velocimetry study. *private communication*, 1993.

[98] H. Lübcke, T. Rung, F. Thiele, et al. Comparison of les and rans in bluff-body flows. *Journal of Wind Engineering and Industrial Aerodynamics*, 89(14):1471–1485, 2001.

[99] X. Ma, G.-S. Karamanos, and G. Karniadakis. Dynamics and low-dimensionality of a turbulent near wake. *Journal of Fluid Mechanics*, 410:29–65, 2000.

[100] H. G. Matthies and J. Steindorf. Partitioned strong coupling algorithms for fluid–structure interaction. *Computers & Structures*, 81(8):805–812, 2003.

[101] S. F. McCormick. *Multigrid methods*, volume 3. Siam, 1987.

[102] C. Meneveau, T. S. Lund, and W. H. Cabot. A lagrangian dynamic subgrid-scale model of turbulence. *Journal of Fluid Mechanics*, 319:353–385, 1996.

[103] F. Menter. Influence of freestream values on k-omega turbulence model predictions. *AIAA journal*, 30(6):1657–1659, 1992.

[104] F. Menter and Y. Egorov. A scale-adaptive simulation model using two-equation models. *AIAA paper*, 1095:2005, 2005.

[105] F. R. Menter. Zonal two equation k-turbulence models for aerodynamic flows. *AIAA paper*, 2906:1993, 1993.

[106] F. R. Menter. Two-equation eddy-viscosity turbulence models for engineering applications. *AIAA journal*, 32(8):1598–1605, 1994.

[107] C. Michler, S. Hulshoff, E. Van Brummelen, and R. De Borst. A monolithic approach to fluid–structure interaction. *Computers & fluids*, 33(5):839–848, 2004.

[108] C. Michler, E. Van Brummelen, and R. De Borst. An interface newton–krylov solver for fluid–structure interaction. *International Journal for Numerical Methods in Fluids*, 47 (10-11):1189–1195, 2005.

[109] R. Mittal and G. Iaccarino. Immersed boundary methods. *Annu. Rev. Fluid Mech.*, 37: 239–261, 2005.

[110] C. Mockett. *A Comprehensive Study of Detached Eddy Simulation*. Univerlagtuberlin, 2009.

[111] D. Mok and W. Wall. Partitioned analysis schemes for the transient interaction of incompressible flows and nonlinear flexible structures. *Trends in computational structural mechanics, Barcelona*, 2001.

[112] R. D. Moser, J. Kim, and N. N. Mansour. Direct numerical simulation of turbulent channel flow up to re= 590. *Phys. Fluids*, 11(4):943–945, 1999.

[113] M. Münsch and M. Breuer. Numerical simulation of fluid–structure interaction using eddy–resolving schemes. In *Fluid Structure Interaction II*, pages 221–253. Springer, 2011.

[114] K. Ng, M. Yusoff, and E. Ng. Higher-order bounded differencing schemes for compressible and incompressible flows. *International Journal for Numerical Methods in Fluids*, 53 (1):57–80, 2007.

[115] F. Nicoud and F. Ducros. Subgrid-scale stress modelling based on the square of the velocity gradient tensor. *Flow, turbulence and Combustion*, 62(3):183–200, 1999.

[116] L. Ong and J. Wallace. The velocity field of the turbulent very near wake of a circular cylinder. *Experiments in fluids*, 20(6):441–453, 1996.

[117] C. S. Peskin. Numerical analysis of blood flow in the heart. *Journal of computational physics*, 25(3):220–252, 1977.

[118] C. S. Peskin. The immersed boundary method. *Acta numerica*, 11:479–517, 2002.

[119] J. Piquet. *Turbulent flows: models and physics*. Springer Science & Business Media, 2013.

[120] P. Pironkov. *Numerical simulation of thermal fluid-structure interaction*. PhD thesis, TU Darmstadt, 2010.

[121] S. B. Pope. *Turbulent flows*. Cambridge university press, 2000.

[122] M. Popovac and K. Hanjalic. Compound wall treatment for rans computation of complex turbulent flows and heat transfer. *Flow, turbulence and combustion*, 78(2):177–202, 2007.

[123] V. Przulj and B. Basara. Bounded convection schemes for unstructured grids. *AIAA paper*, 2593:2001, 2001.

[124] T. Reimann. *Numerische Simulation von Fluid-Struktur-Interaktion in turbulenten Strömungen*. Logos Verlag, 2013.

[125] T. Reimann, A. Ali, D. C. Sternel, and M. Schaefer. Numerical simulation of a turbulent fsi benchmark case. *PAMM*, 14(1):631–632, December 2014. ISSN 1617-7061. URL http://tubiblio.ulb.tu-darmstadt.de/73951/.

[126] O. Reynolds. An experimental investigation of the circumstances which determine whether the motion of water shall be direct or sinuous, and of the law of resistance in parallel channels. *Proceedings of the royal society of London*, 35(224-226):84–99, 1883.

[127] O. Reynolds. On the dynamical theory of incompressible viscous fluids and the determination of the criterion. *Proceedings of the Royal Society of London*, 56(336-339):40–45, 1894.

[128] O. Reynolds. On the dynamical theory of incompressible viscous fluids and the determination of the criterion. *Philosophical Transactions of the Royal Society of London. A*, 186: 123–164, 1895.

[129] L. F. Richardson. *Weather prediction by numerical process*. Cambridge University Press, 2007.

[130] D. Rival, R. Manejev, and C. Tropea. Measurement of parallel blade–vortex interaction at low reynolds numbers. *Experiments in Fluids*, 49(1):89–99, 2010.

[131] D. Rival, G. Hass, and C. Tropea. Recovery of energy from leading- and trailing-edge vortices in tandem-airfoil configurations. *Journal of Aircraft*, 48:203–211, February 2011. URL http://tubiblio.ulb.tu-darmstadt.de/69731/.

[132] D. E. Rival. *Development, Control and Recovery of Leading- and Trailing-Edge Vortices in Tandem-Airfoil Configurations*. PhD thesis, Technische Universität, Darmstadt, October 2009. URL http://tuprints.ulb.tu-darmstadt.de/1929/.

[133] P. J. Roache. Code verification by the method of manufactured solutions. *Journal of Fluids Engineering*, 124(1):4–10, 2002.

[134] A. M. Roma, C. S. Peskin, and M. J. Berger. An adaptive version of the immersed boundary method. *Journal of computational physics*, 153(2):509–534, 1999.

[135] S. Rugonyi and K. Bathe. On finite element analysis of fluid flows fully coupled with structural interactions. *CMES- Computer Modeling in Engineering and Sciences*, 2(2): 195–212, 2001.

[136] P. Sagaut. *Large eddy simulation for incompressible flows: an introduction*. Springer Science & Business Media, 2006.

[137] K. Salari and P. Knupp. Code verification by the method of manufactured solutions. Technical report, Sandia National Labs., Albuquerque, NM (US); Sandia National Labs., Livermore, CA (US), 2000.

[138] M. Schäfer. *Numerik im Maschinenbau*. Springer DE, 1999.

[139] H. Schlichting and K. Gersten. Boundary layer theory springer-verlag. *Berlin, Heidelberg*, 2000.

[140] W. Schmidt. Der wellpropeller ein neuer antrieb fur wasser-land-und luftfahrzeuge. *Zeitschrift fur Flugwissenschaften*, 13(12):472, 1965.

[141] B. Šekutkovski, I. Kostić, A. Simonović, P. Cardiff, and V. Jazarević. Three-dimensional fluid–structure interaction simulation with a hybrid rans–les turbulence model for applications in transonic flow domain. *Aerospace Science and Technology*, 49:1–16, 2016.

[142] V. Shinde, T. Marcel, Y. Hoarau, T. Deloze, G. Harran, F. Baj, J. Cardolaccia, J.-P. Magnaud, E. Longatte, and M. Braza. Numerical simulation of the fluid–structure interaction in a tube array under cross flow at moderate and high reynolds number. *Journal of Fluids and Structures*, 47:99–113, 2014.

[143] M. L. Shur, P. R. Spalart, M. K. Strelets, and A. K. Travin. A hybrid rans-les approach with delayed-des and wall-modelled les capabilities. *International Journal of Heat and Fluid Flow*, 29(6):1638–1649, 2008.

[144] J. Smagorinsky. General circulation experiments with the primitive equations: I. the basic experiment*. *Monthly weather review*, 91(3):99–164, 1963.

[145] F. Sotiropoulos and X. Yang. Immersed boundary methods for simulating fluid–structure interaction. *Progress in Aerospace Sciences*, 65:1–21, 2014.

[146] M. Souli and D. J. Benson. *Arbitrary Lagrangian Eulerian and fluid-structure interaction: numerical simulation*. John Wiley & Sons, 2013.

[147] P. R. Spalart. Strategies for turbulence modelling and simulations. *International Journal of Heat and Fluid Flow*, 21(3):252–263, 2000.

[148] P. R. Spalart and S. R. Allmaras. A one equation turbulence model for aerodinamic flows. *AIAA journal*, 94, 1992.

[149] P. R. Spalart, W. Jou, M. Strelets, and S. Allmaras. Comments of feasibility of les for wings, and on a hybrid rans/les approach. *Greyden Press*, 20(3):181–195, 1997.

[150] P. R. Spalart, S. Deck, M. Shur, K. Squires, M. K. Strelets, and A. Travin. A new version of detached-eddy simulation, resistant to ambiguous grid densities. *Advances in DNS/LES*, 20(3):181–195, 2006.

[151] C. Speziale. Turbulence modeling for time-dependent rans and vles: a review. *AIAA journal*, 36(2):173–184, 1998.

[152] C. G. Speziale. Computing non-equilibrium turbulent flows with time-dependent rans and vles. In *Fifteenth International Conference on Numerical Methods in Fluid Dynamics*, pages 123–129. Springer, 1997.

[153] C. G. Speziale, S. Sarkar, and T. B. Gatski. Modelling the pressure–strain correlation of turbulence: an invariant dynamical systems approach. *Journal of Fluid Mechanics*, 227: 245–272, 1991.

[154] J. H. Spurk. *Strömungslehre*, volume 8. Springer Berlin, 2010.

[155] H. L. Stone. Iterative solution of implicit approximations of multidimensional partial differential equations. *SIAM Journal on Numerical Analysis*, 5(3):530–558, 1968.

[156] P. K. Sweby. High resolution schemes using flux limiters for hyperbolic conservation laws. *SIAM journal on numerical analysis*, 21(5):995–1011, 1984.

[157] K. Takizawa, T. E. Tezduyar, J. Boben, N. Kostov, C. Boswell, and A. Buscher. Fluid–structure interaction modeling of clusters of spacecraft parachutes with modified geometric porosity. *Computational Mechanics*, 52(6):1351–1364, 2013.

[158] P. Temarel et al. Numerical simulation of an oscillating cylinder in cross-flow at a reynolds number of 10,000: Forced and free oscillations. In *ASME 2014 33rd International Conference on Ocean, Offshore and Arctic Engineering*, pages V002T08A022–V002T08A022. American Society of Mechanical Engineers, 2014.

[159] M. Temmerman, L.; Leschziner. Large eddy simulation of separated flow in a channel with corrugated wall. *Proc. 2nd Int. Conf. on Turbulence and Shear Flow Phenomena*, 3: 399–404, 2001.

[160] T. E. Tezduyar and S. Sathe. Modelling of fluid–structure interactions with the space–time finite elements: solution techniques. *International Journal for Numerical Methods in Fluids*, 54(6-8):855–900, 2007.

[161] P. Thomas and C. Lombard. Geometric conservation law and its application to flow computations on moving grids. *AIAA journal*, 17(10):1030–1037, 1979.

[162] A. K. Travin, M. L. Shur, P. R. Spalart, and M. K. Strelets. Improvement of delayed detached-eddy simulation for les with wall modelling. In *ECCOMAS CFD 2006: Proceedings of the European Conference on Computational Fluid Dynamics, Egmond aan Zee, The Netherlands, September 5-8, 2006*. Delft University of Technology; European Community on Computational Methods in Applied Sciences (ECCOMAS), 2006.

[163] S. Türk. *Investigation of hybrid turbulence modeling techniques in the context of Fluid-Structure Interaction*. Verlag Dr. Hut, 2014.

[164] E. R. Van Driest. On turbulent flow near a wall. *Journal of the Aeronautical Sciences*, 2012.

[165] R. Van Loon, P. Anderson, F. Van de Vosse, and S. Sherwin. Comparison of various fluid–structure interaction methods for deformable bodies. *Computers & structures*, 85(11): 833–843, 2007.

[166] J. Vierendeels. Implicit coupling of partitioned fluid-structure interaction solvers using reduced-order models. In *Fluid-Structure Interaction*, pages 1–18. Springer, 2006.

[167] W. A. Wall, D. P. Mok, and E. Ramm. Partitioned analysis approach of the transient coupled response of viscous fluids and flexible structures. In *Solids, structures and coupled problems in engineering, proceedings of the European conference on computational mechanics ECCM*, volume 99, 1999.

[168] Z. Warsi. Conservation form of the navier-stokes equations in general nonsteady coordinates. *AIAA Journal*, 19(2):240–242, 1981.

[169] D. C. Wilcox. Reassessment of the scale-determining equation for advanced turbulence models. *AIAA journal*, 26(11):1299–1310, 1988.

[170] D. C. Wilcox. Formulation of the k-omega turbulence model revisited. *AIAA journal*, 46 (11):2823–2838, 2008.

[171] D. C. Wilcox et al. *Turbulence modeling for CFD*, volume 2. DCW industries La Canada, CA, 1998.

[172] J. Wissmann and K.-D. Sarnes. *Finite Elemente in der Strukturmechanik*. Springer, 2006.

[173] S. L. Woodruff. Coupling turbulence in hybrid les-rans techniques. In *TSFP DIGITAL LIBRARY ONLINE*. Begel House Inc., 2011.

[174] L. Xue. *Entwicklung eines effizienten parallelen Lösungsalgorithmus zur dreidimensionalen Simulation komplexer turbulenter Strömungen*. na, 1998.

[175] A. Yoshizawa and K. Horiuti. A statistically-derived subgrid-scale kinetic energy model for the large-eddy simulation of turbulent flows. *Journal of the Physical Society of Japan*, 54(8):2834–2839, 1985.

[176] H. Zhang, C. Bachman, and H. F. Fasel. Application of a new methodology for simulations of complex turbulent flows. *AIAA paper*, 2535:2000, 2000.